Spring 5-2022

Experimental Investigation of All-Optical Production of Metastable Krypton

Joshua Carl Frechem
Old Dominion University, jfrech14@hotmail.com

EXPERIMENTAL INVESTIGATION OF ALL-OPTICAL PRODUCTION OF METASTABLE KRYPTON

by

Joshua Carl Frechem
B.S. August 2016, Old Dominion University
B.S.M.E. August 2016, Old Dominion University
M.S. May 2019, Old Dominion University

A Dissertation Submitted to the Faculty of
Old Dominion University in Partial Fulfillment of the
Requirements for the Degree of

DOCTOR OF PHILOSOPHY

PHYSICS

OLD DOMINION UNIVERSITY
May 2022

Approved by:

Charles Sukenik (Director)

Robert Ash (Member)

Peter Bernath (Member)

Desmond Cook (Member)

Alexander Gurevich (Member)

ABSTRACT

EXPERIMENTAL INVESTIGATION OF ALL-OPTICAL
PRODUCTION OF METASTABLE KRYPTON

Joshua Carl Frechem
Old Dominion University, 2022
Director: Dr. Charles Sukenik

Metastable production of noble gases requires significant energy due to their filled valence shells. These transitions from the ground state are in the vacuum ultraviolet and extreme ultraviolet, which are relatively inaccessible to lasers. This necessitates the use of either electron/ion bombardment via inefficient glow discharges or the use of high-power lasers and nonlinear processes. The all-optical production efficiency using these high-power lasers promises to be orders of magnitude higher than glow discharges, but far more costly. This work looks to improve all-optical production of metastable krypton (Kr*) through the use of a commercially available vacuum ultraviolet lamp with a low-power diode laser coupled to a power build-up cavity to excite two resonant transitions, and to leverage this excitation scheme in the study of producing a diode-pumped rare gas laser. The data obtained in this work show similar production rates to comparable, state-of-the-art work done by Z.T. Lu of Hefei National Laboratory, around 10^{10}-10^{11} atoms/s for ^{84}Kr, while using a lower-powered laser and a lower-flux lamp. These data show all-optical production to be comparable to the production rates of discharge-based production of Kr* but offer more scalability than glow discharges and eliminate the contamination caused by plasma-embedded Kr sputtering from chamber walls.

This dissertation is dedicated to my parents, sister, brother-in-law, grandparents, and my best friend for supporting me along the way throughout this journey. Also, to the faculty members and colleagues that have helped me both academically and in making my time at Old Dominion memorable. My doctoral advisor, Charles Sukenik, has been a great mentor, advisor, colleague, and example of professionalism that helped develop my skills in communication and collaboration. This dissertation is also dedicated to my grandfather, who was not able to celebrate the end of this journey with me. He had a tremendous role in who I have grown to be and was always encouraging of my academic pursuits.

ACKNOWLEDGMENTS

I would like to acknowledge the significant role that my advisor, Charles Sukenik, has played in my academic journey at Old Dominion University. He has always had the ability to fix something in the lab with just a look. He has also always allowed me to think for myself and to give me the freedom of trial and error to develop my skills as an experimentalist. The right balance of hands-on vs hands off as an advisor is a hard one to strike, and he has managed to get it down to a science.

Tom Hartlove has been a great help since undergrad, from lunch breaks to machine shop tutorials. Also, the members of the departmental office, Lisa Okun, Delicia Malin, and Annette Guzman-Smith, have always had their work cut out supporting the students while keeping the department running.

I would also like to thank my committee members Robert Ash, Peter Bernath, Desmond Cook, and Alexander Gurevich for the role they played in my experience as a scientist and researcher, as well as their contributions to this dissertation.

Finally, I would like to thank Will Williams and Z.T. Lu for the insightful conversations through the years in collaboration with our lab on the topic of all-optical production and Atom Trap Trace Analysis, as well as the use of equipment loaned from Argonne National Lab. Additionally, I would like to note the work on all-optical production in our lab previously done by Grady White and Lindsay Thornton.

TABLE OF CONTENTS

LIST OF TABLES

LIST OF FIGURES

Figure Page

Figure Page

CHAPTER 1

INTRODUCTION AND MOTIVATION

The invention of the laser has accelerated many fields of research due to its ability to provide narrow-bandwidth, highly directional light that can be scaled to high intensities. The diode laser further improved on these advancements due to its high electrical and optical efficiency, as well as their ability to be designed for a wide range of wavelengths.

While diodes can easily reach the visible and infrared, producing ultraviolet wavelengths below near ultraviolet proves to be a continuing challenge. The high energy produces strong spontaneous emissions that require a high threshold current for pumping and there are few materials that are efficiently transparent below the near ultraviolet. While there are mirrors for the deep and vacuum ultraviolet, the short wavelength results in surface quality being of a lower quality with metrology figures of merit typically being measured with He-Ne lasers at 633 nm.

This limitation of diode lasers has led to the prolonged use of high-powered gas and ion lasers for ultraviolet applications. However, tunability of these lasers is limited. Nonlinear optics, such as frequency tripling, can lead to moderately tunable ultraviolet lasers at the cost of efficiency. All of these reasons lead to the heavy use of plasma discharges for excitation when a transition is in the ultraviolet. Plasma, specifically glow, discharges convert electricity to light through the ionization of a gas. This process is very inefficient, but glow discharges are easy and inexpensive to build.

Plasmas, while easy to generate, are highly inefficient ($<10^{-4}$) and cause major contamination. This contamination happens through production of ions, which are more reactive than neutral atoms, and by being driven into the vacuum chamber walls. This research looks to improve on the use of glow discharges for the production of metastable krypton (Kr*) through the design and application of an all-optical excitation scheme. All-optical excitation schemes benefit from the higher optical-optical efficiency of laser-driven transitions and eliminate the contamination of plasma driven into the walls of its container. Additionally, the use of a metastable state allows long counting times due to the long lifetime of the state, which cannot radiatively decay via dipole interactions. This work also seeks to realize even more efficient all-optical excitation of Kr* through the use of a low-powered diode laser coupled to an optical resonator and an optically coupled, commercially available RF lamp.

This increase in efficiency will be directly applicable to the next generation of noble gas radioisotopic dating techniques, such as Atom Trap Trace Analysis (ATTA), and high-powered lasers through the advancement of diode-pumped rare gas lasers (DPRGL).

1.1 GLOW DISCHARGES

Glow discharges can be operated by application of a direct current (DC) or alternating current (AC) voltage to a volume of gas. A DC plasma discharge occurs when the constant voltage between the anode and cathode accelerates electrons from the cathode to the anode. Once the voltage is high enough, the electrons have enough energy to ionize gas while it traverses the discharge. Fluorescence occurs once the collisional energy is high enough to excite atoms and ions to excited electronic states, after which they fluoresce as the atoms and ions radiatively relax to ground.

AC discharges typically operate through the application of a radio frequency (RF) voltage that causes an oscillating field inside the discharge. As the RF power increases, the energy becomes high enough to excite or further ionize the gas when out of phase atoms or ions collide. The glow occurs through the same fluorescence mechanism as in a DC discharge. RF discharges are typically either capacitively coupled or inductively coupled. The capacitively coupled discharge is similar to the DC discharge, but the AC voltage causes more collisions between the electrodes. This is due to averaging the motion over the whole period, which increases the efficiency. In the discharges that involve electrodes, either an external spark can start the plasma, or the voltage needs to be above the breakdown voltage to strip an electron from the atom. The electron is then accelerated and collides to produce more atoms until an avalanche effect occurs and starts the plasma.

Inductively coupled discharges use a coil around the gas to produce a magnetic field inside the gas (which produces an electric field in the gas). The electromagnetic fields in the discharge region produce a figure-8 motion, leading to collisions. Since there are no electrodes in the inductively coupled discharge, a spark of some type needs to be provided to start the discharge except when very high voltages are applied [1]. An image of the glow discharge used in this dissertation is shown in Fig. 1.

1.2 ATOM TRAP TRACE ANALYSIS

Metastable rare gases have found use in many areas of research which benefit from the long lifetime of the metastable states, the lack of hyperfine structure of even isotopes, and

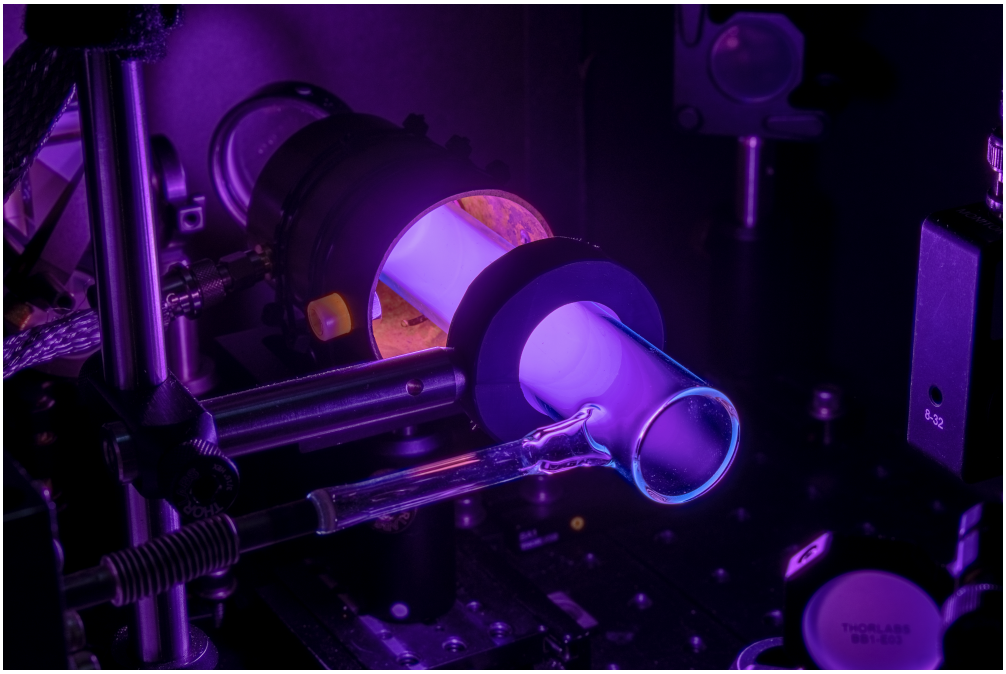

FIG. 1. The Kr glow discharge used to lock the laser to the selected ^{84}Kr transition glows purple at lower pressures due to less attenuation/quenching of the higher frequency transitions.

the chemical inertness of neutral rare gases. Metastable rare gases also have a high probability of undergoing Penning ionization, which allows them to be efficiently detected with electron multipliers[2]. In 1999, the research group of Z.T. Lu at Argonne National Lab first demonstrated the use of metastable rare gases to realize an ultrasensitive isotope trace analysis technique (ATTA) based on Kr* [3]. This technique extends the capabilities of low-level counting and accelerator mass spectrometry for detection and quantification of radionuclides. For specific details on low-level counting and the specific origins of radionuclides, see [4]. An overview of accelerator mass spectrometry and its applications can be found in [5].

ATTA improves upon the other trace analysis techniques through the extremely selective technique of trapping the atoms in a magneto-optical trap (MOT). Samples do not need to be as pure as for other techniques because different isotopes of an atom have shifted resonances due to changes in the electronic levels of the isotopes. A MOT targets the transition of a specific isotope through careful selection of laser frequency and polarization. If a laser's linewidth is narrow enough, the probability of a contaminant atom or molecule having a transition that is also resonant with the laser approaches zero due to the discrete

quantization of energy levels [6]. However, too many contaminants can knock target atoms out of the MOT. Therefore, more isotopically selective trapping techniques are used than just a 3D MOT for counting. Typically, a 2D MOT and a Zeeman slower further isolate and prepare the atoms for trapping in the counting MOT [7]. The targeting of a specific isotope requires the use of Doppler free spectroscopic techniques to lock the laser to the particular isotope transition. This is because the isotope shifts are typically much smaller than the Doppler width, and the Doppler width is centered around the center of mass of the isotopes.

Krypton is of particular interest for radionuclide dating because ^{85}Kr has an extraordinarily low natural abundance with a half-life of 10.8 years, and is formed naturally from cosmic rays interacting with ^{84}Kr. Nearly all of the current ^{85}Kr in the atmosphere is from anthropogenic nuclear activity. This enables detection and geographic tracing of nuclear activity through detection in atmospheric sources. It also enables the dating of shallow groundwater due to the short half-life [3].

^{81}Kr has a half-life of 230,000 years, which enables samples to be dated that are older than what ^{14}C allows. Additionally, the selectivity of ATTA also allows dating of old samples that are contaminated with modern, anthropogenic sources. One such application is dating of ancient groundwater. Carbon contamination from human activity would give inaccurate readings when using ^{14}C, but ATTA with ^{81}Kr would give accurate readings due to the lack of anthropogenic sources [8, 9].

An exciting prospective application of ATTA was in the development of dark matter detectors. ATTA was used to detect ^{85}Kr contamination, which produces a radiation background, in atmospheric Xe that is collected for the liquid Xe (LXe) dark matter detectors. Although dark matter was not detected, it demonstrated a new level of noble gas purification [10].

Thus far, all ATTA devices have implemented RF discharges to populate the metastable state for Ar, Kr, and Xe. While optical production of metastable has been performed, none of the efforts had been implemented into an ATTA device until Z.T. Lu *et al.* in 2021 [11]. In that work, a ^{83}Kr* production rate of $7.2{\cdot}10^{10}$ atoms/s and a ^{84}Kr* production rate of $4.5{\cdot}10^{11}$ atoms/s were measured. The work performed in this dissertation specifically looked at ^{84}Kr, as it is the most abundant [12]. While ^{84}Kr is the most abundant isotope with a natural abundance of 57%, there are only trace amounts of the radioisotopes of interest, ^{81}Kr and ^{85}Kr.

The work in this dissertation looks to further improve on the efficiency of ATTA through the continued investigation of all-optical production of metastables with the added benefit

of using the small form-factor and decreased cost of a low-powered diode laser coupled to an optical cavity. Eliminating the need for high-powered lasers such as a Ti:Sapphire laser or a diode with a tapered amplifier opens up the opportunities to build extremely compact systems.

1.3 DIODE-PUMPED RARE GAS LASER

Many studies have been done on the effectiveness of rare gas buffers for a rare gas laser. The main species studied for a rare gas laser has been Ar, which offers much insight into the creation of a Kr DPRGL [13–16]. DPRGL have been demonstrated for Ne, Ar, Kr, and Xe as pulsed lasers. However, continuous wave DPRGL have only been demonstrated in Ar [15, 17]. These lasers typically operate by producing metastables in a discharge and using a diode laser to pump the cycling transition of the DPRGL. It is challenging to produce a significant density of metastables in a discharge at such high pressures. While there has been headway on designs to alleviate this symptom, such as a pulsed discharge in [15] and a microplasma discharge in [17], the promise of all-optical production to eliminate the need for a discharge offers an expanded range of pressures and the ability to scale powers more efficiently to saturate metastable production. There are several methods of all-optical production, such as two-photon transitions out of the ground state or two-step transitions using vacuum ultraviolet (VUV) + near infrared (NIR). This dissertation will focus specifically on the two-step method where the VUV transition is incoherently excited with a VUV lamp and the NIR transition is coherently driven with a cavity-coupled diode laser. At the time of writing, the author of this dissertation has not seen experimental work done on the application of all-optical production of metastable rare gases, as done in ATTA experiments, to the field of DPRGL. Significant theoretical work has been done using the discharge production method in [18–23].

1.4 DISSERTATION OVERVIEW

The purpose of the research performed in this dissertation was to investigate the feasibility of using a low-powered diode laser coupled to a power build-up cavity instead of high-powered lasers in the all-optical production of Kr*, using the excitation scheme shown in Fig. 2. In studying the production of Kr*, the experimental apparatus was already set to also look at how the Kr* production responds to the addition of a buffer gas, specifically He. The knowledge of how Kr* production responds to a He buffer gas will provide valuable information for the more efficient creation of a DPRGL through all-optical means, rather

than the typical discharge method. This increase in efficiency would lead the way for a decrease in size, weight, and power (SWaP) for the DPRGL, enabling its use in a wider range of applications.

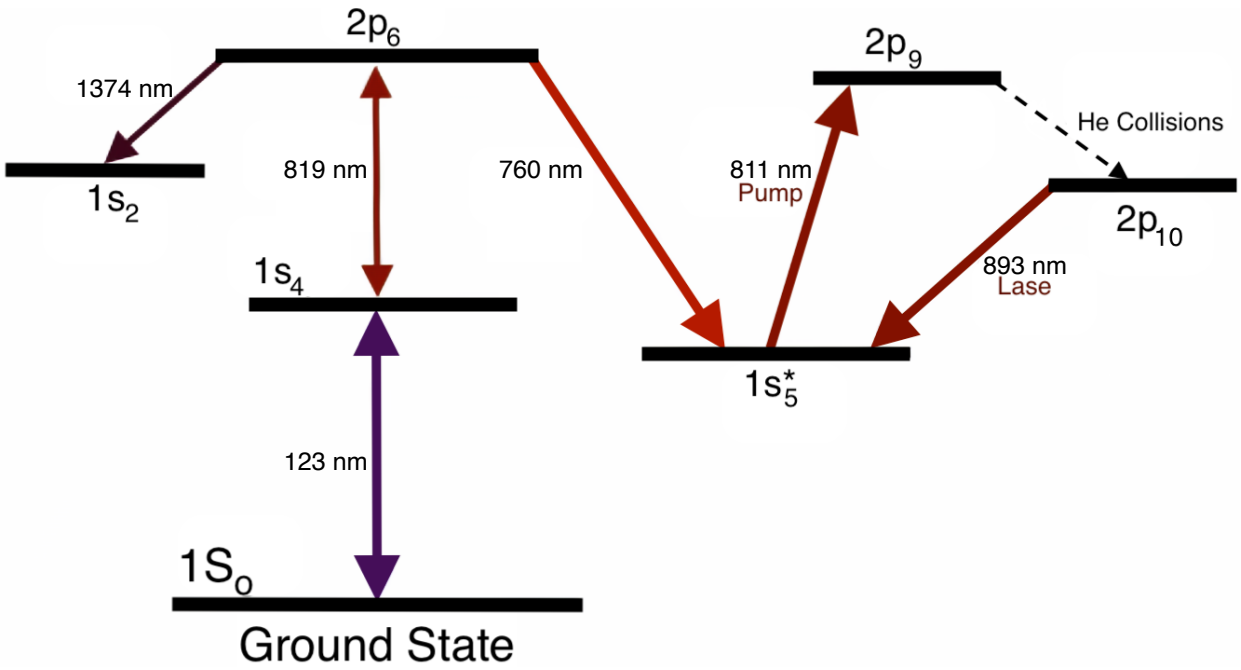

FIG. 2. This figure shows the two-step all-optical excitation scheme to produce Kr*, as well as the pumping scheme for the DPRGL. Double arrows represent transitions that have dipole-allowed radiative decays and are optically pumped.

In this dissertation, the first four chapters cover the basics of atomic spectroscopy, lasers, optical resonators, and feedback mechanisms that are critical foundations for this research. Then, the experimental setup will be described and both how and why certain components and designs were chosen or built will be discussed. A large portion of that discussion is on the construction of the build-up cavity, which went through several design iterations where the mirror mounts were designed, from custom and off-the-shelf parts, and constructed in the lab.

Finally, the dissertation goes into the important experimental and theoretical results of this dissertation in Chapter 7. Section 7.1 goes through the results of measuring the build-up of the cavity to more accurately determine the intensity of the 819 nm laser in

the Kr* production region. With a more accurate knowledge of this intensity, more precise information can be determined about the two-step transition under study for the all-optical production.

Section 7.2 discusses the results of how 819 nm intensity and 123 nm intensity affect Kr* production, also as a function of pressure from 1 mTorr to 10 Torr. This information would allow optimization of hardware selection and experimental parameters in ATTA and DPRGLs to maximize Kr* production at as high of a wall-plug efficiency as possible.

The final section of experimental data, in section 7.4, discusses how the addition of a He buffer affects Kr* production as a function of He and Kr partial pressures. This information helps guide understanding of effective quenching rates when experimental quenching rates are not available for particular states for the use in modeling. This also enables the comparison between the addition of a He buffer in an all-optical setup to well-established data using a discharge.

The computational model with an experimental comparison is discussed at the end of this dissertation. The conclusion then goes into what future work will be performed and what steps could be taken to further expand on the data presented in this dissertation. The use of metastable rare gases has shown, and continue to show, important applications in various fields of physics. The all-optical production of these metastables will allow more efficient use of these metastables, and the use of a low-powered diode laser will open the door to lower cost and smaller size for integration of the all-optical method into experiments.

CHAPTER 2

THEORY OF ATOMIC SPECTROSCOPY

Atomic spectroscopy is governed by rigid rules defined by quantum mechanics. The transitions discussed in this dissertation are almost entirely what are called dipole allowed transitions, or electronic transitions. The other transitions are higher order terms of the multipole expansion, which is discussed at length in the well-known text by Jackson [24]. There are selection rules that define which transitions can occur due to dipole interactions. The derivation of these selection rules to include increasingly complex interactions such as the fine and hyperfine structures of multi-electron atoms can take up a significant portion of a book, and is done so very well in Peter Bernath's book *Atoms and Molecules* [25]. While the wavefunctions of any two levels of a multi-electron atom can be quite complicated due to these perturbations, the determining factor of whether a transition is dipole allowed or not depends on whether the transition moment integral, Eq. (1), is zero or nonzero. $\vec{M}$ is the transition dipole moment, which gives the probability of the transition from state i to f. The wavefunction of a particular level is denoted as ψ, and $\vec{\mu}$ is the dipole operator, which is a charge-weighted sum of all of the electron position vectors of a multi-electron atom or molecule. If the integral is 0, then the transition is not dipole allowed, otherwise known as forbidden. However, the text by Bernath goes into extreme detail on how symmetry and group theory can be used to determine the symmetry of atomic and molecular transition moments in order to determine if a transition is forbidden without solving the integral.

$$\vec{M} = \int \psi_f^* \vec{\mu} \psi_i d\tau \tag{1}$$

2.1 PERTURBATIONS AND COUPLING SCHEMES

In this section, the notation used will be such that single electron atoms or specific electrons use lowercase quantum numbers and multi-electron atoms use uppercase quantum numbers. This dissertation focuses on multi-electron atoms.

The Laporte rule states that transitions between like orbitals are forbidden, meaning $\Delta \mathrm{l} = \pm 1$, where l is the orbital angular momentum quantum number of the atom making the

transition. Really, the Laporte rule is saying parity conservation is forbidden for electronic transitions, more rigorously stated in Eq. (1). Another selection rule for a single-electron atom is $\Delta m = 0, \pm 1$, where m is the magnetic quantum number. The rules are modified and more complex when higher-order corrections are included for multi-electron atoms, like electron-electron repulsion and spin-orbit coupling, which will be notated using the Russell-Saunders (LS)-coupling scheme.

For these multi-electron vector models, the angular momenta are vector sums of the individual electron angular momenta vectors, $\vec{L} = \sum_{i=1}^{n} \vec{l_i}$. The corresponding multi-electron quantum number is L, where $|\vec{L}| = \sqrt{L(L+1)}\hbar$ and the direction of the vector is determined by M_L.

Electron-electron repulsions are included in the Hamiltonian of multi-electron atoms, and represent the first, and largest, splitting of energy levels, called terms. If this correction is the only significant correction included, the eigenstates are $|nLM_LSM_S\rangle$ with degeneracy of (2L+1)(2S+1). For these eigenstates, n is the principal quantum number, L is the multi-electron total orbital angular momentum quantum number, and M_L multi-electron magnetic quantum number, which is the projection of $\vec{L}$ onto the z-axis. S is the multi-electron spin quantum number and M_S is the projection of the spin vector onto the z-axis. At this level of perturbation, the next level of designation after term is state, which can be determined by using Slater determinants to denote the degenerate states for each term. In the LS-coupling notation, these terms are represented as ^{2S+1}L, where S values are scalar combinations of the sum of all of the electron spins in open shells, and L values are the scalar combinations of the sum of all of the electron orbital angular momentum quantum numbers in the open shells. For a two-electron atom, this is represented by $L=(l_1 + l_2)...|l_1 - l_2|$ and $S=(s_1 + s_2)...|s_1 - s_2|$. For example, for two electrons with $|l_1 s_1\rangle = |1, 1/2\rangle$ and $|l_1 s_2\rangle = |1, 1/2\rangle$, the possible L values are 0,1, and 2 while the S values are 0 or 1 [26]. The selection rules for these terms are $\Delta L = 0, \pm 1$, except $L=0 \rightarrow L'=0$, and $\Delta S = 0$.

Spin-orbit coupling is the interaction between the electronic spin and its orbital angular momentum, which is one of the corrections in what is called the fine structure. The other two corrections in the fine structure are relativistic corrections using perturbation theory. Spin-orbit coupling is the correction that lifts the degeneracy of the states determined by the Slater determinants for the case of electron-electron repulsion. The eigenstates for this coupling are $|LSJM_J\rangle$, where $\vec{J}=\vec{L}+\vec{S}$ is the total angular momentum and the corresponding quantum number takes the scalar values J=(L+S)...|L-S|. M_J is the total angular momentum magnetic quantum number, which is the projection of $\vec{J}$ onto the z-axis. The LS-coupling

notation for this interaction is the $^{2S+1}L_J$ level. The selection rules for the spin-orbit coupling are $\Delta J = 0, \pm 1$ except for J=0→J′=0, and $\Delta M_J = 0, \pm 1$ except for $M_J = 0 \rightarrow 0$ if $\Delta J = 0$.

The final major correction after the fine structure is known as the hyperfine structure (IJ Coupling). The hyperfine structure, $\vec{F}$=$\vec{J}$+$\vec{I}$, is due to the interaction between nuclear spin ($\vec{I}$) and the electron's angular momentum ($\vec{J}$), with M_F being the projection onto the z-axis. The eigenstates for this coupling are $|IJFM_F\rangle$ and the possible F values are F=(I+J)...|I-J|. This IJ coupling has the selection rules $\Delta F = 0, \pm 1$ except for F=0→F′=0 and and $\Delta M_F = 0, \pm 1$ except for $M_F = 0 \rightarrow 0$ if $\Delta F = 0$ [25].

When external magnetic fields are applied (Zeeman Effect) or external electric fields are applied (Stark Effect) the degeneracies can be lifted. For the Zeeman Effect, if fine and hyperfine structures are excluded, the 2S+1 number of levels split into 2L+1 states, denoted M_L. If the fine structure is included, the 2S+1 number of levels are split into 2J+1 magnetic sublevels, denoted M_J. Finally, if the hyperfine structure is included, each F level is split into 2F+1 magnetic sublevels, denoted M_F. The Stark Effect is separated into DC and AC Stark Effect. While the DC Stark Effect lifts degeneracies like the Zeeman Effect, the AC Start Effect primarily shifts the energy levels.

A crucial note is that the LS-coupling only remains valid when the spin-orbit interaction is much weaker than the electron-electron repulsion (lighter elements). When the electron-electron repulsion is much weaker than the spin-orbit interaction (heavier elements), a coupling scheme called jj-coupling is used. In this coupling scheme, the angular momenta of each electron are coupled and, the frame of reference is shifted to j with l and s precessing around it. Intermediate coupling is needed between these two regimes [27].

2.1.1 PASCHEN AND RACAH NOTATIONS

Paschen and Racah notations are notations used for excited noble gases that deal with a core ion and an excited electron. Both notations are found in literature, but Racah notation has come into favor by coupling quantum numbers of the ion to the excited electron, whereas Paschen notation was formulated to fit experimental data compared to the hydrogen spectrum.

Paschen notation is written as nl#, where n is the energy level (principal quantum number) and l is the orbital angular momentum quantum number of the excited electron. The # is the energy level of the term nl, where 1 is the highest energy level and the number increases as the energy level decreases. Paschen notation of the energy levels of krypton that are under investigation in this research can be seen later in this dissertation in Fig. 43.

Racah notation is a combination of LS-coupling and J_1L_2-coupling, where K couples the total spin of the ion with the orbital angular momentum of the excited electron ($\vec{K}=\vec{J_1}+\vec{l}$), and J is the total angular momentum by combining K and the spin angular momentum of the excited electron ($\vec{J}=\vec{K}+\vec{s}$). The level for Racah notation is $^{2S_1+1}L_{1_{J_1}}\,nl[K]^o_J$ where S_1, L_1, and J_1 are the spin angular momentum, orbital angular momentum, and total angular momentum quantum numbers of the parent ion. J remains the total angular momentum quantum number of the atom, while n and l are the principal quantum number and orbital angular momentum quantum number of the atom. The superscript o designates the parity of the state. For the noble gases, the parent ions can only be $^2P_{1/2}$ and $^2P_{3/2}$. This is often shortened as nl $^2P_{3/2}$ for and nl' for $^2P_{1/2}$ [27, 28].

TABLE 1. Table of energy levels in Paschen and Racah notations.

Paschen	Electronic Configuration	Racah
$1p_0$	$[Ar]4p^6$	$^1S_0$
$1s_5$	$[Ar]4p^5 5s^1$	$^2P_{3/2}\ 5s[3/2]^o_2$
$1s_4$	$[Ar]4p^5 5s^1$	$^2P_{3/2}\ 5s[3/2]^o_1$
$1s_3$	$[Ar]4p^5 5s^1$	$^2P_{1/2}\ 5s[1/2]^o_0$
$1s_2$	$[Ar]4p^5 5s^1$	$^2P_{1/2}\ 5s[1/2]^o_1$
$2p_{10}$	$[Ar]4p^5 5p^1$	$^2P_{3/2}\ 5p[1/2]^o_1$
$2p_9$	$[Ar]4p^5 5p^1$	$^2P_{3/2}\ 5p[5/2]^o_3$
$2p_8$	$[Ar]4p^5 5p^1$	$^2P_{3/2}\ 5p[5/2]^o_2$
$2p_7$	$[Ar]4p^5 5p^1$	$^2P_{3/2}\ 5p[3/2]^o_1$
$2p_6$	$[Ar]4p^5 5p^1$	$^2P_{3/2}\ 5p[3/2]^o_2$
$2p_5$	$[Ar]4p^5 5p^1$	$^2P_{3/2}\ 5p[1/2]^o_0$
$2p_4$	$[Ar]4p^5 5p^1$	$^2P_{1/2}\ 5p[3/2]^o_1$
$2p_3$	$[Ar]4p^5 5p^1$	$^2P_{1/2}\ 5p[3/2]^o_2$
$2p_2$	$[Ar]4p^5 5p^1$	$^2P_{1/2}\ 5p[1/2]^o_1$
$2p_1$	$[Ar]4p^5 5p^1$	$^2P_{1/2}\ 5p[1/2]^o_0$

2.2 ATOMIC ABSORPTION AND EMISSION

The fundamental processes of atomic physics involve the interaction of light with the two-level atom. The history books tell the tale of how Einstein devised a thought experiment that would consider the intuitive, basic processes that could possibly happen in such a system assuming thermal radiation in equilibrium with the atom and conservation of the laws of thermodynamics. The result was that three processes are possible, which are absorption, stimulated emission, and spontaneous emission.

These processes have come to be called the Einstein coefficients, where B_{12} represents absorption, B_{21} represents stimulated emission, and A_{21} represents spontaneous emission. The energy levels may be degenerate with g states or sublevels. It can be seen that absorption and stimulated emission are balanced when a system is simplified to a two-level system, has electric or magnetic fields applied to lift the degeneracy, or the two levels have equal degeneracies.

For a general, degenerate system, the Einstein A_{21} coefficient is defined in Eq. (2), while a non-degenerate, two-level system simplifies to Eq. (3). The degenerate form includes the decay from all of the degenerate excited sublevels together, to each individual sublevel of the lower level. The non-degenerate equation shows the more commonly expressed form for the simplified two-level model with either all degeneracies lifted or simply excluding all other levels and sublevels. The inner products in Eq. (2) can be simplified to the dipole moments of each transition from the upper level, 2, to the lower sublevels, $\mu_{21_{m_l}}$.

$$A_{21} = \frac{8\pi^2 e^2 \nu_{21}^3}{3\epsilon_o \hbar c^3} \sum_{m_l} |\langle 1 m_l | \vec{r} | 2 \rangle|^2 = \frac{8\pi^2 \nu_{21}^3}{3\epsilon_o \hbar c^3} \sum_{m_l} \mu_{21_{m_l}}^2 \tag{2}$$

$$A_{21} = \frac{8\pi^2 e^2 \nu_{21}^3}{3\epsilon_o \hbar c^3} |\langle 1 | \vec{r} | 2 \rangle|^2 = \frac{8\pi^2 \nu_{21}^3 \mu_{21}^2}{3\epsilon_o \hbar c^3} \tag{3}$$

While A_{21} is typically expressed as the inverse of the upper level lifetime, τ_2, this is only true for a two-level system, or a system where level two can radiatively decay to only level 1. If level 2 can radiatively decay to multiple levels, then the excited state lifetime is inversely related to the sum of the Einstein A coefficients of all the lower levels, as expressed in Eq. (4).

$$\sum_g A_{eg} = \frac{1}{\tau_e} \tag{4}$$

$$B_{21} = \frac{c^3}{8\pi\hbar\nu^3} A_{21} \tag{5}$$

Equation (5) shows the expression calculating B_{21} from A_{21}, and as before B_{12} can be found by $B_{12}=\frac{g_2}{g_1}B_{21}$. An important note is that the form of all of these equations depend on how the energy density is formulated. The energy density can be expressed as a function of wavenumber, angular frequency, or frequency. It can also be expressed as a function of spectral radiance, spectral irradiance, or spectral energy density. The form used in this discussion is in terms of spectral energy density, which is a factor of $4\pi/c$ greater than spectral radiance, and Eq. (6) shows the spectral energy density form of Planck's law[29].

$$\rho_\nu(T) = \frac{8\pi\hbar\nu^3}{c^3} \frac{1}{e^{2\pi\hbar\nu/(k_B T)} - 1} \tag{6}$$

2.3 BROADENING MECHANISMS AND SPECTRAL LINESHAPES

Mechanisms for spectral line broadening can be separated into two categories. The first is homogeneous broadening, where all emitters or absorbers equally experience the same broadening. Inhomogeneous broadening is when specific groups of a certain population experience a different amount broadening than other groups. Homogeneous broadening leads to a Lorentzian lineshape, while inhomogeneous broadening leads to a Gaussian lineshape. The true lineshape is a convolution of the two, called a Voigt function.

2.3.1 HOMOGENEOUS BROADENING

Because of the Heisenberg uncertainty principle, spectral linewidths cannot be zero. They must be finite because the energy levels cannot be infinitely narrow, which leads to the Energy-Time uncertainty principle, $\Delta E \Delta t \geq \hbar$. This quantum mechanical limit is what defines the narrowest a spectral line can be, known as the natural linewidth. While features can be observed below the natural linewidth, these special techniques will not be discussed. The natural linewidth is an example of a homogeneous broadening mechanism, because it is a quantum mechanical property that affects the whole population.

The other main type of homogeneous broadening mechanism is collisional broadening. In a well-mixed gas, the mean free path is approximately the same for all atoms in the gas. Therefore, phase disturbances that cause a reduced lifetime occur equally to all atoms in a particular state. The simplified model of collisional broadening causes a broadened linewidth inversely proportional to the mean collision time of the gas, Eq. (7). In (7), P is the pressure, d is the classical atomic diameter, m is the atomic mass, and T is the sample temperature. The mean collision time is the ratio of the mean free path, ℓ to the RMS velocity of the gas.

$$\Delta\nu_P = \frac{1}{\pi T} = \frac{v_{RMS}}{\pi \ell} = \sqrt{\frac{3kT}{m}} \left(\frac{\sqrt{2} P d^2}{kT} \right) \tag{7}$$

There are, however, several specific types of collisional broadening depending on the interactions involved. There are resonant collisions where two atoms of the same species have strong dipoles that interact with each other. There is also Van der Waals broadening from collisions between ground state atoms and excited atoms, and there is Stark broadening due to collisions with ions or electrons.

2.3.2 INHOMOGENEOUS BROADENING

The primary inhomogeneous broadening mechanism is Doppler broadening, which is due to the motion of the absorbers or emitters with respect to the laser wave vector. The broadened profile is the Maxwellian velocity distribution, Eq. (8), convolved with a Dirac delta $\delta(\nu\text{-}\nu')$, where $\nu'=\nu_o(1\text{-}\frac{v}{c})$. This is effectively a statistical averaging of the velocity distribution, p(v), at a given frequency, ν. The resulting line function for a Doppler broadened spectral line is Eq. (9), with Eq. (10) defining the linewidth [25, 30].

$$p(v) = \sqrt{\frac{m}{2\pi kT}} e^{\frac{mv^2}{2kT}} \tag{8}$$

$$g(\nu - \nu_o) = p(v) * \delta(\nu - \nu') = \sqrt{\frac{mc^2}{2\pi kT\nu_o^2}} e^{\frac{m(\nu-\nu_o)^2}{2kT\nu_o^2}} \tag{9}$$

$$\Delta\nu_D = \sqrt{\frac{8kTln(2)}{mc^2\nu_o^2}} \tag{10}$$

The second major inhomogeneous broadening mechanism is the nonlinear effect from saturation, intensity (power) broadening. If an atomic transition is coherently pumped, the system will undergo Rabi oscillations where the populations of the two states of the pumped transition will oscillate back and forth. Due to the Energy-Time uncertainty principle, this causes the energy level to become broader as the intensity of the pump gets higher. The higher pump intensity increases the Rabi oscillation frequency (see 3.2), which decreases the time an atom is in either of the states at a time [25]. The intensity broadened linewidth is defined in (11) as a scaling factor of the natural linewidth, which is a function of the saturation intensity (12). In this equation, σ is the cross-section and τ is the radiative decay lifetime of the upper level.

$$\Delta\nu_I = \Delta\nu_N\sqrt{1 + \frac{I}{I_{sat}}} \tag{11}$$

$$I_{sat} = \frac{h\nu}{2\tau\sigma} \tag{12}$$

2.4 MULTIPHOTON PROCESSES

While there are many types of multiphoton processes, the processes discussed in this chapter will focus on two-photon processes, or more specifically processes involving the atomic absorption of two photons to excite an atom to a state otherwise inaccessible by a single photon. These processes can occur linearly or nonlinearly, as well as simultaneously or stepwise. These differences will be discussed below. Higher-order multiphoton processes are increasingly accessible with pulsed lasers being commonplace in labs, and with advancements bringing higher powered lasers with compatible optics. Such higher-order processes include high-harmonic generation, sum-frequency generation, harmonic generation, spontaneous parametric down-conversion, and four-wave mixing. While some of these processes can involve only two photons, they are different processes and are excluded from this discussion in order to focus on atomic absorption processes used in this research.

2.4.1 TWO-PHOTON PROCESSES

A two-photon process is any process in which two photons of the same or different frequencies interact with an atomic system nearly instantaneously to excite an atom from a lower state to, in most cases, a higher state (an in some cases lower) that is not accessible through a single-photon process. Because the probability amplitude for simultaneous multiphoton absorption is proportional to the product of the two excitation sources' intensities, two-photon processes, as well as higher order multiphoton processes, are nonlinear in nature with proportionally smaller cross-sections. This leads to high energy, pulsed lasers being used for such processes.

Non-Resonant Two-Photon Processes

A two-photon process is non-resonant when the intermediate level is virtual, which is a state that is a linear combination of wave functions of real transitions with large off-resonance detunings. Non-resonant two-photon absorption is the process in which two photons instantaneously interact with the same atomic system and the sum of the energy of two photons is equal to the energy difference between a ground state and an excited state that is not accessible by excitation from a single photon. Degenerate two-photon absorption is a special case of non-resonant two-photon absorption where the photons have the same frequency, from either the same laser or from a nonlinear parametric process, in which the intermediate level is a virtual state. This process is also differentiated from other two-photon processes,

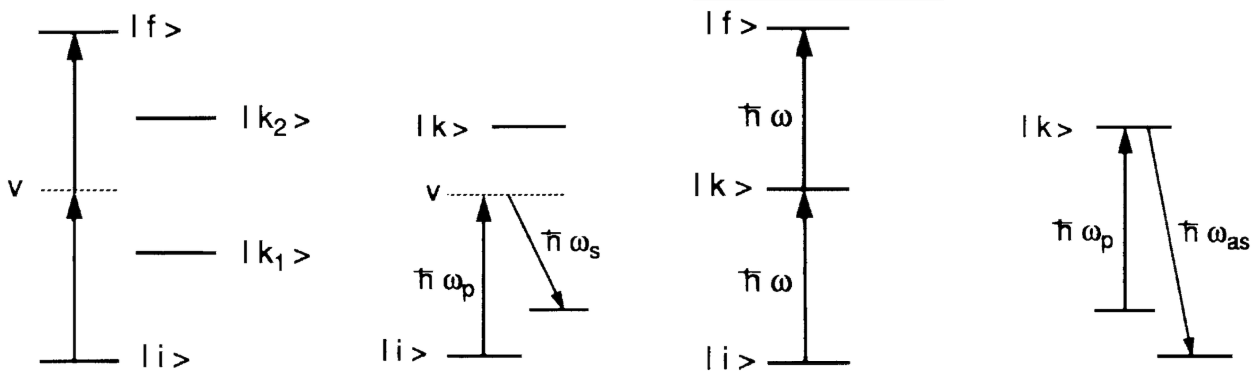

(a) Non-resonant TPA (b) Non-resonant Stokes Raman (c) Resonant TPA (d) Resonant anti-Stokes Raman

FIG. 3. a) Non-resonant, or coherent, TPA. b) Coherent Stokes Raman transition. c) Resonant TPA. d) Resonant anti-Stokes Raman transition. Figure is taken from [31] with license in Appendix E.1.

such as coherent two-photon absorption.

Another non-resonant two-photon process is Raman scattering where a photon inelastically scatters off an atom, exciting the atom to a virtual state and radiating a second photon to a final state. If the final state is higher than the initial state, this radiation is called Stokes radiation. If the final state is lower than the initial state, the radiation is called anti-Stokes radiation. This scattering is referred to as superelastic photon scattering [31]. The differences in these processes can be seen in Fig. 3, compared to a few resonant processes described in the following section.

Resonant Two-Photon Processes

As the virtual intermediate state approaches a real intermediate state, a resonant enhancement occurs from the two individual single-photon resonances. Once the detuning of the high energy photon from the first excited state becomes zero, this process is referred to as a resonant two-photon process, or incoherent two-photon absorption. This process can be modeled as a rate equation approximation of non-resonant two-photon absorption [32]. Just as in non-resonant two-photon absorption, due to parity conservation, this second excited state cannot be accessed via a single-photon process, and the same selection rules apply. The benefit of this resonant two-photon process over the non-resonant process is

that the fluorescence signal can be much stronger due to the resonance enhancement and that when the two transitions are not saturated, the fluorescence depends on the product of the intensities while the absorption of each transition is linear. For the non-resonant case, absorption and fluorescence are always nonlinear. However, Doppler-free two-photon spectroscopy can only truly be done in the degenerate non-resonant two-photon absorption case when all interacting atoms are effectively in the same velocity class [31, 33].

In general, these two-photon transitions where each photon is resonant with a transition are called optical-optical double resonance, which are separated into three processes described below, and shown in Fig. 4. Depending on the intensity of the lower level excitation laser, the absorption coefficient of these double resonances vary between independent (linear process) to linearly dependent (nonlinear process) of the excitation intensities [34]. The similarity between these resonant processes and the non-resonant two-photon absorption depends on the intensities of the two lasers, described below, but also on the relaxation rates of each level involved. In section 3.1, the combination of these double resonance transitions and relaxation rates in terms of level populations will be discussed in detail.

The pure absorption double resonance process is called stepwise two-step absorption where the intermediate state is an atomic resonance. Due to the fact that the intermediate state is a real state with a non-negligible lifetime, the two-step process varies between linear, for the case of high intensity pumping to the intermediate state, to nonlinear with respect to the square of the intensities for the case of low intensity pumping to the intermediate state [35]. The two-step excitation method is the excitation scheme used in this research. The high energy photon is in the VUV and the lower energy photon is in the near infrared (NIR). Fluorescence down to the desired metastable state is measured to estimate the number of metastables. This process is commonly used to excite Rydberg states with applications in quantum computing, optical clocks, and fundamental studies [32].

There are two additional types of double resonance processes that fall into this category which are not like the typical two-photon absorption processes previously described. These two processes have different nonlinear mechanisms due to optical bleaching and saturation affecting the populations of the states. However, the non-linearity of these two processes ultimately have nearly identical intensity dependencies.

The first of these two processes is the V-type double resonance, which is the inverse of laser induced fluorescence (LIF), and is called labeling spectroscopy. The second is the Λ-type double resonance, a stimulated, resonant Raman transition referred to as stimulated emission pumping. However, this Raman transition can also occur spontaneously through the

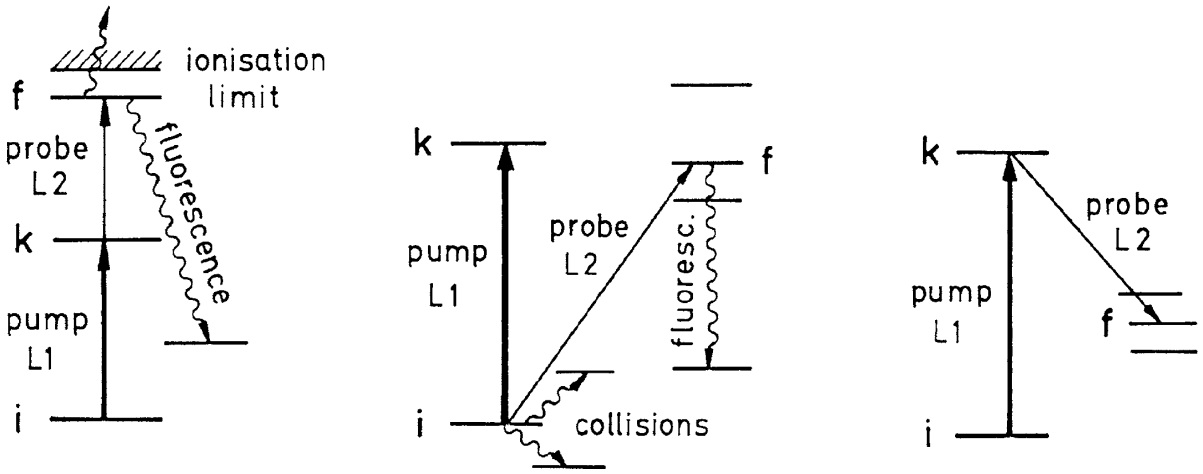

(a) Stepwise-type (b) V-type (c) Λ-type

FIG. 4. Three Optical-Optical Double Resonance Schemes. Figure is taken from [31] with license in Appendix E.1.

pumping of just the first real, excited state and is the resonant case of Raman scattering noted in the previous section [26, 31]. Stimulated emission pumping is used in photoassociation spectroscopy in which two cold, colliding atoms are excited into a stable vibrational level. The resulting interactions can then be probed using stimulated emission spectroscopy. More on photoassociation spectroscopy can be found in [36] on the $RbAr^*$ heterodimer.

CHAPTER 3

FUNDAMENTALS OF LASERS IN ATOMIC PHYSICS

Lasers gave spectroscopy an entirely new dimension by allowing spectroscopists to use light that is spatially and temporally coherent. Lasers have the unique ability to have a very narrow bandwidth, the ability to scan this narrow bandwidth light source across regions of special interest, as well as achieve ultrashort pulses to probe atomic and molecular interactions and chemical reactions. While there is a long list of laser types, the two types of focus in this dissertation are the diode laser and the gas laser.

Driving an atomic or molecular species with a laser in a complete manner (including coherence) requires a more complicated theoretical description than incoherent sources. Section 2.2 described the use of Einstein coefficients to describe incoherent light interactions with an atom. A more quantum mechanical approach needs to be taken for coherence, which is a purely quantum affect than can be approached semi-classically.

3.1 PRINCIPLES OF DIODE AND GAS LASERS

Gas lasers were the predecessor to diode lasers due to the technology available at the time. Atomic gases could be pumped with high intensity flash lamps, which are still used to this day for high-intensity pulsed lasers. However, due to the electrical inefficiency of this process, the advent of the laser diode has moved much of the attention and use of lasers from gas lasers to diode lasers, or solid-state lasers in general. While gas and diode lasers will be briefly discussed, the specifics of how a laser is formed will be discussed in sections 3.2 and 3.3.

3.1.1 GAS LASER DESIGNS

Gas lasers involve the optical pumping of an atomic or molecular gas. The gas is typically excited out of the ground state using an electrical discharge that non-selectively populates many states in a plasma through electron bombardment. The non-selectivity is part of why gas lasers are electrically inefficient, as well as energy loss through heat.

Often, an atomic species will be combined with a molecular species, where the atomic species is easier to excite to a specific state due to it having fewer energy levels. Then,

collisions will transfer the energy from the atomic species to the molecular species, where the molecules can then fluoresce on one of many lines due to the complicated molecular energy level structure. This allows several lasing wavelength options in many gas lasers with the difference being only the coatings of the laser resonator mirrors, which, along with the resonator length, will select the lasing mode.

The typical construction of gas lasers, such as He-Ne lasers, CO_2 lasers, or rare gas ion lasers, can be seen in Fig. 5. The gas is typically contained in a sealed reservoir with electrodes at either end to apply a large electric field. The example in Fig. 5 shows a gas bypass tube, which is sometimes included to help eliminate pressure gradients due to gas pumping. This pressure gradient would hinder the performance of the laser due to a length dependence of the optical gain. In addition to the gas bypass tube, water cooling tubes are often connected to a water reservoir surrounding the gas reservoir in order to cool the laser to maintain steady performance.

The gas reservoir is enclosed in an optical resonator, where one mirror is usually a very high reflector, and the other is a lower reflectance output coupler. Brewster windows are typically used to limit the internal cavity losses and control polarization. For lasers that can operate at multiple wavelengths, an intracavity prism is used to select which wavelength the laser will operate on. For lasers that can lase at multiple wavelengths, but no selectivity is desired, this can be achieved by using specific bandpass coatings for the cavity mirrors.

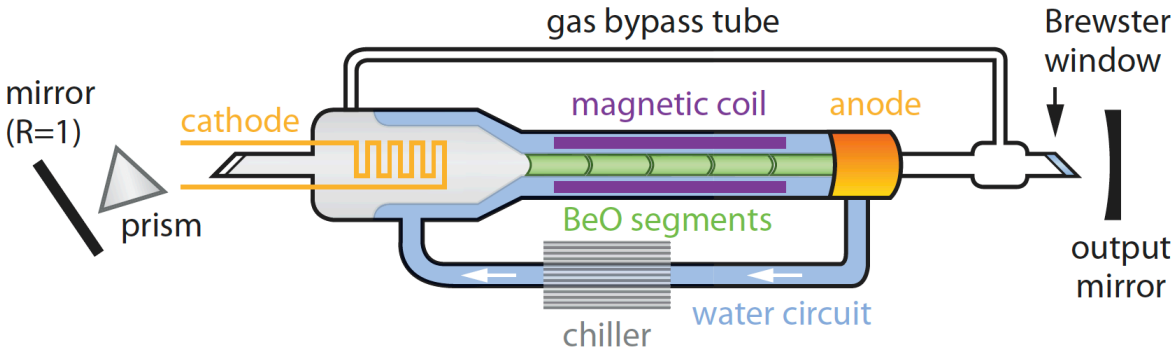

FIG. 5. Typical configuration of a gas laser. This particular diagram shows a setup specifically for an ion laser due to the inclusion of magnetic coils to confine the plasma close to the optical axis. Figure is taken from [37] with license in Appendix E.2.

3.1.2 DIODE LASER DESIGNS

Diode lasers revolutionized the laser industry, as well as research in an array of fields. Diode lasers have significantly higher efficiencies (wall plug efficiency), which lead to power scalability with moderate cooling solutions. Diode lasers are also designed to be operated near room temperature without the need for heating to increase efficiency, for example heating a gas in ion lasers increases the efficiency of excitation out of the ground state, but limits ion lasers lifetimes. Neutral atom lasers do not require the energy to ionize, like in ion lasers, and can thus operate at lower temperatures. However, room temperature fluctuations can still affect both ion and neutral atom lasers if the cavity is not sufficiently resistant to thermal expansion.

Another advantage of diode lasers is the ability to engineer the layers to produce a wide range of wavelengths that are inaccessible when reliant on suitable atomic or molecular states. This design freedom has largely allowed the discontinuation of the use of dye lasers, which were the tunable laser of choice, and what enabled the first magneto-optical trap to be created.

In a pure, intrinsic semiconductor, the carriers do not have the thermal energy to flow at low temperatures and the semiconductor acts as an insulator. At higher temperatures, some electrons make it across the band gap to create vacancies. This allows current to flow under certain conditions. If a voltage is held across the device, the free carriers of a semiconductor at a finite temperature allow a small current to flow.

In order for semiconductors to be useful as electronic devices, doped semiconductors are butted up against each other to create an intrinsic electric field after charge carriers neutralize in a depletion region near the junction. Under a reverse bias, the depletion zone increases, and the semiconductor becomes sensitive to light (photodiode) but is otherwise an insulator (other than thermal leakage currents). Under a forward bias, the depletion zone decreases and current will flow due to the internal electric field being overcome and allowing diffusion to occur once again. If the band structure is indirect, only current will flow due to recombination requiring a change in momentum that occurs through a phonon interaction (energy absorbed into the lattice). In a material with a direct band gap, the momenta of the two bands are matched, and thus recombination can occur with the energy being emitted through spontaneous emission.

Laser diodes are made of material combinations to create a direct band gap structure where carrier momenta are the same and thus radiative recombination can occur rather than non-radiative recombination with the lattice. Since direct band gap materials are already

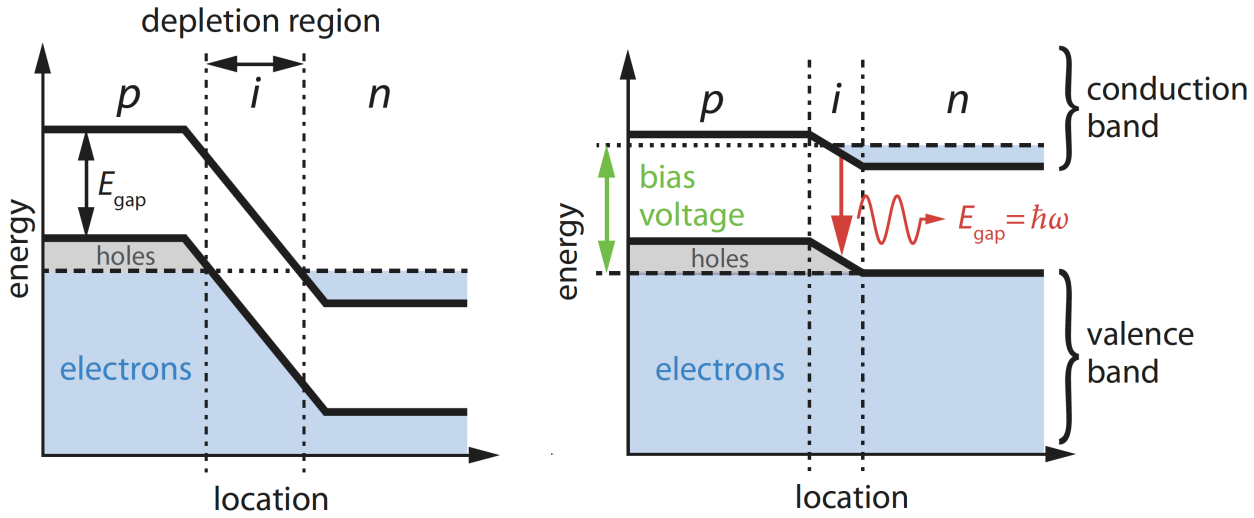

(a) Unbiased PIN diode laser.

(b) Forward biased PIN diode laser.

FIG. 6. Unbiased and forward biased PIN semiconductor showing how the forward bias voltage enables physical overlap of carriers in the depletion region. Figure is taken from [37] with license in Appendix E.2.

engineered materials, the diodes are also engineered with two or more doped semiconductor regions to increase the carrier densities in their respective bands. Thus, when a forward bias voltage is applied, the increased carrier densities in the doped regions allow higher carrier densities to diffuse into the depleted junction region formed between the two doped semiconductors. This results in more radiative recombination in the depletion region. The intrinsic depletion region can be designed with a higher index of refraction than the doped regions. This higher index of refraction will result in more internal reflections, creating a waveguide between the two doped semiconductors. This waveguide is what allows the spontaneous emission to build up in a cavity formed by reflective surfaces on either side of the depletion region. Once stimulated emission occurs, the emitted photons have the same momenta as the cavity photons. This results in the highly directional beam that lasers are known for.

An example of how a forward bias affects the energy bands across the structure of the diode can be seen in Fig. 6. Diodes can be designed using a heterostructure design that further allows more carrier confinement in the depletion region for more efficient lasing. More thorough discussions of diode laser theory, different types of diode lasers, and their applications can be found in [38–40].

The laser design that is ubiquitous in the field of atomic and molecular physics, because of its tunability and narrow linewidth, is the external-cavity diode laser (ECDL). This design creates an optical resonator external to the diode substrate, enabling the addition of a dispersive element for wavelength selectivity and lengthening the cavity for a much narrower linewidth. Anti-reflection (AR) coated facets are typically used to fully utilize the potential gain of an ECDL. Either both facets can be AR coated to put the diode between two external cavity mirrors, or just one facet can be AR coated while the other is used as the high reflector of the cavity.

The two commonly used types of ECDL are the Littrow and the Littman-Metcalf. The Littrow ECDL uses a diffractive element, typically a grating, to feed the first-order reflection back to the diode, closing the cavity, to reinforce the lasing of a specific wavelength. The zeroth-order reflection is sent to the experiment. Using the zeroth-order beam maximizes energy output, but the tuning of the standard Littrow configuration changes the output beam's direction. A modification of the Littrow, using turning mirrors, can eliminate the change in the beam's output direction while tuning.

The Littman-Metcalf configuration also has the diode's beam incident on a diffractive element, again typically a diffraction grating, but this time the first-order beam goes to a mirror and is retroreflected back to the diffraction grating. Then, the first-order reflection of the retroreflected beam is sent back to the diode, closing the cavity. The output beam is still the zeroth-order of the first reflection off the diffraction grating, but the beam is incident on the diffraction grating at a grazing angle such that much less power is in the zeroth-order of the grating. This means that, while the output direction of the Littman-Metcalf is constant as the wavelength is tuned by turning the mirror, the efficiency is much less than the Littrow configuration. The book Tunable External Cavity Diode Lasers covers these designs and more in great detail [41].

3.2 LASER-DRIVEN ATOMIC SYSTEMS

Atomic systems have been probed long before the advent of the laser. Incoherent sources, such as arc lamps, were the foundation of spectroscopy for decades, while flame sources and the sun were used before that. As technology advanced, incoherent sources could be filtered to be, albeit poor, coherent sources. These were the first footsteps into experimentally investigating more modern quantum theories of light-matter interactions. However, the laser has allowed experimentalists to look into phenomena more exotic than ever before thanks to their high spatial and temporal coherence at high intensities.

Classically, atomic system dynamics can be described by rate equations, which are accurate for incoherent and broadband sources. The rate equation approximation can also hold well for systems driven with weak coherent sources. However, when coherence between states needs to be considered, quantum dynamics need to be taken into account by using a quantum master equation of some sort. The Schrödinger equation is a special case of the Lindblad master equation where only pure states are considered with pure unitary evolution. The Schrödinger equation does not allow for any decoherences, and thus does not allow accurate representation of real (open) quantum systems. An improvement on the Schrödinger equation is to use the density matrix which allows for coherence between states. The use of the density matrix changes the Schrödinger equation to the von Neumann equation. In order to include decoherences to make the system more realistic, decoherence terms are added to the von Neumann equation to include the non-unitary evolution produced by the coupling of the quantum system and the environment. This new equation is a general quantum master equation called the Lindblad equation [32]. The following sections will follow the process of developing a rate equation model and modifying it to include both quantum coherence and decoherences by using the Lindblad master equation. This model will then be applied to a gas laser. The model constructed for this research on the metastable production and rare gas laser can be found in Chapter 7.

3.2.1 RATE EQUATION MODEL

The Einstein A and B coefficients discussed in Chapter 2.2 were developed with the thought construct of the basic processes that can happen when an atom interacts with a photon. This formulation takes into account isotropic radiation that is strongly incoherent, specifically thermal radiation. This limit can be shown through the use of the optical Bloch equations (OBE) in [42], which show the Einstein rate equations (ERE) coming from the assumption of incoherent light. However, Höppner *et al.* also show the rate equation approximation's validity in another limit, being the atomic incoherence limit, rather than the radiation incoherence limit. Here, the atomic transition is broad enough that incoherent light has an effective coherence if narrow enough compared to the atomic transition. Such situations can occur when collisional or spontaneous decoherence rates are significant enough to overpower the coherence rates [29, 43]. This section discusses the ERE, while the OBE will be discussed in the next section using the density matrix formulation.

The Einstein coefficients, defined in 2.2 and quickly reviewed here, represent probability of each respective optical process occurring. They are put into the rate equations by converting

them into rate coefficients using other model parameters such as the intensity of exciting light, for the B coefficients, or by analyzing the atomic levels for the A constant. The A constant represents spontaneous absorption and is in the form of a rate (frequency). However, it can vary between being equal to the decay rate to being part of the sum of the decay rate. If the atomic transition is closed, the A coefficient is equal to the decay rate and the inverse of the decay time constant (lifetime). Transition rates, for dipole transitions, are typically lower (with longer lifetimes) as the energy difference between the states gets higher, or the upper level energy gets farther from ground. The closed dipole transitions out of the ground state have the shortest lifetimes due to the strong coupling potential. This can be seen as a consequence of a smaller interaction potential between the electron and the atom as a whole (coupling between the parent ion and the excited electron). Rydberg states are an example of states where the valence electron is (or multiple electrons are) highly excited near the ionization limit and have very long lifetimes due to the weak coupling to ground.

However, more highly excited states are rarely closed, meaning an excited state can decay to multiple lower states. While the spontaneous decay rates (Einstein A) for each transition vary based on the degeneracy and dipole moment, the excited state only has one lifetime, which is the inverse sum of the decay rates of each decay. Therefore, in rate equations, one must use care between when a decay rate is used and when a lifetime is used.

The B coefficients refer to the absorption and emission of a photon by an atom in the presence of an external field, while spontaneous emission (A) occurs even in the absence of fields (excluding vacuum fluctuations in field theory). The two B coefficients must be balanced because they are the opposite processes of each other. However, when including degeneracy of the states, they are not exactly equal and the steady state population in a two-level atom at equilibrium will change by a factor of the ratio of the two degeneracies. An important note to make is that the Einstein B coefficients in the rate equations in this dissertation are formulated as in [29] such that the use of a narrowband light source is used. Therefore, rather than using spectral density, as is used in 2.2 for the basic theory of the Einstein coefficients, this dissertation and the included model use intensity called irradiance in [29]). Hilborn wisely advises to carefully pay attention to units based on the application.

The most fundamental Einstein rate equation is based on detailed balancing, which is only valid at equilibrium (process is reversible and current state only relies on the previous state). This detailed balancing means that the system remains unaffected, even if it interacts with an environment (weakly-coupled environment: Markovian reservoir). What this Markovian assumption defines is that there is no probability flow into or out of the system and that

information is not lost to the environment [44]. This is an important, yet easy to exclude, description of the model because even the density matrix model using the master equation has the Markovian assumption, and it vastly simplifies the system dynamics. However, it is in general a reasonable assumption for ensembles where macroscopic properties are under investigation. Non-Markovian dynamics is an active field of research due to the growing interest in quantum information where information loss of atomic systems to the environment is trying to be minimized/controlled.

The ERE, for a two-level system, with the original assumption of time-independent Einstein coefficients (in 2.2) at equilibrium are seen in Eq. (13). An additional note to the previous discourse on the validity of the ERE is that they derive from the use of first-order perturbation theory. For the full, quantum treatment of light, light cannot be treated as a perturbation [45].

$$\begin{aligned} \frac{d\dot{n}_1(t)}{dt} &= A_{21}n_2(t) - B_{12}In_1(t) + B_{21}In_2(t) \\ \frac{d\dot{n}_2(t)}{dt} &= -A_{21}n_2(t) + B_{12}In_1(t) - B_{21}In_2(t) \end{aligned} \tag{13}$$

The time-dependent B coefficients, derived from non-perturbative origins in the Rabi model, can be seen in Eq. (14), with the corresponding rate equations in Eq. (15). The Rabi frequency, Ω, is defined in Eq. (20), and the derivation of the time-dependent B coefficients is covered extensively in [46]. These equations, like Einstein's, only hold for thermal, incoherent, light but include Rabi oscillations in the incoherent regime from weak to strong coupling. While the density matrix model in the next section includes Rabi oscillations in the coherent regime, the model does not include incoherent Rabi oscillations and assumes weak coupling for the incoherent sources. Islam *et al.* found the time-dependence of the B coefficients to drive the system away from equilibrium in the case of strong coupling, opposite of Einstein's predictions. However, the original ERE results are recovered when the Rabi frequency goes to zero.

$$\begin{aligned} B_{12}(t) &= \left(\frac{\pi}{3\epsilon_0\hbar^2}\right) |\langle\psi_1|\vec{d}_{12}|\psi_2\rangle|^2 |J_0(\Omega_{12}t)| \\ B_{21}(t) &= \frac{g_2}{g_1}B_{12}(t) \end{aligned} \tag{14}$$

$$\begin{aligned}\frac{d\dot{n}_1(t)}{dt} &= A_{21}n_2(t) - B_{12}(t)In_1(t) + B_{21}(t)In_2(t)\\ \frac{d\dot{n}_2(t)}{dt} &= -A_{21}n_2(t) + B_{12}(t)In_1(t) - B_{21}(t)In_2(t)\end{aligned} \tag{15}$$

3.2.2 DENSITY MATRIX MODEL

The largest deviation from the full quantum treatment of this system that is presented in this work is treating the laser field as a classical electromagnetic field. A more thorough derivation of this method can be found in [45]. For a derivation of the master equation in non-relativistic field theory, refer to section 75.8 of [32].

Using the Schrödinger equation, Eq. (16), the wave equation for the atom can be represented by Eq. (17), where $\zeta_n(t) - \zeta_m(t) = \omega_{nm}t$ is a time-dependent phase factor and the sum only includes the atomic levels of interest in the system under study. The potential, V(t) in equation 19, is the time-dependent potential the atom experiences from the interaction with the light. Here, the electric field is seen in Eq. (18), where the approximation represents the dipole approximation of a plane wave. The approximation of the laser as a plane wave is valid within the Rayleigh length, which increases quadratically with the beam waist. However, a narrowband laser is still coherent over a long distance (1 km for $\Delta\nu \approx$100 kHz). This complicates the model for a laser exciting an atom in the far field that can still coherently drive a transition.

The potential in Eq. (19) is transformed to be in terms of the transition dipole moment, and then the Rabi frequency, Eq. (20). The top half of the potential equation is general for all of the matrix elements, while the bottom half of the equation is in terms of the matrix element [g,e], where g is the lower state and e is the upper state of a particular transition. The Rabi frequency is also expressed in terms of properties that are generally more well known about a system and is used in the numerical model discussed in Chapter 7. The λ_{ge} is the wavelength of the exciting or emitted light from the transition from level g to level e, Γ_{ge} is the rate of spontaneous emission from level e to level g, I is the intensity of the driving laser, and j is the total angular momentum of the transition levels.

$$i\hbar\frac{\partial\Psi(t)}{\partial t} = (H_o + V(t))\Psi(t) \tag{16}$$

$$\Psi(t) = \Sigma_n \rho_n(t)\psi_n e^{-i\zeta_n(t)} \tag{17}$$

$$\vec{E}(\vec{r},t) = E_o e^{i(\vec{k}\cdot\vec{r}-\omega t)} \approx \frac{E_o}{2}(e^{i\omega t} + e^{-i\omega t})\vec{\epsilon} \tag{18}$$

$$\begin{aligned} V(t) &= -e\vec{E}(\vec{r},t)\cdot\vec{r} = -e\vec{E}(\vec{r},t)\cdot\langle\psi_g|\,\vec{r}\,|\psi_e\rangle \\ &= \frac{\vec{d}_{g,e}\cdot\vec{E}(\vec{r},t)}{2}(e^{i\omega t} + e^{-i\omega t}) = \frac{\hbar\Omega_{ge}}{2}(e^{i\omega t} + e^{-i\omega t}) \end{aligned} \tag{19}$$

$$\Omega_{ge} = \frac{\vec{d}_{g,e}\cdot\vec{E}(\vec{r},t)}{\hbar} = \sqrt{\frac{2j_e+1}{2j_g+1}}\left(\frac{\lambda_{ge}^3\Gamma_{eg}I_{Laser}}{2\pi hc}\right) \tag{20}$$

After simplifying Eq. (16), the equation is in the form of the von Neumann equation, which is the density matrix generalization of the Schrödinger equation. The von Neumann equation can be seen in Eq. (21), which, at this point, is still representative of a closed quantum system without decoherence. During the process of plugging the wave equation, Eq. (17), into the Schrödinger equation, oscillating terms show up in the coherence terms from the differences between time dependent phases in the wave equation sum. The rotating wave approximation is applied where slowly oscillating terms (with $\delta \approx 0$) are approximated to 1 and fast oscillations (2ω) are averaged to 0. This will be shown in the density matrix model in Chapter 7 [47].

In order to add the decoherence, additional terms are added giving the Lindblad master equation, Eq. (22). Additional rate constants will be added to the model for decoherence due to atomic collisions in the experiment, which act as decay constants from one state to another, just as the spontaneous emission rate constant and the spontaneous/stimulated absorption rate constants for incoherent light [7]. A simple case of a three-level system where the pump is driven coherently and the excited state fluoresces down to a metastable state can be seen in Eq. (24).

Together, the NxN density matrix formulation in the Lindblad equation express N^2 differential equations that represent the semi-classical optical Bloch equations. While the system may produce N^2 differential equations, the minimum number to fully solve N pure states

is $\frac{N(N-1)}{2}$ complex differential equations. This reduced system of equations is due to the property that $\rho_{i,j} = \rho^{\dagger}_{j,i}$. The Lindblad system differs from the case of the Schrödinger equation, which is solving N real differential equations for N pure states. In the Lindblad master equation, Eq. (22), σ is as defined in Eq. (23) and $|i\rangle$ is the state vector. For more on the Dirac formalism of using Bra-Ket notation for state vectors, see Chapter 3 of [48].

$$i\hbar\frac{\partial\rho(t)}{\partial t} = [H, \rho(t)] \tag{21}$$

$$i\hbar\frac{\partial\rho(t)}{\partial t} = [H, \rho(t)] + \sum_{g,e=1}^{N}\left(\Gamma_{eg}(\sigma_{ge}\rho(t)\sigma_{eg} - \frac{1}{2}[\sigma_{eg}\sigma_{ge}, \rho(t)]\right) \tag{22}$$

$$\sigma_{ge} = |g\rangle\langle e| \tag{23}$$

$$\begin{aligned} V(t) &= -e\vec{E}(\vec{r},t)\cdot\vec{r} = -e\vec{E}(\vec{r},t)\cdot\langle\psi_g|\,\vec{r}\,|\psi_e\rangle \\ &= \frac{\vec{d}_{g,e}\cdot\vec{E}(\vec{r},t)}{2}(e^{i\omega t} + e^{-i\omega t}) = \frac{\hbar\Omega_{ge}}{2}(e^{i\omega t} + e^{-i\omega t}) \end{aligned} \tag{24}$$

3.3 THE OPTICALLY PUMPED GAS LASER

The previous two sections on the rate equation model and the density matrix model can be applied to physical systems that have many levels. Rate equations are often used to successfully model multilevel lasers. The minimum number of levels required for a laser are three, due to the necessity of what is called population inversion. Population inversion is when atoms are pumped into a slowly decaying state that allows for more population in an excited state than the ground state. This is not possible with two levels because a true two-level system can only equilibrate to equal populations due to each level having no degeneracy (otherwise it is more than two levels). However, when looking at two levels of a real atom, the states can be degenerate, and the equilibrium is a ratio of the two degeneracies. In the presence of a perturbation, such as a photon, the degeneracy is lifted, and the photon will excite a particular level based on polarization or some other property.

The basic laser is the three-level laser where the ground state is the ground state, or a metastable state, that either doesn't decay or decays very slowly. Atoms in the ground

state are pumped to an excited state that then non-radiatively (collisionally) decays very quickly to a third level. Then, the decay from the third level to the ground state is relatively slow. The long decay from the third level is what enables the population inversion where the majority of the atoms are in the third state. The atoms then radiatively relax to the ground state. When in an optical cavity, the spontaneously decayed photons stimulate more decays. The stimulated emission builds up with common phase and frequency, which leads to the high coherence of laser light.

The more levels the laser system operates on, the more efficient because it introduces more longer-lived levels for population to build up. For a four-level laser, atoms in the ground state will be pumped to a short-lived state that non-radiatively relaxes to a long-lived metastable state, where the population builds up for population inversion. The metastable state slowly radiates to a lower 4th level, but in a laser cavity, begins to radiate faster due to the build-up of stimulated radiation. The fourth state then quickly relaxes, non-radiatively, back to the ground state, which is subsequently pumped back up to the excited state. The four-level laser is more efficient due to the probability of the atom being in the long-lived state, which in the three-level laser is the ground state. In complex laser models, the fast-decaying state populations are often approximated to zero as the atom does not remain in that state long enough to affect the populations of the other states [32].

The typical energy level diagrams for a 3-level and a 4-level laser can be seen in Figs. 7a and 7b respectively [37, 49]. In the rate equations of these systems, the populations of each of the states are expressed, except for the population of the upper state of the non-radiative transitions. This is because the transition happens so quickly that the population is effectively zero. The rate equations also include an equation for the laser intensity using the gain of the atomic medium. This laser gain is critical for the laser to reach the lasing threshold where gain overcomes the losses. This laser gain is the major component left out of the rare gas laser model discussed in this work in Chapter 7.

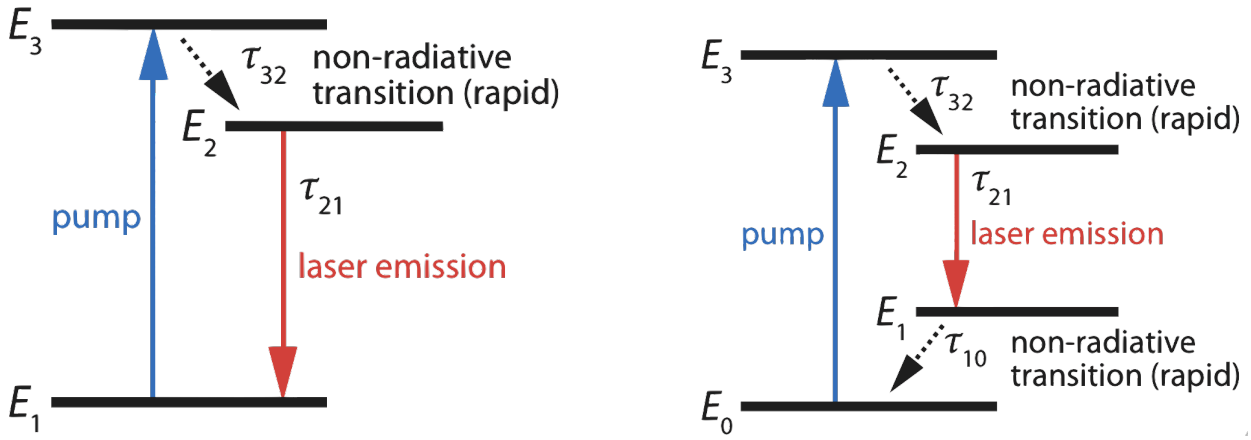

(a) Three-level Laser

(b) Four-level Laser

FIG. 7. Energy level diagrams for a three-level and four-level laser. Figure is taken from [37] with license in Appendix E.2.

CHAPTER 4

THEORY OF OPTICAL RESONATORS

Optical resonators are ubiquitous in the field of physics. Lasers operate on the principle of optical gain from stimulated emission, which would not be possible without the formation of an optical resonator of some type. In semiconductor diode lasers, the resonator may be formed by having high reflectance coatings on the cleaved sides of the diode, which causes light to be trapped in the semiconductor and increasing the optical gain to lase strongly enough for ample light to make it out of the resonator. Some diodes have AR coatings on one side, or both sides, of the diode to be used in an external cavity design, as discussed in 3.1.2.

4.1 OPTICAL PROPERTIES AND TYPES OF RESONATORS

A perfectly aligned and mode-matched cavity's stability can be determined using the inequality $0 < g_1 g_2 < 1$, where g is the cavity stability parameter defined in Eq. (25) with L being the cavity length. Cavities at the bounds of that inequality, 0 or 1, are marginally stable and therefore more sensitive to misalignment. The value of g can be seen in Equation 25, where the indices are mirror 1 for the input coupler and mirror 2 for the output coupler. In this stability parameter equation, L is the cavity length and R is the radius of curvature (ROC) of the mirror.

$$g_i = 1 - \frac{L}{R_i} \tag{25}$$

The two most common types of resonators are the plane-parallel and the confocal. The most basic cavity is the plane-parallel, which is a cavity formed between two plane mirrors. This type of cavity is also called a Fabry-Perot, or etalon. However, the term Fabry-Perot has come to be used as an umbrella term for two-mirrored spherical cavities. The plane-parallel is unique in that, excluding diffraction losses, the mode is the same across the mirror. This means that you can mode-match nearly any sized beam or launch a small beam into the cavity anywhere on the mirror's surface. This allows one to either fill the cavity volume

for as much utilization of a gain medium as possible or even mode-match multiple beams into the same cavity. This is not completely accurate due to the mirror coatings' reflectance values as well as the fact that coatings typically degrade closer to the edge. The mirror also acts as an aperture, so diffraction losses also limit the size of a beam that can efficiently be coupled. However, when the beam waist is a fraction of the size of the mirror, diffraction losses can be disregarded.

Due to the infinite radius of curvature of a plane mirror, a plane-parallel cavity always has the values of g_1=g_2=1. This makes the cavity very difficult to align, along with the fact that having flat mirrors means the effect of mirror walk-off on misalignment is much more pronounced. Cavities with spherical mirrors are much easier to align due to the fact that spherical mirrors make the beam walk-off more slowly than for plane mirrors. Plane-parallel cavities are typically used in high-power applications due to the lack of any focusing in the cavity.

The confocal cavity is when two mirrors with the same radii of curvature are located one radius of curvature away from each other (two focal lengths). This means each mirror has the focal point past the opposite mirror. A similar type of cavity is concentric, which is when the mirrors are placed two radii of curvature away so that each mirror focuses to the other mirror's focal point. A modified version of this cavity is when the mirrors have different radii of curvature, and the cavity length is the sum of the focal lengths. On the stability diagram, confocal cavities are at (0,0) and concentric are at (-1,-1), meaning they are also marginally stable. For this reason, they are sensitive to not just tilt alignment, but length adjustment.

Because confocal cavities never focus, the cavity waist is larger than the concentric cavity. The concentric cavity focuses the most of any cavity, limited by its waist, defined as $\omega_o = \frac{2M^2\lambda f}{\pi D}$. In this equation, f is the focal length, D is the diameter, and M is the quality factor where a TEM_{00} has M=1. Higher order modes have a beam quality of M=2n+1 and 2m+1 for the TEM_{nm} mode.

A third, commonly used cavity is the hemispherical or semi-hemispherical cavity. A hemispherical cavity is when one mirror is planar while the other has a radius of curvature equal to the cavity length. A semi-hemispherical cavity is when the cavity length of a hemispherical cavity is less than the radius of curvature of the spherical mirror. A hemispherical cavity is marginally stable while a semi-hemispherical cavity is stable. A semi-hemispherical cavity is bounded on the stability diagram by the hemispherical cavity at (0,1) and the plane-parallel cavity at (1,1).

The hemispherical cavity can be challenging to align because, just as with the confocal and concentric cavities, not only do the mirrors need to be tilt aligned but the length of the cavity needs to be within the Rayleigh range of the radius of curvature of the spherical mirror. However, due to the inclusion of a plane mirror, they are more sensitive to walk-off than the confocal and concentric cavities. The ease of use and the relative insensitivity to mirror spacing of a semi-hemispherical cavity make it a very popular cavity due to its ease of alignment in situations not including high powers (plane-parallel) or experiments needing strong coupling to the field (concentric).

While there are other stable cavity designs, the prior are the main ones used in experiments due to their power handling ability, small cavity waist, or ease of construction. For extremely high-powered applications, unstable resonators are used. Because of their unstable nature, the internal losses of these cavities are quite high. However, they offer the advantage of having very large mode sizes and higher mode selectivity due to the increased diffraction losses for higher order modes. This enables the realization of very high-powered lasers with good beam quality. These lasers do, however, require a gain medium with a large gain factor due to the significantly decreased photon lifetime in the cavity compared to stable resonators.

For the rest of the discussions on optical cavities, R will more often be used to express the reflectance of an individual mirror or the entire cavity. Reflectance is defined as the power reflectivity, which is the square of the coefficient of reflectivity. The coefficient of reflectivity is the complex ratio of the reflected electric field to the incident electric field, where the electric field is complex, while the intensity and power are real measurables proportional to the square of the electric field. Reflectance is the ratio of the total power reflected to the total power incident. Reflectivity, not the coefficient of reflectivity, and reflectance are often used interchangeably, and for simple materials can mean the same thing.

4.2 MATHEMATICAL MODELING OF A GENERAL RESONATOR

For a general, lossy cavity that does not have identical mirrors, the equations for the transmission and reflection of the cavity are not as straight forward as in most texts that often use lossless and/or identical mirrors. Equations (26)-(29) were derived, as a function of detuning from resonance, using the same technique as in [50–52] through the use of treating the repeated reflections as a geometric series. Here, the detuning, ϕ, is scaled by the FSR where whole integers of π are resonance and half integers of π are antiresonance. These equations allow for losses in the mirrors, such as bulk absorption, and in the cavity. For

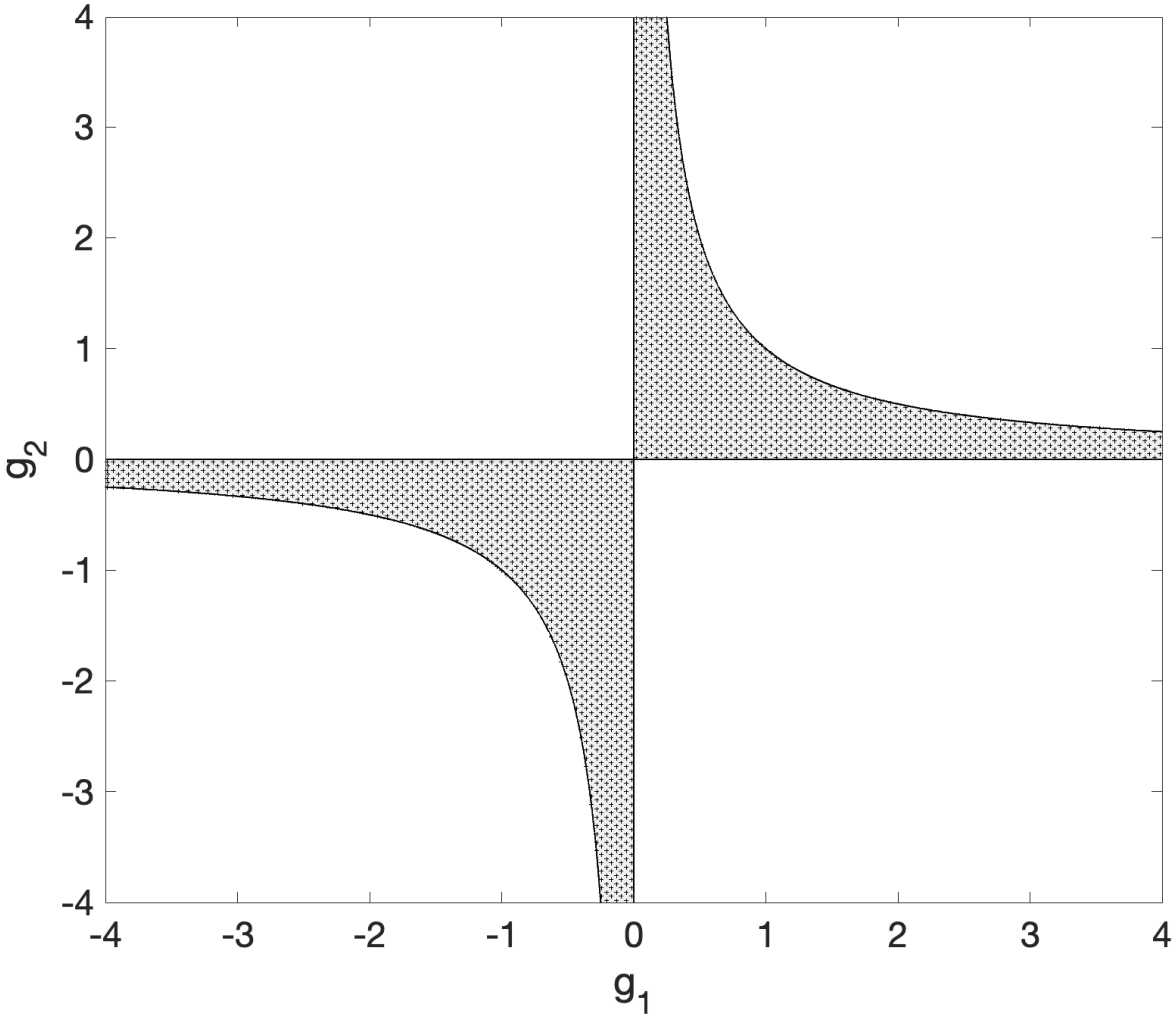

FIG. 8. Stability diagram for spherical cavities. Cavities inside the hatched area representing $0 < g_1 g_2 < 1$ are stable.

each mirror, T+R+L=t^2+r^2+l^2=1. While the mirror loss term accounts for both absorption and scattering, scattering is a difficult parameter to measure in high reflectance mirrors, while absorption is often taken as scattering subtracted from total losses, which is typically measured by cavity ringdown.

The cavity has a linear loss coefficient, α, that decreases the round-trip build-up of the cavity due to absorption or scattering in the medium. This loss term can be used for modeling cavity-enhanced spectroscopy where the transmission of the cavity will significantly be reduced by absorption losses in the sample. This loss term also plays a role in lasers where absorption and stimulated emission occur, and in harmonic generation using nonlinear crystals.

$$E_T = \frac{-t_1 t_2 e^{-\frac{1}{2}\alpha L} e^{-i\phi}}{1 - r_1 r_2 e^{-\alpha L} e^{-2i\phi}} \tag{26}$$

$$T = E_T E_T^* = \frac{T_1 T_2 e^{-\alpha L}}{1 + R_1 R_2 e^{-2\alpha L} - 2 r_1 r_2 e^{-\alpha L} \cos(2\phi)} \tag{27}$$

$$E_R = r_1 - \frac{T_1 r_2 e^{-\alpha L} e^{-2i\phi}}{1 - r_1 r_2 e^{-\alpha L} e^{-2i\phi}} \tag{28}$$

$$R = E_R E_R^* = \frac{R_1 + R_2 (T_1 + R_1)^2 e^{-2\alpha L} - 2 r_1 r_2 (T_1 + R_1) e^{-\alpha L} \cos(2\phi)}{1 + R_1 R_2 e^{-2\alpha L} - 2 r_1 r_2 e^{-\alpha L} \ \cos(2\phi)} \tag{29}$$

An important parameter for a cavity is its quality factor, or Q-factor. This parameter is how damped an oscillator is, just like the quality factor in many other physical systems. However, in an oscillator, it is the damping factor of the light leakage when a resonator is tested under cavity-ringdown. The higher the quality, the longer the light stays in the resonator and the smaller the bandwidth the energy in the resonator is contained. Therefore, the Q-factor is directly related to two critical properties of a cavity, the linewidth and the resonance enhancement factor (intracavity gain).

The most common way to measure the average reflectivity of cavity mirrors is through cavity ringdown, which is measuring the photon lifetime through watching the exponential decay of the transmitted light from the cavity. The cavity linewidth is inversely proportional to the photon lifetime, and directly proportional to the Q-factor. As will be discussed in 7.1,

ringdown was used to measure the first cavity but was removed due to the loss in power in the acousto-optic modulator (AOM) used as an optical switch.

The resonance enhancement can be measured several ways, but the most direct way is that the transmitted intensity is the internal field intensity after passing through the rear mirror (output coupler). Therefore, accurate knowledge of the second mirror's transmittance is what is required. The resonance enhancement can be seen in Equation (30) as a function of detuning from resonance.

$$C = E_T E_T^* = \frac{T_1 e^{-\alpha L}}{1 + R_1 R_2 e^{-2\alpha L} - 2 r_1 r_2 e^{-\alpha L} \cos(2\phi)} \tag{30}$$

CHAPTER 5

FEEDBACK METHODS FOR LASERS AND CAVITIES IN SPECTROSCOPY

Feedback systems are important in nearly all areas of physics, and in the high precision field of atomic and molecular physics they are crucial. Feedback allows the experimentalist to control a laser, atom, or other part of the experiment in a known and controlled manner. A common and easy example of closed-loop control is a piezo actuator. When a piezo has voltage applied to it, it will expand or contract, and it will return to its baseline when the voltage is removed. However, in reality, it will not return exactly to its baseline due to hysteresis. This leads to the use of strain gauges in some piezos that measure the expansion and contraction and feed back to the controller where it actually is so that the system both tells it where to go and makes sure it is where it says it needs to be.

This closed-loop feedback is exactly what is used in laser systems. Lasers are locked to atomic resonances or cavity resonances, atoms can be trapped and moved using magnetic fields and lasers through imaging, and temperature control is often needed for the extreme regulation needed for narrowband lasers. Lasers feature another type of feedback, which will also be discussed later, where light that is fed back to the laser can either cause damage or help stabilize and narrow the laser. There are so many methods and uses for feedback that really make atomic and molecular physics applicable to so many fields.

5.1 FREQUENCY DRIFT

Lasers, and optical resonators in general, have a tendency to drift, whether that be in alignment or in frequency. Thermal drift in a diode laser can be an issue or a benefit depending on the level of temperature regulation. An unregulated diode will drift in frequency due to the fact that a diode laser forms a cavity by having either high or low reflectors on the two facets, depending on the design of the laser. As the laser heats up from lasing, the cavity length changes. This length change causes the longitudinal mode to drift in order to maintain the resonance condition $\frac{N\lambda}{2} = L$ of the lasing mode. If the temperature of the diode is regulated, this thermal drift can be another parameter to use in order to fine-tune

the laser's frequency. It can also be used to stabilize the laser away from a mode-hop if the laser drifts too close to another longitudinal mode, which may begin preferentially lasing.

Thermal drifts also occur in ECDL, such as Littrow or Littman-Metcalf ECDLs described in Chapter 3, by causing either thermal changes in the index of refraction of the air inside the cavity or by causing thermal expansion of the mechanical support of the cavity. To a much smaller extent, thermal drift can also affect the piezoelectric (piezo) element used to scan the cavity if one is used. This particular thermal drift can be eliminated by using strain gauges to feed back absolute position measurements to counteract any thermal drift in the piezo itself. This strain gauge technique also eliminates another type of drift in the form of hysteresis due to the piezo not moving to the expected position during either scanning operations or if the cavity piezo is used as an actuator in closed-loop locking of the laser to a frequency reference.

ECDLs are typically quite small as all of the gain is achieved inside the semiconductor substrate and the distance between longitudinal modes (Free Spectral Range) decreases with an increase in cavity length. As a result, shorter cavities are typically able to scan much farther than longer cavities and can be much easier to mechanically stabilize.

Optical cavities used outside of lasers can often be much larger than an ECDL and usually have very high reflectivity mirrors on both ends. This combination makes optical cavities very sensitive to changes in length compared to the usual ECDL. In this experiment, the primary long-term cavity drift issues are mechanical drift due to lab temperature changes and vacuum chamber pressure changes.

Another disturbance that needs to be counteracted is mechanical vibration. For home-built ECDLs, this can often be an issue but is far less significant for most manufactured lasers due to increased mechanical rigidity and the ability to make small cavities in a much more efficient manner. If one were to monitor a mechanically unstable ECDL on a mechanically stable optical spectrum analyzer (a stable Fabry-Perot optical cavity), one would be able to see mechanical vibrations from acoustic noise in the lab such as the HVAC system, talking colleagues, and even cars driving outside of the building. For an optical cavity with highly reflective mirrors, these mechanical vibrations are even more important, and difficult, to counteract due to the narrow linewidth. If one were to lock to the resonance peak of a highly reflective cavity, the peak is so narrow that even a small disturbance would knock it far from resonance, and it could even jump to an antiresonance. These mechanical vibrations are the primary short timescale corrections when locking a laser or cavity to a frequency reference. In ultra-stable reference cavities, noise can be near the quantum limit where atomic motion

of the mirrors and shot noise of the laser are the limiting factors.

Correcting all of these disturbances can be done several ways depending on the type of laser or cavity. For a diode laser (such as a Fabry-Perot diode laser) one would simply adjust the current or the temperature. For an ECDL, the addition of the external cavity gives one the ability to use the cavity length as a stabilization parameter and if the cavity has a diffractive element, the angle of the diffractive element allows one to shift the frequency selection commensurate with any drift or jitter in the frequency.

Temperature adjustments are the slowest and are typically only used for long-term drifts. However, the temperature is often reserved for tuning the laser frequency to a desired lasing mode or move the laser away from a mode-hop.

Due to the capacitance of piezos, the piezo actuations have a limited bandwidth that is decreased as the load it is pushing/pulling is increased. Therefore, piezo adjustments typically counteract low to medium frequency disturbances below 10 kHz, depending on laser or cavity construction and piezo selection.

High frequency disturbances are corrected by current adjustments due to the ability of most current drivers to respond rapidly and that injection current rapidly affects the current density, changing the index of refraction and therefore changing the effective cavity length. The fact that diode lasers respond quite linearly in frequency to the injection current leads to a straightforward control system that can respond in the radio-frequency range, often above 10 MHz.

These three methods of disturbance correction can be implemented digitally using several feedback loops targeting different disturbance frequency regions, such as using a proportional-integral-derivative (PID) control system, or by using analog electronics and separating the frequency components by using filters or a device such as a bias tee. The error signal that is fed to these control systems can be obtained in many ways that can involve modulation. Modulation techniques often offer lower noise limits due to the 1/frequency noise characteristics of lasers and electronics. Modulation-free techniques offer the benefit of not having any residual modulation in the stabilized laser or cavity and benefit from the reduced cost and complexity of modulators if high modulation frequencies are desired.

While some mechanical disturbances, such as mechanical drifts caused by thermal changes or acoustic vibrations, can be directly counteracted through measurement with strain gauges, other techniques offer finer feedback as well as the benefit of knowing exactly where the laser is in frequency-space by referencing an atomic or molecular transition. This type of stabilization is done through combining control theory with atomic or molecular spectroscopy.

This work will focus on atomic spectroscopy, but while the theory of molecular spectroscopy is quite different than that for atoms, the implementation of such feedback systems is the same. While feedback mechanism will be discussed in this work, theory on actual control system designs to implement a feedback servo will be limited to only the two methods used in this research, which are a home-built feedback servo and the Toptica DLC pro lock.

5.2 FEEDBACK MECHANISMS

Feedback in laser systems can be either optical or electronic. Optical feedback (external) is when light, typically coherent light from another laser or back-reflections from the same laser, causes significant stimulated emission in the laser gain medium. If the optical feedback is undesired, the feedback will cause instability in the laser because it may either cause mode competition in the cavity or it may be out of phase with the laser emission, which can cause amplitude changes. In the case of high-powered lasers, back-reflections can cause serious damage to the laser, especially solid-state lasers. Unwanted optical feedback is corrected with either careful alignment or, more typically, with the addition of an optical isolator.

An optical isolator, specifically a Faraday Isolator, is a magneto-optic device that uses a material that exhibits a strong Faraday effect, which causes the light's polarization to rotate (Faraday rotator), to prevent counterpropagating light from passing back through it. In the Faraday isolator, the Faraday rotator crystal is surrounded by a cylindrical permanent magnet parallel to the optical axis, an input polarizer, and an output polarizer, after the rotator, rotated 45^o with respect to the input polarizer. The light will come out of the isolator rotated 45^o and any light that is reflected back into the rotator will be rotated another 45^o. This results in a polarization that is rotated 90^o from the input polarization, which is rejected by the input polarizer. In this experiment, a Faraday isolator with the polarizers removed was used as a Faraday rotator instead of using a quarter waveplate. A Faraday rotator's polarization rotation is non-reciprocal, unlike a waveplate. This allows for much better polarization extinction in experiments requiring a retroreflected beam's polarization to be perpendicular to the incident beam using minimal optics. The operational principle is demonstrated in Fig. 9.

Optical feedback is not always detrimental, however. External optical feedback is how injection locking/seeding works while internal, rather than external, optical feedback is how the spontaneous emission in a laser resonator builds up to the regime dominated by stimulated emission leading to coherent lasing in a laser. The optical feedback in an ECDL can

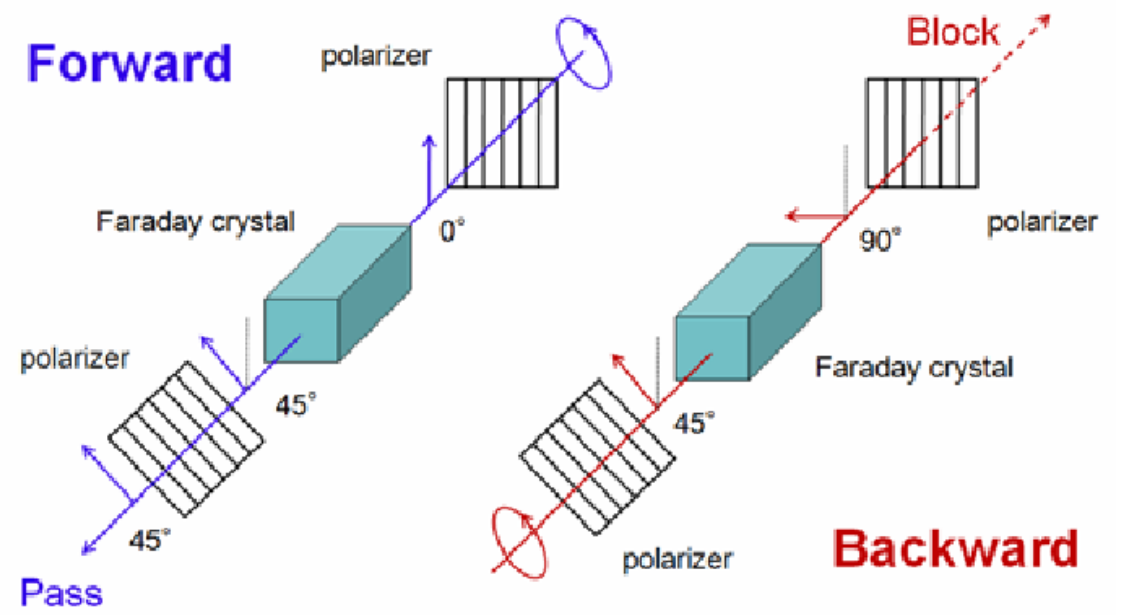

FIG. 9. Functional principles of a Faraday Isolator and rotator showing the non-reciprocity. The figure is taken from [53] and is used under Creative Commons Attribution 3.0 Unported License found at `https://creativecommons.org/licenses/by/3.0/legalcode`.

be described as self-injection locking. Optical feedback is central to the frequency stability, linewidth, and tunability of ECDLs, as discussed in 3.1.2.

5.3 MODULATION-FREE SPECTROSCOPIC TECHNIQUES

There are two main types of spectroscopic techniques used for feedback to stabilize a laser or cavity. The most robust techniques involve modulating a signal in some way to be used to stabilize the desired optical subsystem. However, it is often not desirable to have modulation on a signal. Many types of modulation techniques produce residual modulation, such as residual amplitude modulation, or produce sidebands that may disturb the physical system in an undesirable way. These modulated techniques will be discussed in 5.4.

5.3.1 POLARIZATION SPECTROSCOPY

Polarization spectroscopy is the most common modulation-free technique that is implemented in locking schemes due to its relative ease of setup. While it is not as sensitive as many techniques, if the transition, or other signal, that is being used for locking is strong enough

with a high signal-to-noise ratio, it is a convenient technique that requires no sophisticated locking electronics. This technique is a sub-Doppler method based on the birefringence and circular dichroism of an atomic species that is pumped with a circularly polarized beam and probed with a linearly polarized beam. If the probe's polarization is properly rotated with an "analyzer" half waveplate, the now elliptically polarized probe beam's components can be separated. Subtracting the signals of the two linearly polarized beams from each other produces a dispersion signal that can be used as an error signal. An example apparatus of this technique can be seen in Fig. 10 with more details found in [54].

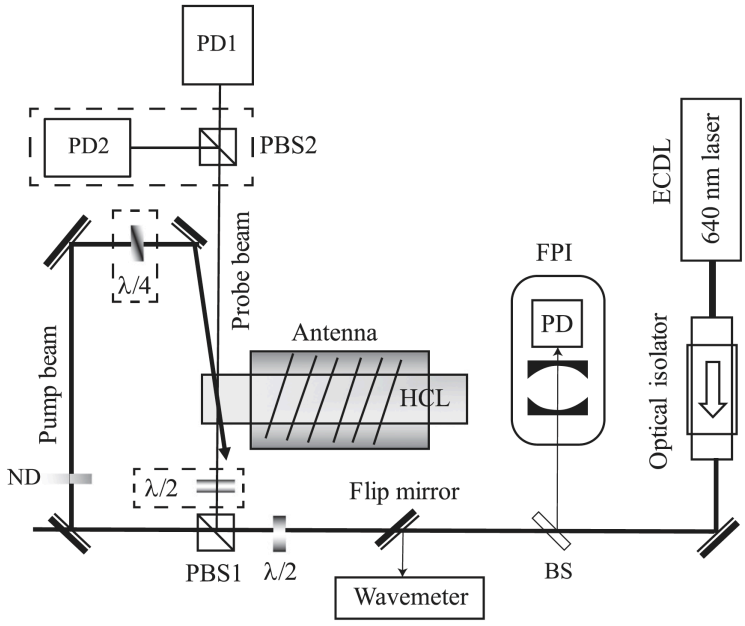

FIG. 10. Polarization spectroscopy experimental setup to obtain a sub-Doppler error signal without modulation. The figure is taken from [54].

5.3.2 TILT LOCKING

The other modulation-free locking technique that will be discussed is one that is particularly useful for locking of an optical resonator based on the sum of the TEM_{00} and TEM_{01} resonator modes. In the single-pass configuration, the Gaussian mode is aligned into the cavity while a tilt produces a non-resonant TEM_{01} mode reflected from the cavity as a phase

reference. The difference between the phases of the two modes is what produces the error signal. In this configuration, as the cavity is scanned, two oppositely signed error signals occur due to the two modes being resonant at different cavity lengths. This causes the reference and cavity modes to switch depending on which one is resonant at a particular cavity length. However, since feedback electronics isolate a particular slope direction, this double error signal has minimal impact on lock stability for a suitably responsive feedback servo.

In order to minimize lock noise and maximize lock response, a double-pass configuration, as seen in Fig. 11, can be implemented to increase the error slope due to the spectral filtering of the cavity. This configuration also eliminates the error signal at the TEM_{01} resonance because the cavity input is aligned so that only the TEM_{00} mode is resonant with the cavity and the tilt is performed on the retroreflection of the Gaussian mode. So, the TEM_{01} mode is only incident on the detector when the Gaussian mode is resonant with the cavity.

While the error signal is sharp for the double-pass tilt lock configuration, it lacks the capture bandwidth of the Pound-Drever-Hall method, discussed in 5.4.3, due to the lack of symmetric sidebands. The single-pass configuration is more similar to the Pound-Drever-Hall method due to the TEM_{01} resonance acting like a sideband on one side of the scan, and offers a similar error slope to Pound-Drever-Hall. However, the capture bandwidth is non-symmetric, which may complicate the feedback servo design. More information on tilt locking can be found in [55, 56].

A similar method, which is a modification of the tilt lock, can be used for atomic spectroscopy by using a Sagnac interferometer rather than an optical resonator. Rather than scanning the length of a cavity across a cavity resonance, a laser is scanned across an atomic resonance. In the case of a Doppler-free saturated absorption spectroscopy signal, the line is a sub-Doppler Lamb dip. More details on this method can be found in [57].

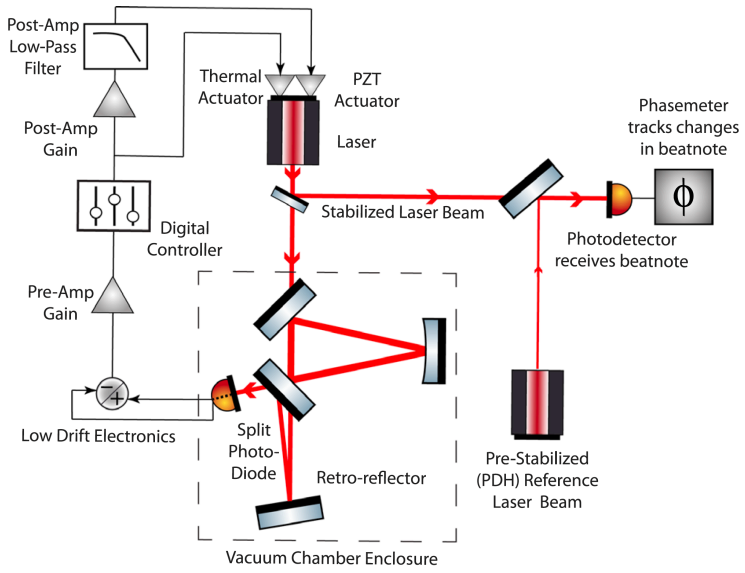

FIG. 11. Tilt locking experimental setup to obtain an error signal from cavity mode interference without modulation. The schematic includes an additional laser stabilized using the modulated Pound-Drever-Hall technique, which is beat against the tilt lock signal. The figure is taken from [56] with OSA open access permissions.

5.4 MODULATED SPECTROSCOPIC TECHNIQUES

Sometimes, modulation is not desired, as described in the previous section. However, an experiment can often be designed such that modulation does not interfere with the experiment in a way as to prevent its use. When possible, modulation-based spectroscopy techniques offer many advantages of modulation-free techniques, such as increased sensitivity and more sophisticated feedback optics. While the latter can provide flexibility, it can also result in increased cost and complexity. However, since laser noise decreases inversely with frequency, the significantly decreased noise floor of RF modulated techniques make these standard techniques for highly sensitive applications.

5.4.1 SATURATED ABSORPTION SPECTROSCOPY

Saturated absorption spectroscopy is the most widely used spectroscopic method for atomic spectroscopy. It is a relatively easy setup that gives very good, Doppler free spectra. This method involves a pump beam and a counter-propagating probe beam. On resonance, the pump beam saturates the transition so that the lower state population of the

transition under investigation is heavily depleted within the linewidth of the laser. The counter-propagating beam experiences a reduced population, which results in a reduction of the absorption, called a Lamb dip. Since this reduction in absorption only occurs when the two counter-propagating beams interact with the same velocity class(es), depending on the linewidth of the laser, the Doppler background is only reduced at the narrow resonance of the transition. The condition of the two beams interacting with the same velocity classes is only met for the atoms that have a Doppler shift less than or equal to the linewidth of the laser. If the experiment is designed properly with a sufficiently narrow laser, the observed linewidth approaches the natural linewidth of the transition.

To eliminate the first-order Doppler profile from the spectrum, a second, offset probe can be used that interacts with a non-pumped column of the sample. The second probe beam then shows only the Doppler background. The second probe beam signal can be subtracted from the first probe beam signal to produce a flat signal everywhere except the narrow Lamb dip on resonance. Figure 12 shows an example of the Lamb dips of the three main even isotopes of Kr, but the background is not flat due to residual Doppler broadening from imperfect matching of the counter-propagating wavevectors. The fitted linewidths of the Lamb dips are larger than the natural linewidth by an order of magnitude due to other broadening mechanisms such as power broadening and pressure broadening. For a detailed overview of saturated absorption spectroscopy, see [58].

5.4.2 FREQUENCY AND WAVELENGTH MODULATION SPECTROSCOPY

While saturated absorption spectroscopy is a sub-Doppler spectroscopic technique, it is not inherently a modulated spectroscopic technique. The spectrum produced is purely just the spectrum, and top-of-peak locking can be performed, which is a modulation-free technique that is typically only performed on very stable signals with a high signal-to-noise ratio (SNR). In order to benefit from the increased SNR of modulating a laser at higher frequencies, the laser must be modulated in some way before interacting with the sample.

For modulated techniques, the modulation depth, β, is how much of the carrier energy is put into the sidebands, and is defined as $\beta = V_{PP}/(2V_{\pi})$. V_{PP} is the peak-peak modulation voltage and V_{π} is the voltage required to shift the phase by π. This means a depth much less than 1 has nearly all of the power in the carrier. When β is above 0.5, the distribution of energy between the carrier and sidebands becomes complicated and the best construction of sidebands desired can be determined through analyzing the expansion of Bessel functions of the first kind, where the Bessel function order corresponds to the order of the sideband.

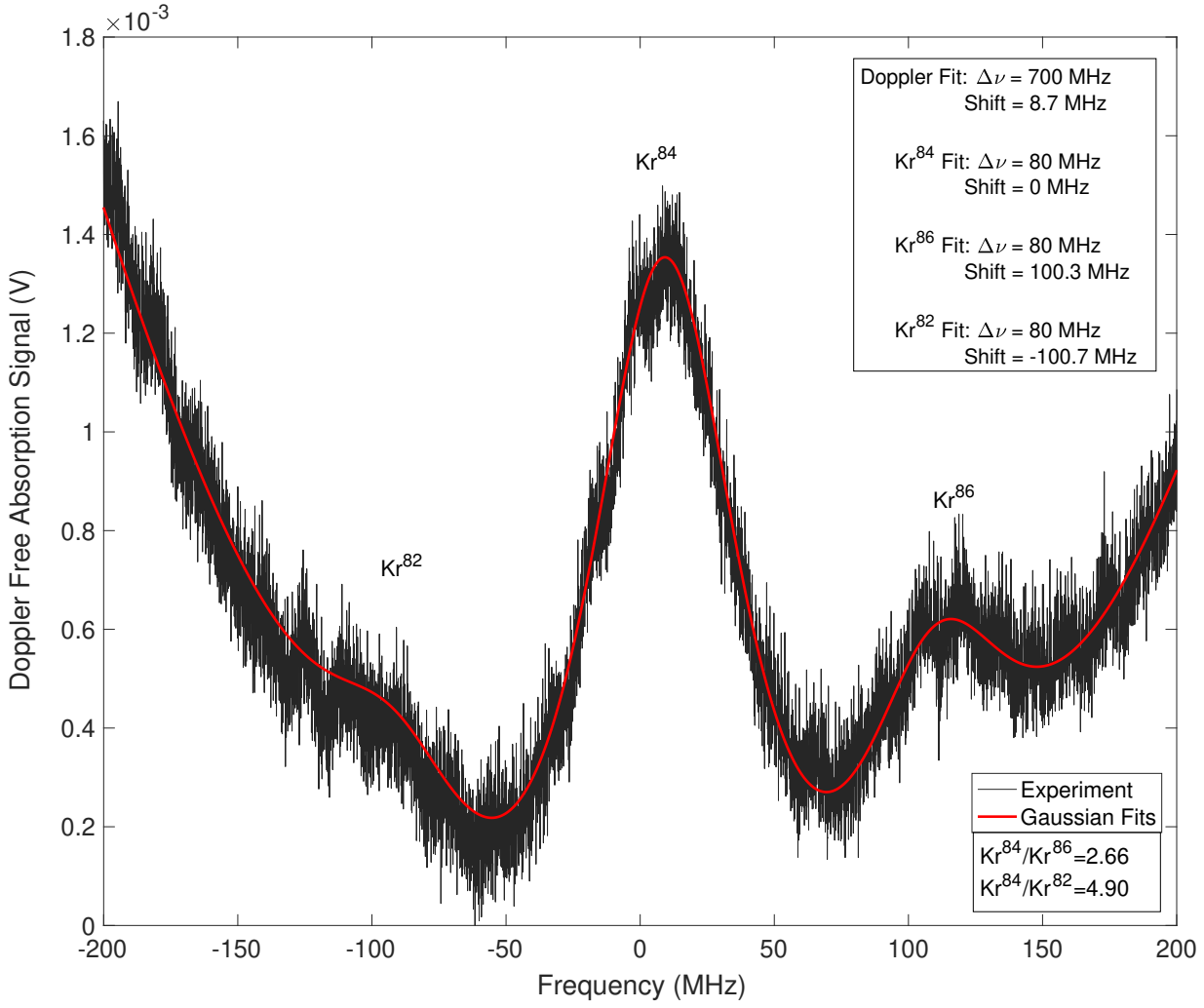

FIG. 12. The isotope shifts of the main even isotopes of Kr were measured using saturated absorption spectroscopy. However, the signal was not stable enough to use for locking. The figure shows Gaussian lineshapes fit to the three isotopes with the ^{84} peak at zero detuning and a Doppler background centered at a detuning corresponding to the center of mass of the even isotopes. The ratios of the amplitudes are also shown. The 84/86 ratio is similar to the natural abundance ratio, while the 84/82 is not as expected due to the low SNR.

Wavelength modulation spectroscopy (WMS) and frequency modulation spectroscopy (FMS) are essentially the same technique with different modulation depths and modulation frequencies. WMS is when the modulation depth is large ($\beta>1$) and the modulation frequency is less than the width of the feature being investigated. This means that the large number of sidebands in WMS are within the linewidth of the feature. As the laser is scanned across the feature, the modulation is sampling the feature by converting the wavelength modulation to an amplitude modulation. This amplitude modulation arises from the fact that as the wavelength oscillates, the absorption at lower frequencies starts to increase closer to resonance. Once on resonance, the oscillations in the wavelength are zero because the modulation frequency is low enough to sample just the peak of the feature for a significant amount of time, and the amplitude doesn't change. Then, as the sweep moves to higher frequencies, the oscillations behave the same as at lower frequencies but with the opposite sign because not the opposite slope is being probed. Together, this produces a dispersion-like signal encoded at the modulation frequency. Using phase-sensitive detection, the derivative signal can be recovered close to DC. WMS is typically used in most general applications of saturated absorption spectroscopy, and the frequencies are low enough to modulate the laser via the injection current (<1 MHz) or the piezo (>10 kHz).

During FMS, the modulation depth is much less than unity ($\beta<<1$) while the modulation frequency is high enough to have sidebands outside of the feature of interest. This results in the feature being probed by the carrier and the sidebands separately, rather than simultaneously as in WMS. FMS can be used on transmission or reflection signals, and absorption is similar in response as the reflection from a cavity. This makes it similar to the cavity locking method described in the next section and used to lock the build-up cavity in this dissertation.

The FMS signal can be tuned with a phase shifter located between the local oscillator and the mixer. The phase shifter tunes the signal between the quadrature signal and the in-phase signal. If the modulation frequency is considered small, the quadrature signal is the signal that is proportional to the derivative of the absorption and the in-phase is proportional to the second derivative of the dispersion. This is the condition of WMS, and the results are as described above. For large modulation frequencies, the in-phase component is the sum of the two sidebands probing the resonance, and a scan results in a negative absorption feature at the negative sideband and a positive absorption feature for the positive sideband.

As the laser is swept in frequency from negative to positive, the positive sideband will

first be absorbed more than the negative sideband, producing a negative feature. On resonance, neither sideband is absorbed, producing no signal. As the sweep continues to a positive detuning, the negative sideband is absorbed, producing a positive feature. When the modulation frequency is on the order of the spectral feature's width, the signal is a pure derivative signal as in WMS. This is because the two absorption signals are overlapped giving the appearance of a dispersion signal. As the modulation frequency increases, the two sideband features separate. This decreases the lock slope but increases the lock capture bandwidth. The major benefit of FMS at high frequencies is the ability to have a decent SNR for the dispersion signal (in-phase component), whereas the dispersion signal is very small for WMS. In the case of a high modulation frequency, the signal can appear similar to the error signal used for locking to the reflection signal of an optical cavity, as described in 5.4.3. This gives the resemblance of the sum of dispersion signals at each resonance, with the slope of the carrier signal being opposite of the sideband slopes. This gives a large error signal slope for locking and a large capture bandwidth. This illustrates the broad applicability of FMS. Mathematical formulations and experimental examples of WMS and FMS can be found in [59–62].

Figure 12 gives the saturated absorption spectrum of the even isotopes with their fitted linewidths. For this work, a modulation frequency of 40 MHz was used. Even though the modulation frequency is quite high, it is not high enough to be larger than the linewidth of the intensity and pressure-broadened atomic transition. This meant the FMS used in this work was effectively WMS, as can be seen by the pure derivative signal in Fig. 13. Note the size and SNR of the error signal, limited by the lock-in amplifier voltage rails, compared to the small absorption signal amplitude and poor SNR. This figure also demonstrates a major drawback of WMS/FMS, which is the fact that it is susceptible to slowly varying background signals. In this work, the slowly varying background signal was the residual Doppler broadening. The scanning of the laser across the background is not modulated, but the Doppler feature is a very broad absorption feature in itself and is therefore sampled the same as an individual Doppler-free absorption line would be. Since the Doppler background is so broad, the Doppler error signal would be WMS, with the zero being centered at the center of mass of the isotopes contributing to the Doppler feature. In practice, due to the residual Doppler broadening, the error signal shape heavily relies on the pump-probe alignment and intensities. Another example of the error signal is shown later in Fig. 21, where the saturated absorption signal is nearly the same, except with an even higher SNR than Fig. 13, but the error signal is more anti-symmetric like a derivative signal without

a background. This difference arose only from changes in the alignment of the two probe beams onto the balanced photodetector.

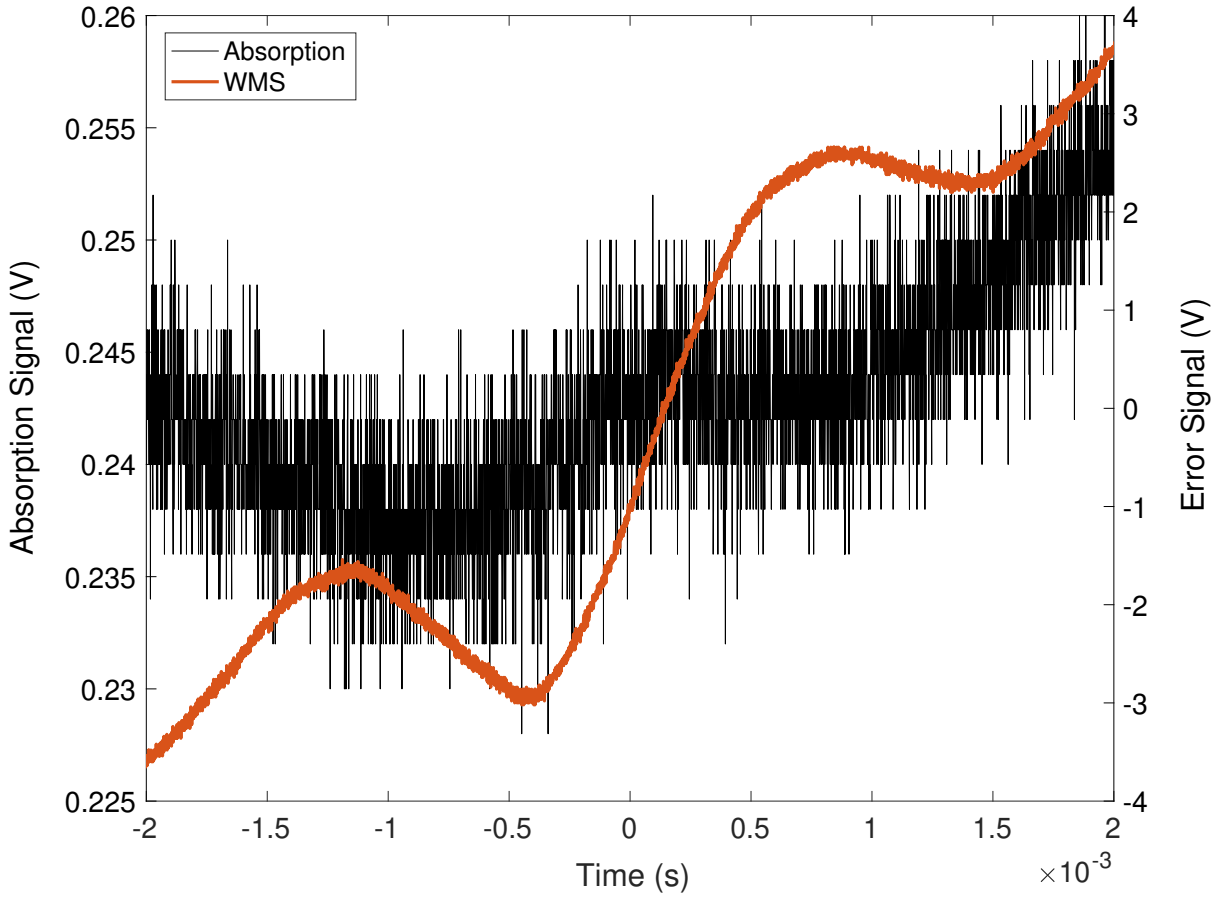

FIG. 13. The saturated absorption spectroscopy signal can be seen with a very low SNR, which would give a very unstable lock. The WMS signal can be seen with a high SNR limited by the lock-in amplifier rails.

5.4.3 POUND-DREVER-HALL

The Pound-Drever-Hall (PDH) technique is very similar to the FMS technique, but the PDH technique relies on the interference between the sidebands with the reflected carrier of a cavity, rather than absorption of the carrier and sidebands. If the modulation frequency is sufficiently large compared to the linewidth of the cavity, the sidebands will completely reflect when the carrier is on resonance. Then, if one sideband is on resonance with the cavity, the carrier and the other sideband will be totally reflected. This gives three resonances with the cavity. In PDH, the modulation depth is typically kept small, as in FMS.

As in FMS/WMS, the in-phase signal is proportional to the dispersion. In a cavity, this absorption would be cavity losses in the mirrors and of a sample inside the cavity. This enables cavity-enhanced FMS. The quadrature signal still represents a signal proportional to the dispersion. This is what is typically considered the PDH signal.

Due to the heterodyning of the carrier with the sidebands, the phases of the beam components are what is being compared, as in FMS. On resonance with the carrier, the beat note between the positive sideband and the carrier exactly cancels out the beat note of the negative sideband and the carrier. This causes the error signal to go to zero. At the resonance of the negative sideband, the beat note of the negative sideband and the carrier cancels the beat note of the positive sideband and the carrier, and vice versa for the positive sideband resonance. The slopes of these two sideband resonances are opposite that of the carrier because of how the reference is taken. For the carrier, the difference is taken from the carrier to the sidebands. For the sidebands, the difference is taken from the sideband to the carrier. The mathematical formulation and explanation of this technique in the complex plane can be found thoroughly derived in [60, 63–65].

When the cavity is not in resonance with either the carrier or one of the sidebands, the signal is non-zero due to the lack of complete destructive interference. How quickly the PDH signal approaches zero between resonances depends on the finesse of the cavity, while how close it gets to zero depends on the modulation frequency. If the finesse of the cavity results in a linewidth close to the modulation frequency, the PDH signal approaches zero slowly outside of the sidebands, and the signal between sidebands is the sum of the interference signals from the resonances. If the cavity linewidth is much smaller than the modulation frequency, the resonances approach zero quickly and have a sharp error signal. However, since there is never complete destructive interference, the signal between the sidebands and the carrier approach but never reach zero. With sufficiently sensitive electronics, high finesse cavities with extremely sharp error signals that go to almost zero are possible as long as the

error signal between sidebands remains above the noise floor of the detection electronics. Ultimately, the result is a strong lock with a capture bandwidth of twice the modulation frequency.

The effect of finesse vs detuning can be seen in Fig. 14. Equations (31) and (32) are the equations used to create the theoretical PDH error signals in this dissertation, where r is the average mirror coefficient of reflectivity and Ω is the modulation angular frequency. It can be seen that as the finesse gets higher, the signal between the sidebands approaches zero, requiring electronics to have a sufficiently low noise floor in order to benefit from the large capture bandwidth the PDH technique offers. However, such a steep error signal on resonance should be sufficient to maintain a lock with a properly designed feedback servo response. The large capture bandwidth is primarily beneficial for large excursions due to large mechanical/acoustic excursions, which are uncommon for modern monolithic cavities in vacuum.

$$F(\omega) = \frac{r\left(e^{i\frac{(\omega-\omega_0)}{\nu_{\text{FSR}}}} - 1\right)}{\left(1 - r^2 e^{i\frac{(\omega-\omega_0)}{\nu_{\text{FSR}}}}\right)} \tag{31}$$

$$\epsilon = -2P_o J_0(\beta) J_1(\beta) \cdot Im\left[F(\omega)F^*(\omega+\Omega) - F^*(\omega)F(\omega-\Omega)\right]; \tag{32}$$

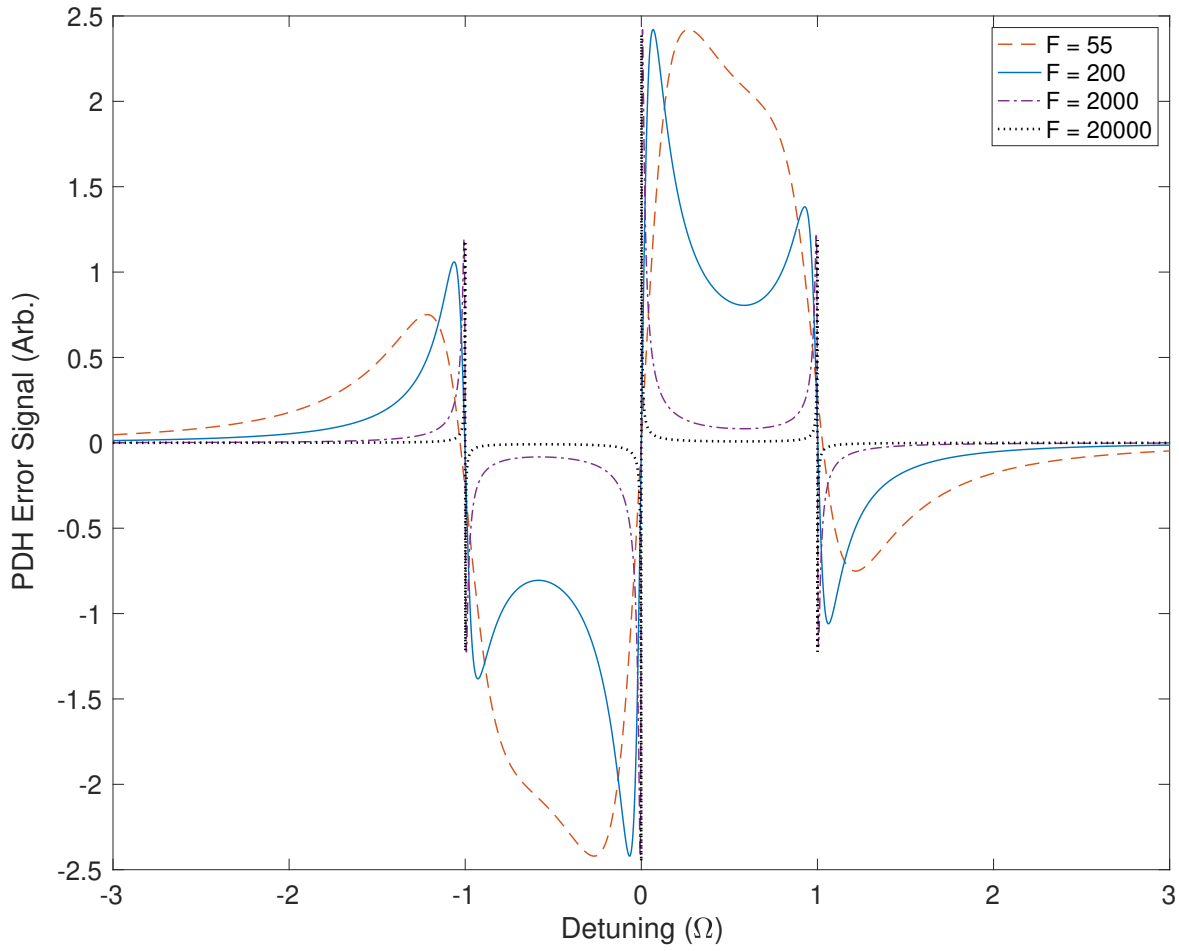

FIG. 14. The PDH error signal is plotted for various finesse values for a cavity that is assumed to be lossless and symmetric. The x-axis is in units of the modulation frequency Ω.

5.4.4 MODULATION TRANSFER SPECTROSCOPY

Modulation Transfer Spectroscopy (MTS) is a sub-Doppler pump-probe technique where a modulated pump beam nonlinearly interacts with an unmodulated, counterpropagating probe beam, which picks up a modulation through a four-wave mixing process. This four-wave mixing process has the two pump sidebands and the probe interacting to produce a sideband on the probe, which can be efficiently detected with phase-sensitive detection. Due to the sub-Doppler condition that has to be met for this mixing, there is zero Doppler background, unlike most other techniques, even FMS. However, a disadvantage in this experiment (or a major advantage in others) is that the four-wave mixing process is more efficient for closed transitions. This means that closed transitions are the dominant feature in the spectra, and that MTS is less efficient for other transitions. This technique was attempted in this research, but FMS was found to be easier to realize and more sensitive with the given conditions.

The MTS quadrature and in-phase error signals can be seen in Fig. 15 and Fig. 16 for different ratios of modulation frequency (Ω) to feature linewidth (Γ). The error signal is expressed in Eq. (33). In this equation, Δ is the laser detuning from resonance, ϕ is the phase with respect to the pump laser, β is the modulation depth, n is the Bessel order, and A contains properties of the species under study. L_n and D_n are defined in Eqs. (34)-(35), where only n=0 and 1 are used when $\beta << 1$ [66–69].

$$S(\Omega,\Delta) = \frac{C}{\sqrt{\Gamma^2+\Omega^2}} \sum_{n=-\infty}^{\infty} J_n(\beta)J_{n-1}(\beta)[(L_{(n+1)/2} + L_{(n-2)/2})\cos(\Omega t+\phi) + (D_{(n+1)/2} + D_{(n-2)/2})\sin(\Omega t+\phi)] \tag{33}$$

$$L_n = \frac{\Gamma^2}{\Gamma^2+(\Delta-n\Omega)^2} \tag{34}$$

$$D_n = \frac{\Gamma(\Delta-n\Omega)}{\Gamma^2+(\Delta-n\Omega)^2} \tag{35}$$

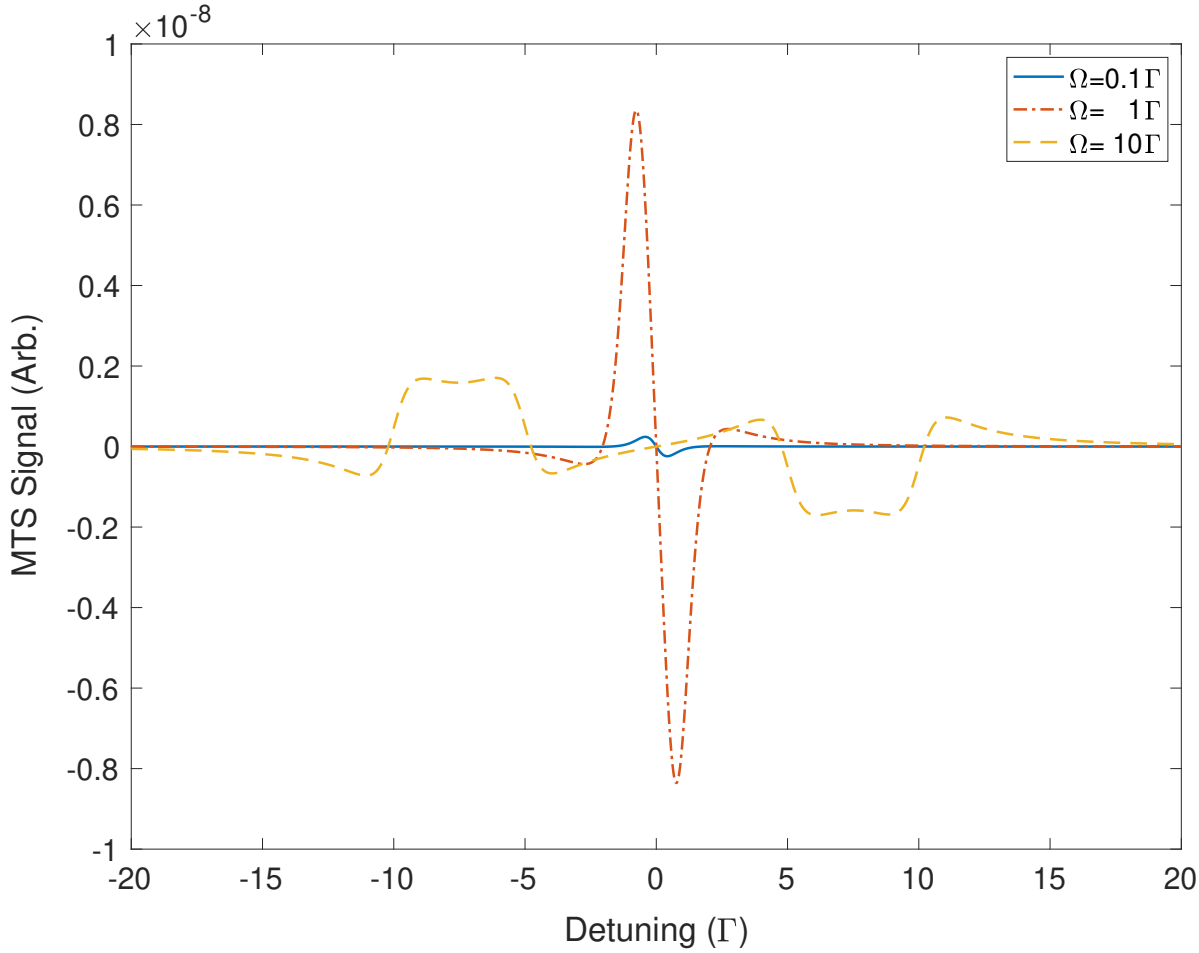

FIG. 15. The MTS quadrature (sine) component of the error signal can be seen as a function of laser detuning and ratio of the modulation frequency to the feature linewidth. The error signal can be seen to be steepest when the modulation frequency is near the linewidth. The detuning is in normalized units of the linewidth.

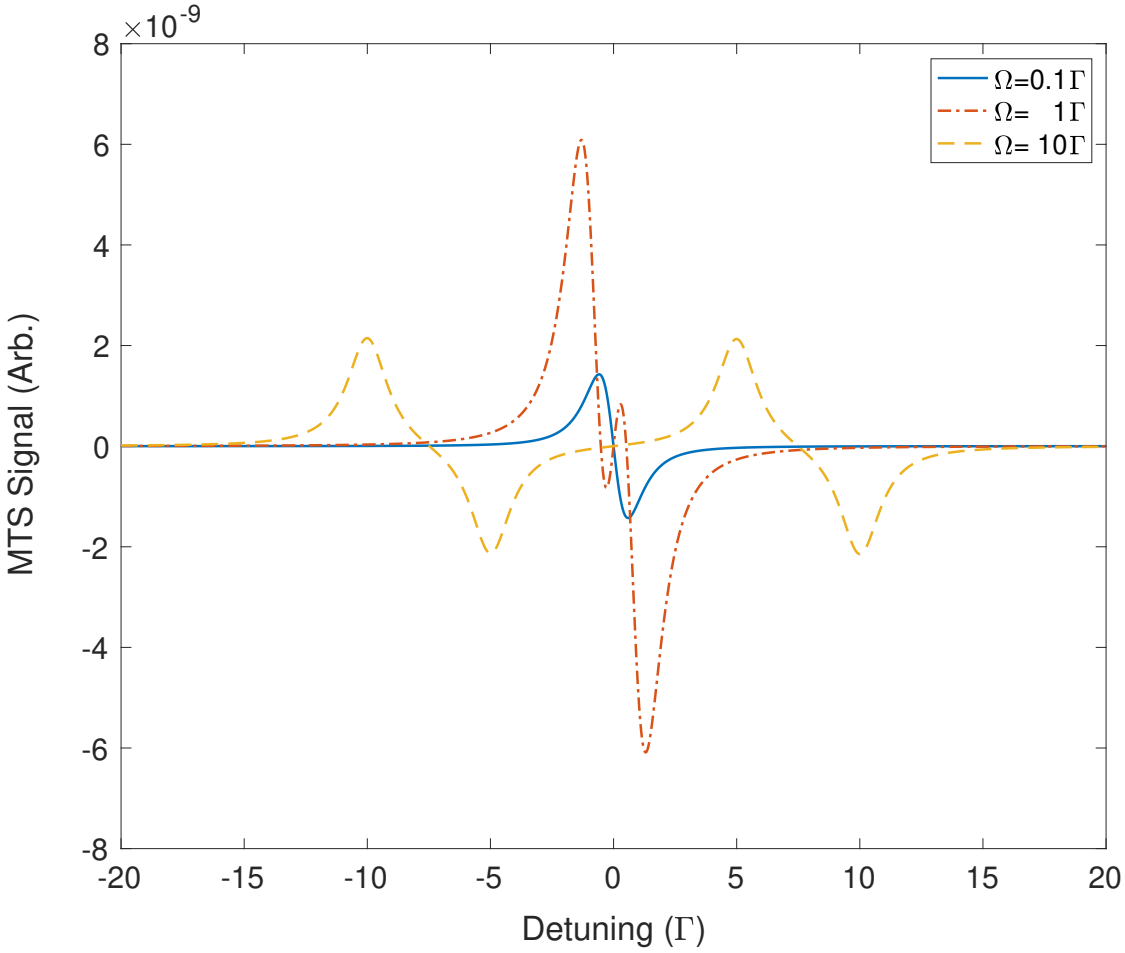

FIG. 16. The MTS in-phase (cosine) component of the error signal can be seen as a function of laser detuning and ratio of the modulation frequency to the feature linewidth. The error signal can be seen to be steepest when the modulation frequency is near the linewidth. The detuning is in normalized units of the linewidth.

CHAPTER 6

EXPERIMENTAL SETUP

The experimental section of this dissertation covers the laser with associated optics for diverting light to other parts of the experiment, the optical cavity where the lamp and laser form the interaction region, and the laser locking cell used as a frequency reference. The following sections will discuss the design and purpose of the components in each of these sections. A rendering of the entire experimental setup, except the Toptica DL Pro, is shown in Fig. 17.

6.1 TOPTICA DL PRO, MODULATION, AND FIBER COUPLING

The laser used to excite the 819 nm transition was a Toptica DL pro with an 805-850 nm AR coated diode that had a free-running wavelength of 835.92 nm. The quoted linewidth of the diode used was approximately 200 kHz. Being AR coated, it was designed to run in an external-cavity, with the DL Pro series being a modified Littrow configuration. An AR coated diode means that the diode resonator has a significantly lower finesse (low reflectivity), and thus a significantly higher threshold current. This is why the Toptica DL pro, while free-running outside of external-cavity conditions, will have significantly lower power at the same current as when in external-cavity or if a Fabry-Perot diode were used alone. This design of a small Littrow cavity with an AR coated diode is what enables the extreme tunability of the DL pro series. A DL pro tuned for 780 nm was previously used for testing on argon but could only tune to 815 nm single mode.

Before the 819 nm DL pro was integrated into the experiment, a home-built Littman-Metcalf ECDL was used with an 820 nm, 100 mW diode from Thorlabs. This laser is shown in Fig. 18. While this laser was suitable, it was not mechanically stable enough to use as a locking reference for the high finesse cavity (F$\approx$2500). However, it was suitable for testing with the low finesse cavity (F$\approx$450) in the prototype phase and the first preliminary experiments. The only spectrum analyzer available to measure the linewidth of the home-built laser had a limiting resolution of approximately 1.7 MHz, which is what was observed. So, the linewidth could be reliably stated as at or below 1.7 MHz.

The DL pro was controlled with a DLC pro, which was used for stabilizing the laser to an RF discharge of krypton using side-of-peak locking with two separate PID loops. One

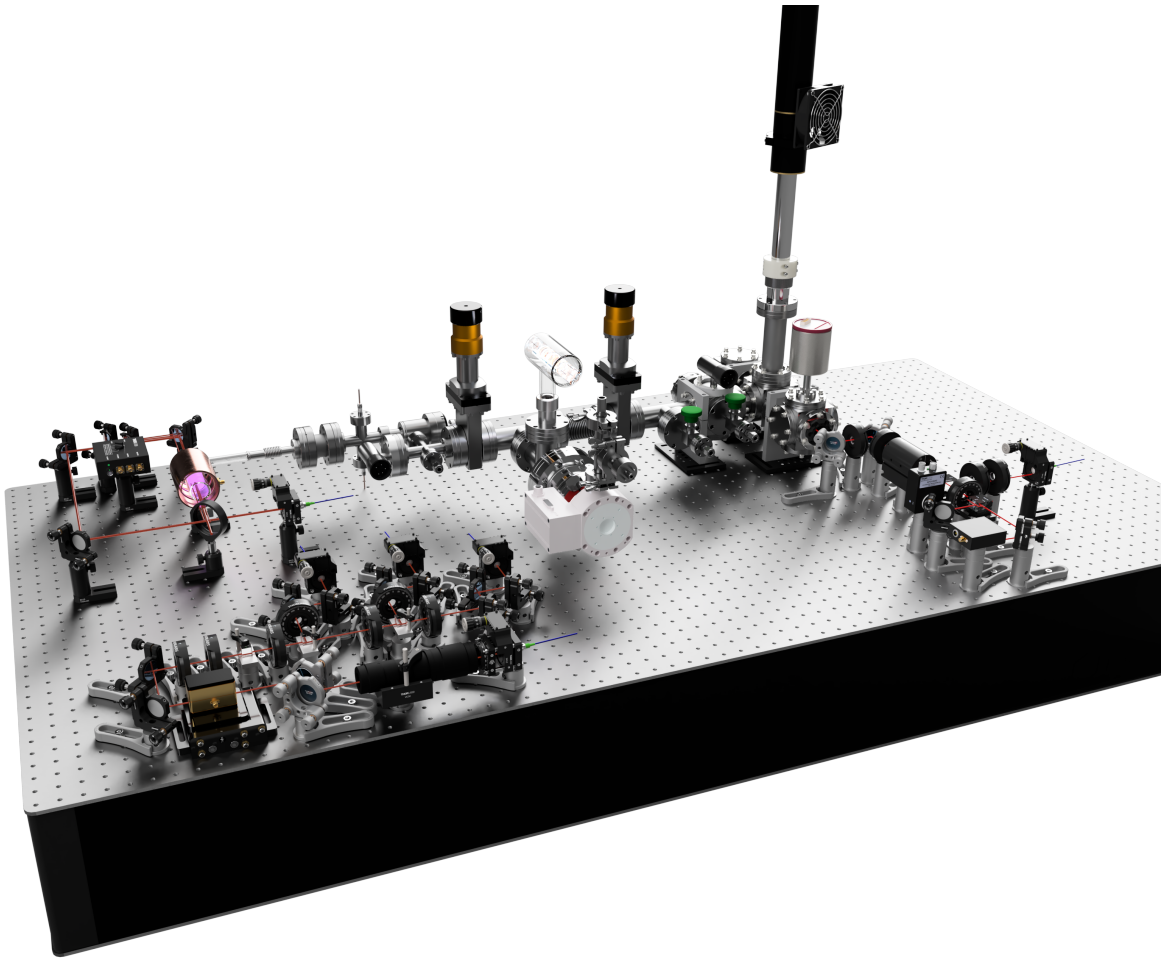

FIG. 17. This rendering shows the entire experimental setup with the glow discharge in the back left, power splitting and modulation in the front left, and the interaction/cavity region on the right.

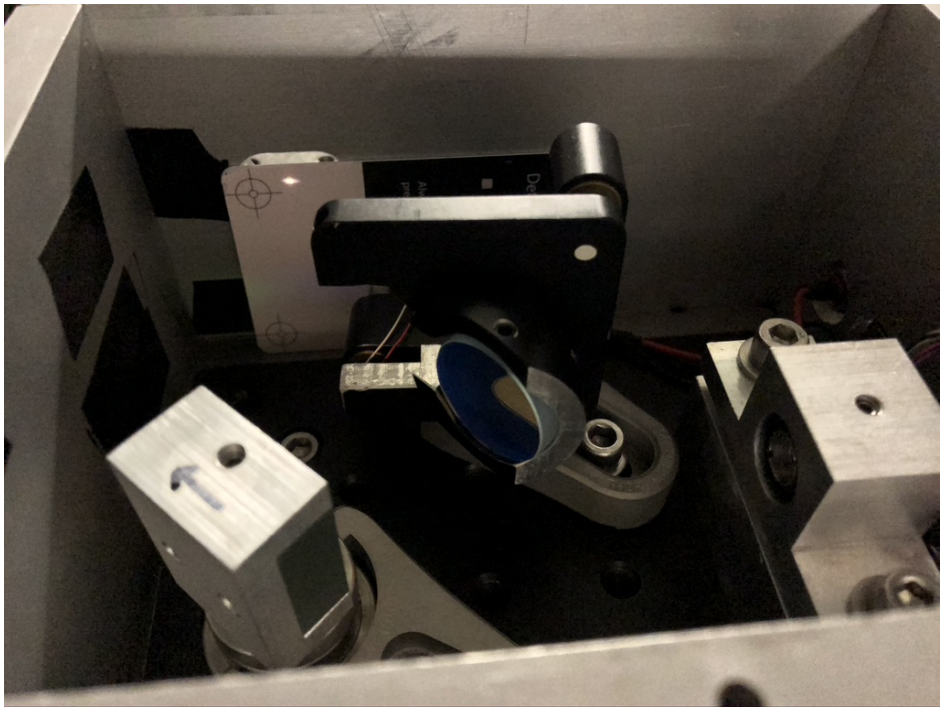

FIG. 18. This image shows the elliptical output of the 819 nm Littman-Metcalf built before the use of the Toptica DL Pro. The long cavity decreased its stability compared to the short DL Pro Littrow cavity.

loop fed back to the grating piezo for lower frequency disturbances while the other PID loop fed back to the diode injection current that corrected frequencies up to the cutoff frequency of the DLC pro (30 kHz).

The DL pro could not be modulated with an AC signal efficiently above 25 MHz using the injection current and on the order of 10 kHz using the piezo. An AC signal was desired to avoid burning the diode with a DC bias that can build up without careful treatment. Modulating the current or piezo at lower frequencies for the frequency lock created residual amplitude modulation in the cavity lock signal that decreased cavity stability. This fact was the primary determining factor for using FMS for frequency stabilization and PDH for cavity locking. This enabled the use of a single modulation frequency well above 20 MHz using an electro-optic modulator (EOM). Using a single high-frequency modulation reduces both technical noise and phase noise due to reduced 1/frequency noise and better isolation during phase-sensitive detection. For more on these techniques, see Chapter 5.

The output power of the Toptica after the fiber launcher was 48 mW, which then went through a telescope to pass the beam through the EOM with maximum efficiency and minimal loss, including both aperture loss and polarization loss. The fiber launcher before the telescope had a half-wave plate mounted to it to align the beam's polarization to the fast axis of the EOM. The EOM was mounted on a 5-axis stage that allowed fine-tuning of the EOM aperture, as well as angle of incidence/parallelism. A quarter-wave plate was excluded because power measurements showed little ellipticity in the beam introduced by the fiber. However, birefringence proved to be a problem throughout the rest of the experiment, where quarter-wave plates were used to counteract fiber and cavity birefringence.

Figure 19 shows a layout of the optics that received the fiber from the DL pro and distributed the power to each section of the experiment using polarization optics. The majority of the power (16 mW after fiber) was sent to the experimental cavity while 5 mW (after fiber) was shared between the reference cell and diagnostic fiber ports, which were used during construction and troubleshooting. Coupling into each fiber was between 55-70% due to imperfect matching between fiber mode sizes, coupling lenses, and beam shape. The primary reasons for sub-optimal coupling of the Toptica FiberDock$^{\text{TM}}$ were due to the beam size and ellipticity of the diode laser.

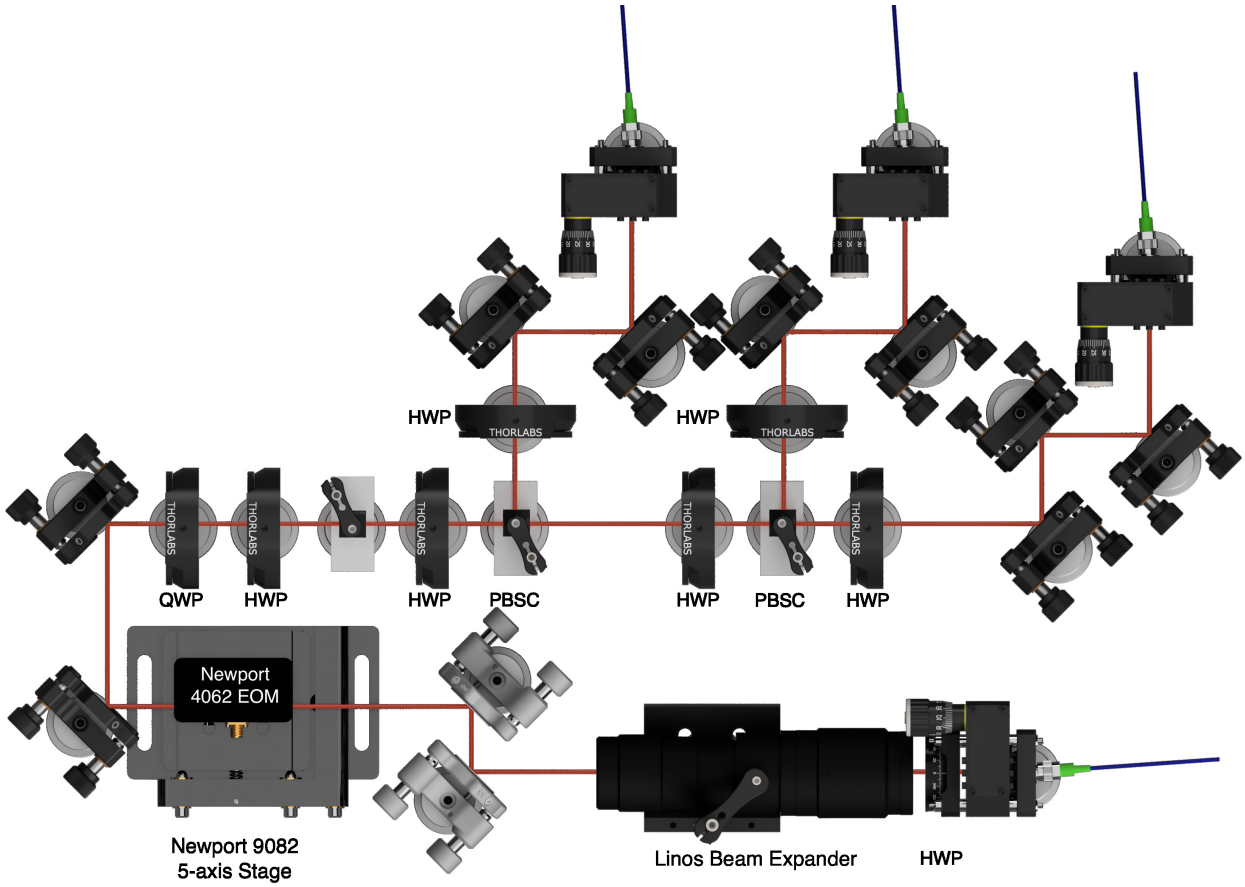

FIG. 19. Optics to split laser power between sections of the experiment. HWP is half waveplate, QWP is quarter waveplate, and PBSC is polarizing beamsplitter cube.

6.2 LASER STABILIZATION REFERENCE CELL

The DL Pro laser was frequency stabilized using a refillable cell inside an inductively coupled RF discharge. The frequency selected for the RF excitation was between 650-750 MHz, depending on the pressure-dependent impedance of the cell. Due to the lack of amateur radio bands in this range of frequencies, no commercially available antenna tuner was available. While possible to make a homemade tank circuit, frequency was tuned over this range to minimize the reflected power whenever the cell pressure was changed. This was found to be sufficient in minimizing reflections due to a strong frequency dependence of the impedance of the plasma. However, this frequency dependence was not as strong before igniting the plasma, which required the use of higher RF power and a piezo igniter to start. After ignited, the power would be turned down 75% to obtain the desired optical path length of plasma.

The FMS setup for frequency stabilization was that of a typical Doppler-free saturated absorption spectroscopy setup with two weak probe beams and a pump. The second probe beam samples the background krypton just beside the other probe with the overlapped pump. This optical setup can be seen in Fig. 20.

6.2.1 WAVELENGTH MODULATION SPECTROSCOPY HETERODYNE ELECTRONICS

While the intention was to do FMS, the experimental linewidth of the Doppler-free ^{84}Kr spectral line was about twice that of the modulation frequency. This firmly put the modulation in the WMS regime, despite the RF modulation. The modulation was imposed on the laser using a Newport 4062 broadband electro-optic phase modulator. The reference frequency was provided by a ZOS-50 voltage-controlled oscillator, which was used as the local oscillator for both the PDH lock-in amplifier and the WMS lock-in amplifier. While the lock-in for the PDH was built in-house from Mini-Circuits parts, discussed in 6.3.2, a Stanford Research Systems SR844 was used as the lock-in amplifier for the laser lock. The output of the SR844 was sent to the feedback servo, which was the low-frequency DLC pro Lock (<30 kHz). This enabled easy locking to either the current or piezo of the Toptica DL pro via their graphical user interface, displayed in Fig. 21.

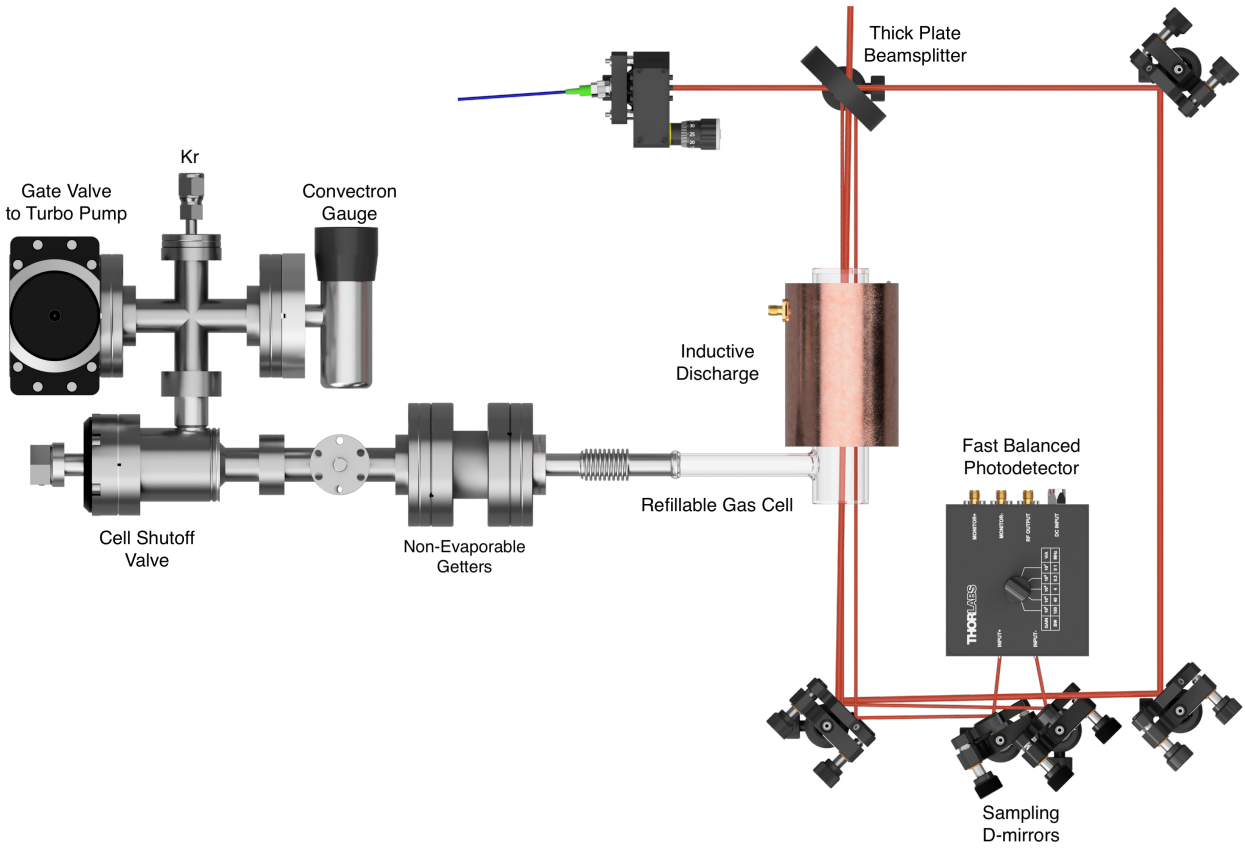

FIG. 20. Refillable RF Discharge cell for laser frequency stabilization.

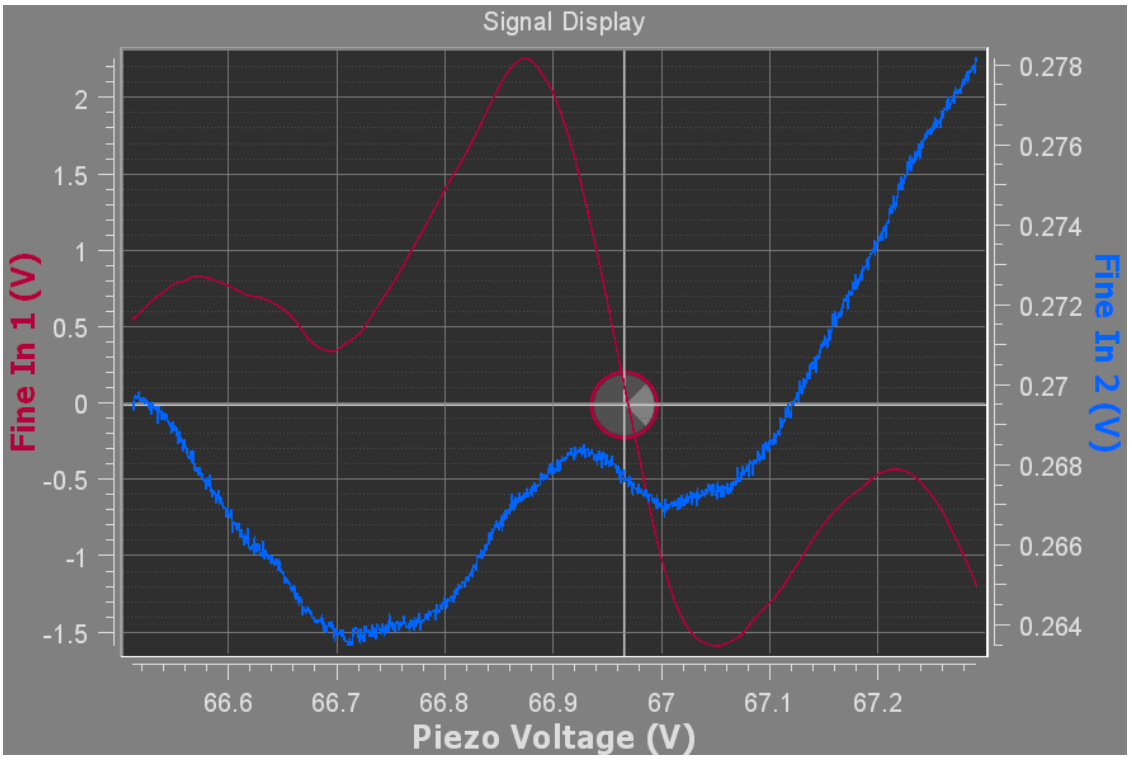

FIG. 21. Shown are a lamb dip from saturated absorption spectroscopy (Blue) and WMS lock-in signal (Red) for frequency locking the laser using the Toptica DLC pro software.

6.3 METASTABLE PRODUCTION CELL

The production cell required several features that needed to be incorporated into as small of a vacuum cell as possible. The smaller cell enabled better stability of the cavity and to have a more controlled volume of krypton. Using modular cubes allowed for easy testing of the best configuration and, with the use of supports, a stable foundation for the cavity to be rigidly coupled to the optical table through the vacuum. The cubes also allowed for flexibility on where to mount necessary components and easy expandability over a custom-made vacuum cavity.

The cavity lock required feedthroughs for the piezos, and optical access was required for the input and output of the cavity along with the fluorescence detection optics. Laser windows were used that had an AR coating specifically to give less than 0.25% reflectivity per surface from 650-850 nm. This AR coating helps prevent reflections from distorting the PDH signal as well as lowering the buildup due to reflections possibly causing partial deconstructive interference with the TEM_{00} mode of the cavity.

A Baratron® capacitance manometer was used as the primary instrument for pressure readings due to its insensitivity to gas type. A Convectron® convection-enhanced Pirani gauge was placed in the system during testing to help verify pressure readings and as a backup pressure gauge. However, it was removed for experimental runs due to concerns over unnecessary components causing contamination in a low-pressure cell with no pumping. To help with cleaning, a non-evaporable getter was placed in the cell. However, it proved to be ineffective at pumping the main contaminant/leaking gas, which turned out to be helium making its way through the gas handling valves at a rate between 0.1-0.5 mTorr per hour. This was likely due to repeated opening and closing of the shutoff valve in order to leak in helium with a variable leak valve (not shown in Fig. 22) located upstream of the shutoff valve (green valves in Fig. 22).

There was a significant amount of birefringence from before the fiber launcher as well as from the cavity. The birefringence from before the launcher was slower and seemed to be thermal, but the source was never isolated. However, monitoring the power transmitted through the first polarizing beamsplitter cube (PBSC) allowed constant monitoring of the polarization, as well as monitoring the transmission of the cavity. The birefringence from the cavity mirrors was primarily from stress inside the mirror coating [70, 71]. Due to the large gain of the high finesse cavity, the power incident on the cavity needed to be stable in order to have consistent Kr* production while experimenting with other parameters. This is why an additional half waveplate (HWP) and quarter waveplate (QWP) were introduced before

the cavity. The cavity birefringence could then be corrected separately from long-term drift corrections in the cavity input power.

The HWP and QWP before the cavity have another purpose in the PDH setup. The waveplates combined with the Faraday rotator (a tunable optical isolator with polarizers removed) allow nearly all of the reflected power to pass through the first PBSC, minimizing the risk of reflections from uncoated optics in other parts of the setup as well as reduce the risk for optical feedback. Although optical feedback was not of much concern in this experiment due to ample use of optical isolators and polarization-maintaining fibers, it is good practice to eliminate the risk for situations that may not have as much feedback isolation. It is common practice not to use a Faraday rotator and simply use a QWP and/or HWP to vary the amount of power going to the PDH detector. This leads to a significant portion of light returning to the source, in this experiment the fiber launcher. This method also has the downside of not having all of the reflected power available for detection in the event of low reflected powers. Also, this method presents a lack of polarization control in the cavity separately from controlling the power reaching the PDH detector. The former is especially important when doing cavity enhanced spectroscopy of atoms in external electric or magnetic fields. A QWP was previously used before incorporating a Faraday rotator, which resulted in the light inside of the cavity being circularly polarized. This caused significant power fluctuations due to the mirror birefringence changing with vacuum pressure. This effect was largest in a previous setup when one of the mirrors acted as one of the vacuum windows.

The final PBSC was used to split the reflected power between a slow photodiode, and the fast PDH detector. The slow photodiode enabled observation of the cavity reflection and optimization of the power incident on the PDH detector. The PDH signal was very sensitive to saturation and alignment. There seemed to be interference issues inside the fast photodiode based on the angle of incidence and power of the incident signal. The PDH signal varied in amplitude, but more interestingly in shape, depending on how the incident power was aligned to the photodiode, even when the signal amplitude stayed the same. This required optimization from time to time as frequency drifts and the phase matching required tuning. While the feedback was not very sensitive to the shape of the PDH signal, it was very sensitive to the DC offset of the PDH signal. It was found that the PDH signal's DC offset was lowest and more consistent when the PDH signal was closest to the theoretical shape and only required periodic adjustments due to temperature fluctuations over longer time periods (weekly vs daily).

The final design consideration was for light scattering from atomic scattering and mechanical scattering. The VUV lamp was a Resonance Ltd. KrLM-LQD12 VUV electrodeless lamp. This lamp was an RF discharge that was optically coupled to the vacuum cell via a MgF_2 window. That meant the lamp emitted light from every available transition with the amplitude depending on the branching ratio and discharge power. This meant 819 nm light from the lamp resonantly scattered off the Kr in the cell, and that the lamp was emitting 760 nm light that mechanically and resonantly scattered in the cell back to the fluorescence detection PMT. The resonantly scattered 819 nm light adds the possibility of increased Kr* production, but the intensity proved to be too low to contribute. However, that light also increased the PMT background that led to the use of double-stacked 760 nm narrowband filters. While the filters were designed for 60% transmission at 760 nm at a 10 nm bandwidth, both had a measured transmission of 54% at 760.2 nm with a central wavelength of 757.8 nm. It was determined that with a high enough PMT gain, the loss in transmission enabled a higher SNR due to the extra suppression of all other light. To see the filter transmission, see Appendix C.1.

6.3.1 OPTICAL CAVITY CONSTRUCTION

The original design of the cavity was to have the vacuum system between the cavity mirrors with laser access through windows. The long-term stability of this design was insufficient for the large power build-up of a high finesse cavity. The losses at the two vacuum windows would decrease the build-up significantly, even if AR coated windows were used. AR coatings have reflectivities around 0.05-0.25%, which are losses significantly higher than the losses of high reflectivity cavity mirrors. There are also absorption losses in the bulk of the windows that would further contribute to cavity losses.

The second change in cavity design placed one of the mirrors inside the vacuum with the other mirror being a window on the chamber. While this design minimized the optical losses between the mirrors, this design also showed to not be stable enough for a high finesse cavity. Additionally, the mechanical stress of the mirror deforming as pressure changed caused a changing birefringence, which changed the cavity performance day-to-day. Having one of the mirrors exposed to atmospheric air also suffered from thermal drifts from the lab's temperature swings, just as the previous design did.

For the final cavity design, the decision was made to have both cavity mirrors inside the vacuum, as is found in most modern reference cavities. In order to lock the cavity, piezos were required to align and scan at least one of the mirrors, which required a custom-designed

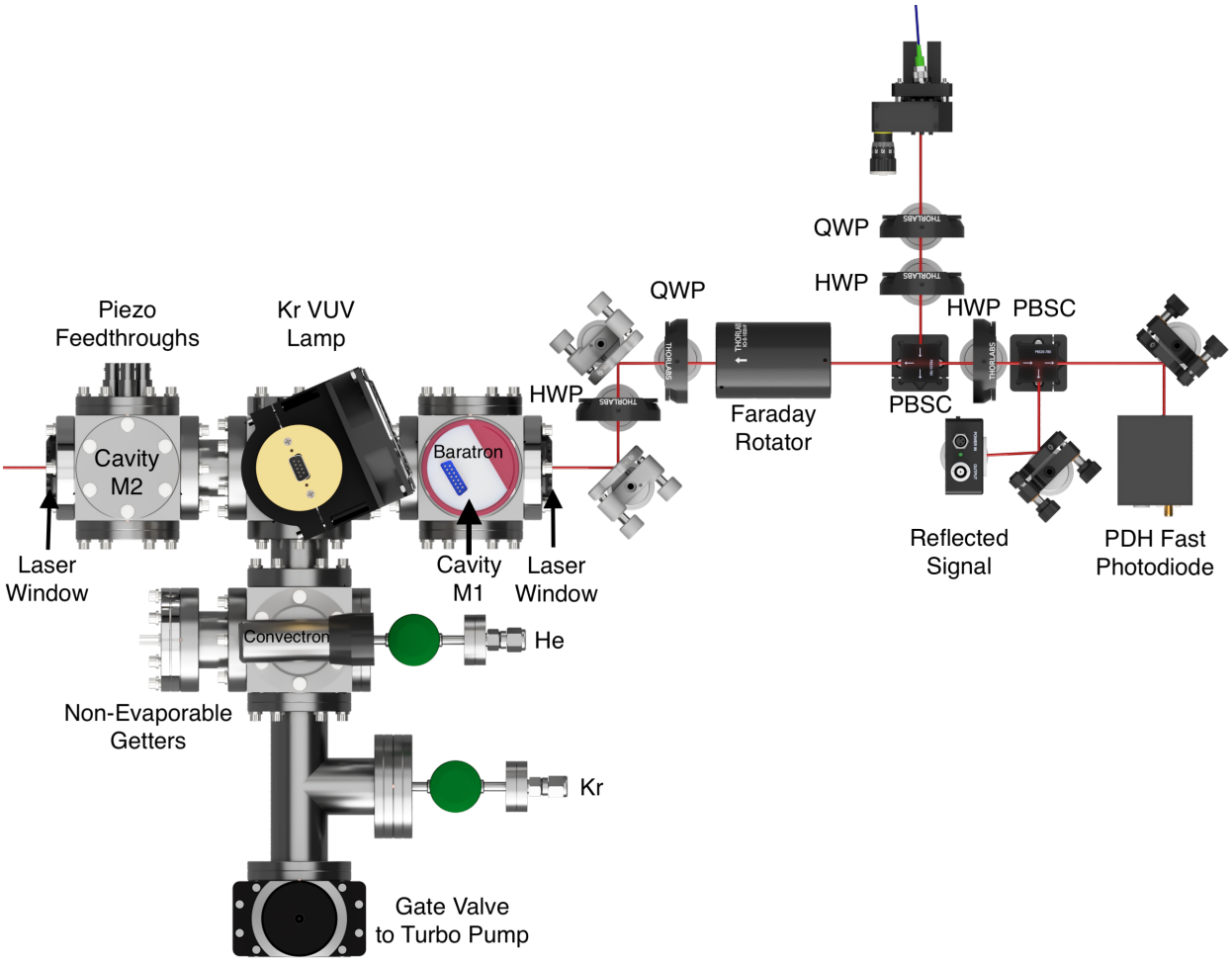

FIG. 22. Optics for aligning and mode-matching into the build-up cavity and the Pound-Drever-Hall Opto-electronics.

mount. There were two mirror mount designs, discussed in the following subsections. Figure 25 shows a rendered model of the final cavity configuration with the VUV lamp being loosely focused or collimated onto the laser beam halfway between the cavity mirrors.

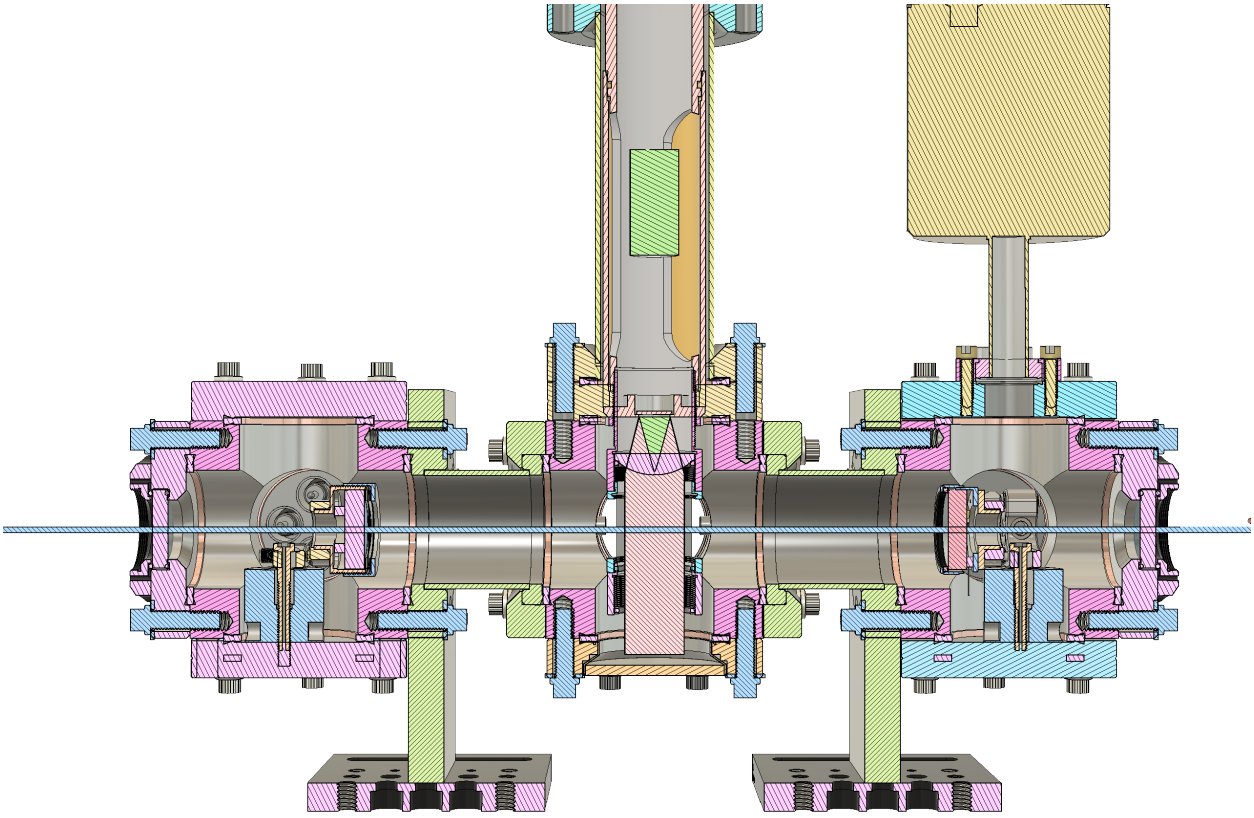

FIG. 23. This cross-section view shows the optical cavity and VUV lamp crossing at the interaction region.

Cavity Optical Design

The cavity type used was a semi-hemispheric design (see Chapter 4) with the waist on the planar mirror. Mirror 2 was selected to have the highest reflectivity to operate the cavity in the overcoupled regime, yielding the highest intracavity build-up. The highest reflectivity mirror ended up being planar, so the highest reflectivity curved mirror was selected as

mirror 1. Being of semi-hemispheric design, the cavity was far easier to align than a plane-parallel cavity. For the spherical mirror, a radius of curvature of 1 m was selected. Using a relatively long focal length mirror made it so the cavity behaved similarly to a plane-parallel cavity across the diameter of the beam. However, it also made it so high-order modes could be used as an easy alignment tool and be heavily suppressed within the frequency range of the modulation. This resulted in a PDH signal free of high-order mode disturbances. Incidentally, the waist size of the fiber launcher ended up being nearly the exact size of the cavity waist, enabling efficient coupling into the cavity with a coupling efficiency into the TEM_{00} mode between 98-99.5%. This further reduced the effects of high-order modes disturbing the PDH signal. The beam profiles showing the beam quality of the incident beam and the transmitted beam can be seen in Fig. 24.

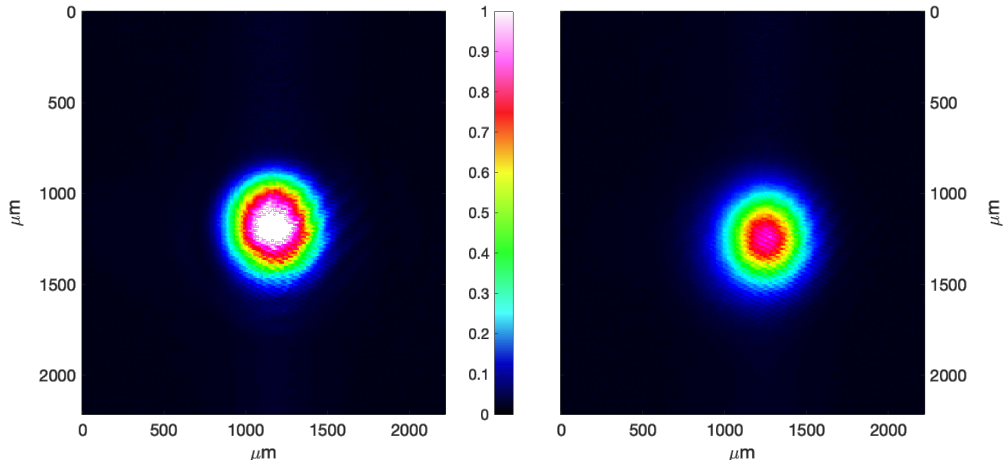

FIG. 24. The beam coupled into the cavity, on the left, can be seen to be very Gaussian. Optical cavities act as not only spectral filters, but spatial filters as well. The Gaussian beam transmitted can be seen to be very clean and similar to the incident bean, showing high coupling efficiency into the TEM_{00} mode.

A 1-inch mirror was selected because it was the largest diameter that could fit inside the ConFlat® cubes, even though 1/2-inch mounts were the only mounts to fit inside the cubes. The larger mirror diameter ensured better coating and surface quality across the beam diameter due to the fact that optical aberrations and defects are optimized for the central region of an optic. The larger diameter also allowed more freedom to design the

scanning mount using off-the-shelf parts readily available by giving more surface area to mount the piezo without blocking the central aperture.

The final version of the mirror mount was used for the scanning mount (mirror 2). The original mirror mount design was used, with the piezos and gasket removed, as a 1/2 - 1 inch adapter to mount mirror 1 in the vacuum using a second 1/2-inch kinematic mount. The final cavity configuration is shown in Fig. 25 with the final version of the mirror mount on the left and the original design on the right. However, the figure shows the piezos still in the model of the original design, while in the experiment the piezos were removed. This made it so only the new mount was adjustable while in vacuum and mirror 1 was as stable as possible. Figure 26 shows the Kr* cell from a different angle and includes the electronics and optics that direct and detect the modulated reflected signal for the PDH error signal.

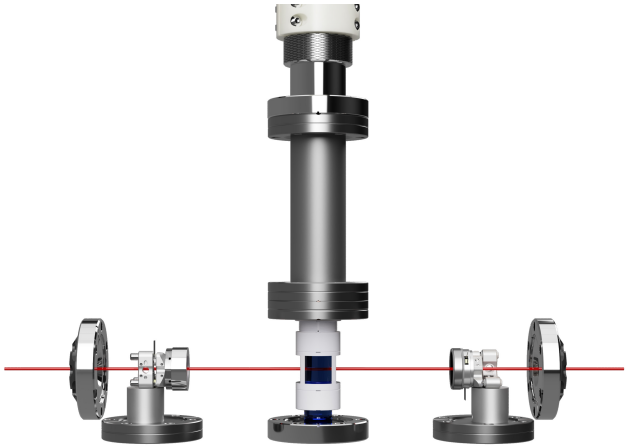

FIG. 25. Model showing the two cavity mirrors and the lamp being loosely focused into the interaction region using a MgF_2 lens. Optical access to vacuum is achieved using two laser windows with AR coatings optimized for NIR, shown in the flanges on either side of the cavity mirrors.

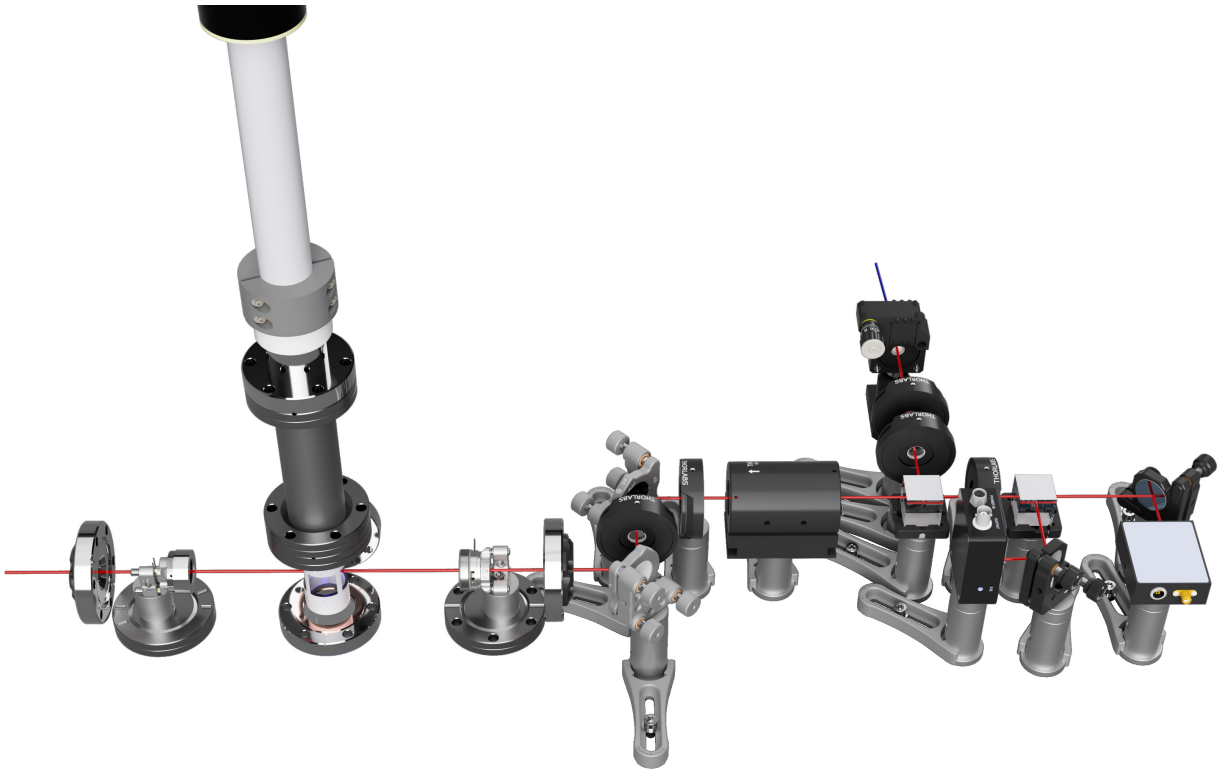

FIG. 26. Model showing the two cavity mirrors and the lamp being loosely focused into the interaction region using a MgF_2 lens. This view shows the PDH electronics and optics to detect the modulated reflection signal and to produce the error signal.

First Cavity Mirror Mount Design

The base of the previous design was based on the MH25T anodized aluminum mirror holder from Thorlabs, which was modified to connect to a custom adapter that fit into the 1/2" Polaris® kinematic mount. The three piezos could be scanned simultaneously using a scan balancer to scan the cavity length. The piezos could also be adjusted individually for minor alignment adjustments. However, due to the design, the motion of each piezo strongly coupled degrees of freedom, which complicated alignment.

To avoid permanently bonding the mirror to the piezo, the design specifically allowed the assembly to be non-destructively disassembled to swap parts. A Viton® gasket was used to provide resistance against the mirror and keep the mirror in place. The gasket proved to have a large amount of hysteresis. This design worked; however, scanning was not very linear over a free spectral range and lock performance was hindered by the hysteresis and scan imbalance between the piezos.

This design was also not optimally vacuum-compatible due to the anodized mirror holder. Anodization creates a porous surface that more efficiently traps contaminants. This anodization was partially removed by baking at a high temperature for several hours. However, since anodization is partially a coating and partially in the substrate of the material, only the outer layer could be baked off. The contact surface between the custom adapter and the mirror holder also provided a place for contaminants to get trapped and behave as a possible virtual leak. In addition to the possible outgassing/virtual leaks, the soft metal and fine threads of the holder, with the additional modifications, caused aluminum dust to be worn off every time the mount was disassembled. This design can be seen as a rendering from the back in Fig. 27 and as a cross-section in Fig. 28.

FIG. 27. The figure shows the first cavity mirror mount design rendering. The Polaris® mount can be seen with the kinematic adjusters without piezos. The MH25T has machined slots to accommodate the piezo wires. The stainless-steel adapter from the MH25T to the Polaris can be seen with the drawtube in the Polaris and one of the countersunk tapped holes that screws the MH25T to the adapter.

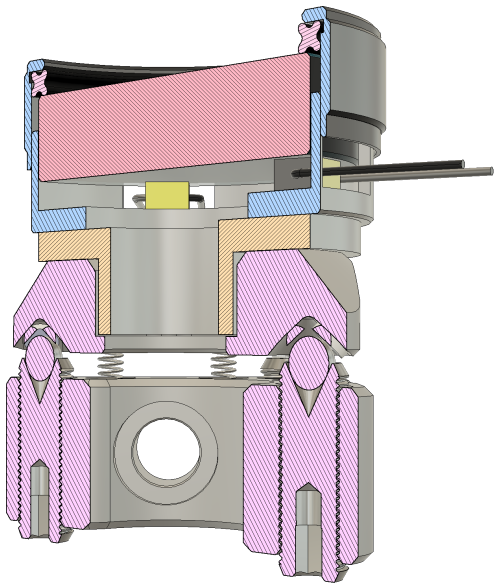

FIG. 28. Shown is the first cavity mirror mount design. The MH25T has the blue hatching, the custom adapter has the orange hatching, the Polaris® mount has the purple hatching, and the 3 piezos are equidistant from each other between the MH25T and the mirror.

Final Cavity Mirror Mount Design

The final design of the cavity mount improved upon the previous design by using all stainless-steel for better vacuum compatibility and mechanical stability. This design also improved fine adjustment of the alignment by putting a piezo on each kinematic adjuster. This isolated the degrees of freedom better and improved scanning by replacing the Viton® gasket with a stacked wave spring. This spring provided a linear resistance, less hysteresis, and a larger contact surface between the mirror and the mount. This greater surface area provided lower stress concentrations that could deform the mirror. While the spring was a great improvement, the best design for linearity and lock bandwidth would be to epoxy the mirror to the piezo, which is typically the design for cavity mirrors in commercial designs. Epoxying the mirror to the piezo reduces the load on the piezo, giving the largest bandwidth of the piezo and ideally puts the resonance outside of the servo's bandwidth for feedback stability. While the load on the piezo can be adjusted to a certain degree by adjusting the force on the wave spring, the load was set to the load that gave the piezo the largest stroke for the longest scan. However, that moved the resonance frequency into the bandwidth of the locking circuit. This resulted in oscillations when the gain of the servo was set too high. It would have been more ideal to set the load so that the resonance frequency was outside the bandwidth of the servo. This design can be seen as a rendering from the back in Fig. 29 and as a cross-section in Fig. 30. More photos of the actual final products of these mirror designs can be found in Appendix B.

6.3.2 POUND-DREVER-HALL HETERODYNE ELECTRONICS

Due to the relatively high modulation frequency, only one commercial lock-in amplifier was available in the lab, which was used to frequency lock the laser to the RF discharge using WMS, discussed in 6.2.1. This necessitated the assembly of a lock-in amplifier made from Mini-Circuits parts, as shown in Fig. 31, for the PDH lock [63, 64]. The voltage-controlled oscillator was used as the local oscillator for both laser and cavity locks. The auxiliary output was sent to the Stanford Research Systems SR844 while the main output was sent to a power splitter. Half of the power was sent to the electro-optic phase modulator, after being attenuated and amplified with a Mini-Circuits TIA-1000-1R8. An amateur radio impedance-matching antenna tuner was used to minimize reflections from the modulator back to the amplifier. Impedance matching for this type of electro-optic modulator, known as broadband, is mostly for the safety of the amplifier and other components. Resonant

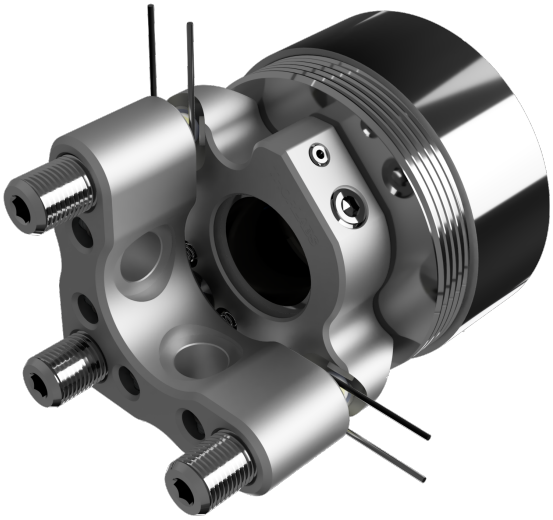

FIG. 29. The figure shows the final cavity mirror mount design rendering. The Polaris® mount can be seen with the kinematic adjusters with piezos between the adjuster and sapphire plates. The stainless-steel adapter is now combined with a custom mirror holder that holds the piezo, mirror, and wave spring for scanning.

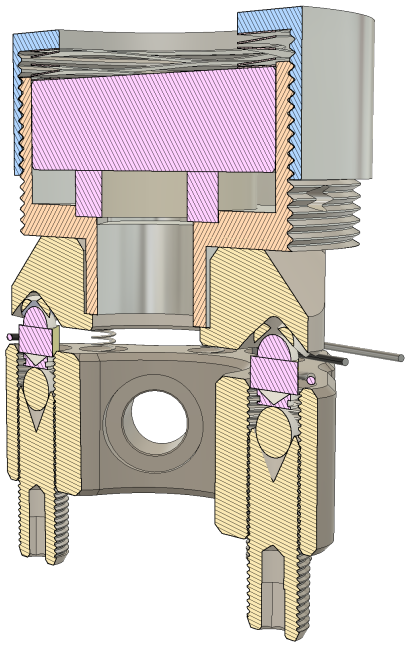

FIG. 30. Shown is the final cavity mirror mount design. The mirror and piezo have the pink hatching at the top, the custom adapter has the orange hatching, the Polaris mount has the yellow hatching, and the three piezos have pink hatching between the two bodies of the Polaris® mount.

electro-optic modulators require careful impedance matching in order to function properly, but often include tank circuits from the manufacturer to help alleviate design difficulties.

The other half of the power went through fixed attenuators to a Mini-Circuits JSPHS-51 phase shifter. Attenuation was needed because distortion is introduced in these phase-shifters beyond a rated power. The signal was then amplified and attenuated to the 7 dBm input power of the mixer's local oscillator input. The RF photodetector used for detecting the phase-modulated reflected cavity signal used a DC block to AC couple the signal before being amplified and mixed. The phase of the local oscillator was shifted to select the quadrature component of the mixed signal, and the output was then low-pass filtered. This low-pass filtered error signal was then sent to the feedback servo for locking. For a background on the theory of the PDH lock, refer to 5.4.3.

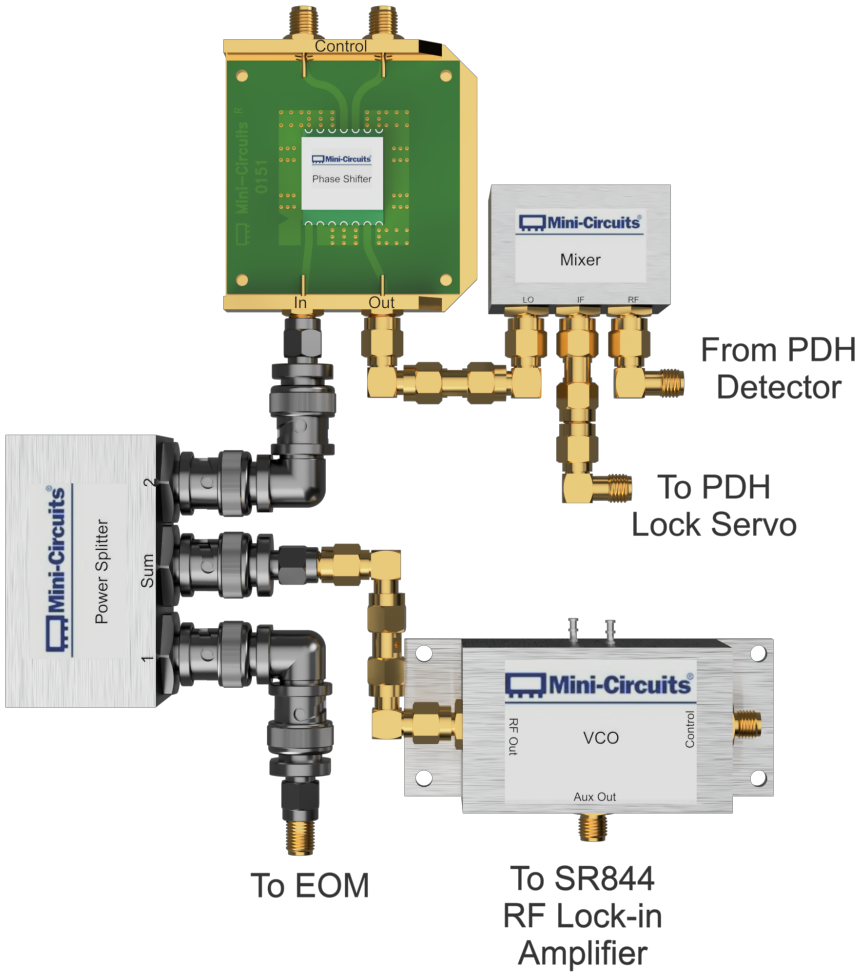

FIG. 31. Heterodyne detection electronics for locking the cavity length to the laser using the PDH method.

CHAPTER 7

EXPERIMENTAL RESULTS AND ANALYSIS

This chapter will discuss the experimental results for Kr* production as a function of 819 nm power, 123 nm power, Kr pressure, and He+Kr pressure. The dependencies on power and Kr data are key data for all-optical production of Kr*, while the He+Kr data are to explore the feasibility of an all-optical DPRGL. The data obtained were specifically of ^{84}Kr because it is the most abundant isotope and had the best signal to lock to for testing. The saturated absorption spectrum of the even isotopes of Kr, as well as the main even isotope shifts, can be seen in Fig. 12, with the fitted isotope shifts within 1% of those measured in [72].

The data were taken by measuring the PMT current with a picoammeter and averaging 1000 data-points with the 819 nm laser on, with the 819 nm laser off, and then taking the difference. The lamp remained powered on each day for stability. The difference was taken between the signal with the laser on and off because the lamp provided a steady 760 nm background due to the discharge populating the $2p_6$ state, which then has an indistinguishable fluorescence signal from the signal under investigation.

7.1 CAVITY BUILD-UP MEASUREMENTS

To determine actual cavity performance, the transmission and reflection coefficients of the entire cavity were measured and fit to a mathematical model that ran a minimization algorithm to determine the transmission, reflection, and losses of the cavity to match the experimental results. These results allowed the finesse, gain, and quality factor to be estimated several different ways, which all agreed to within 15% for overall finesse.

Finesse measurements were done by employing several different methods. The two primary methods were fitting the PDH signal to the model and measuring the ratio of the FSR to the cavity linewidth. The cavity linewidth was the more difficult measurement due to mechanical vibrations broadening the linewidth and making the lineshape deviate from a smooth curve due to random disturbances. With an adequately fast feedback system, these vibrations could be corrected. However, with a bandwidth of only about 5-10 kHz, they were not sufficiently damped.

The mirrors were measured outside of the vacuum using the same laser that was used in the experiment to get accurate transmission values. The transmission for the input coupler (ROC=1 m) was measured at T_1=0.00059 and the output coupler (ROC=∞) was measured at T_2=0.00022. Due to the lack of a cavity ringdown setup or the proper experimental apparatus to measure such high reflectivities and low losses, the only value directly measured for each mirror was the transmission. The transmission was measured using an optical power meter and an amplified, linear photodiode to check the measured values. The estimated values from CVI, for the spherical mirror, was T=0.00087 and R=1-T=0.99913. The planar mirror from RMI was only quoted above 0.998. However, the measured value and the fit value discussed below match quite well.

The numerical simulation used to match the experimental cavity transmission (T_{cav}=0.34) and reflection (R_{cav}=0.24) coefficients to the theory gave fitted values of T_1=0.00245, T_2=0.0004, L_1=0.0004, L_2=0.00004, R_1=0.9972, and R_2=0.9996. These values give a finesse of 1907, which is within 10% of the experimental value, discussed below, of the measured ratio of the FSR to the transmission linewidth. These parameters also produce an estimated optical gain of G=875 with respect to the input beam and an intracavity gain of $\frac{G}{T_1}$=$3.57 \cdot 10^5$. This results in an estimated Q-factor of $6.6 \cdot 10^8$. The experimental cavity transmission and reflection lineshapes can be seen in Fig. 32 compared to the theoretical fits.

Cavity Linewidth Measurements

The FSR was measured for each iteration of the cavity, and the length of the cavity was able to be determined for each. The final cavity design ended up with a cavity length of 142.2 mm at atmospheric pressure and 143.4 mm at vacuum. This change in length is a combination of the change in the index of refraction inside the cavity and the external pressure on the mirror mounts relaxing as the pressure decreases. This cavity length gives an FSR of 1.054 GHz. The FSR was calibrated using the sidebands that were produced by the EOM for the PDH and WMS locks, shown in Fig. 33. For the final experiments, the EOM modulation depth was decreased to keep 99% of the power in the carrier. The scan is slightly nonlinear, so the calibration was based on the average of the two calibration factors obtained from the sidebands of each longitudinal mode. The different amplitudes of the longitudinal modes in Fig. 33 is due to temporal fluctuations of the cavity transmission from mechanical vibrations. When scanning the laser frequency, rather than the cavity length, the mode amplitudes vary due to mechanical vibrations, different reflectivities at the

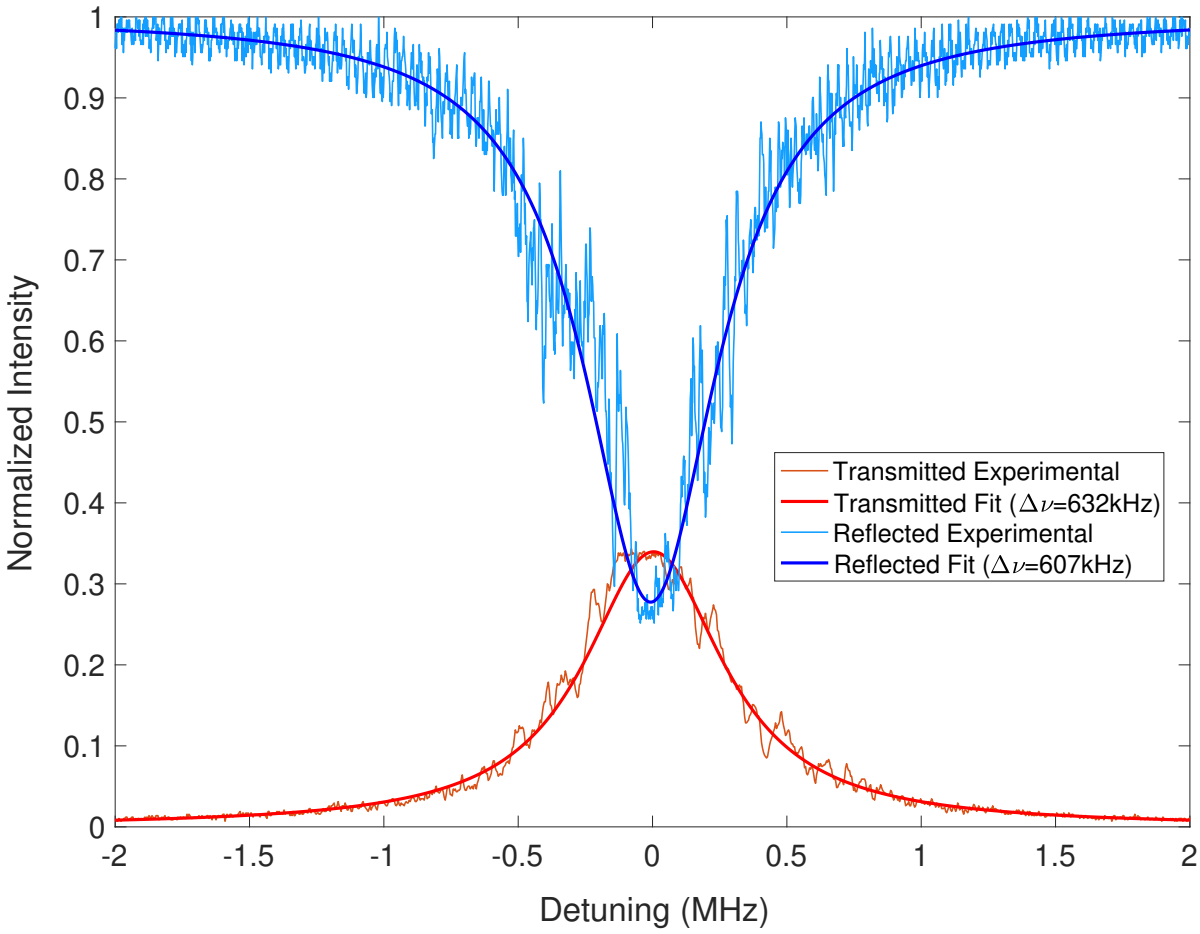

FIG. 32. Lorentzian linefunctions fit to experimental cavity transmission and reflection signals.

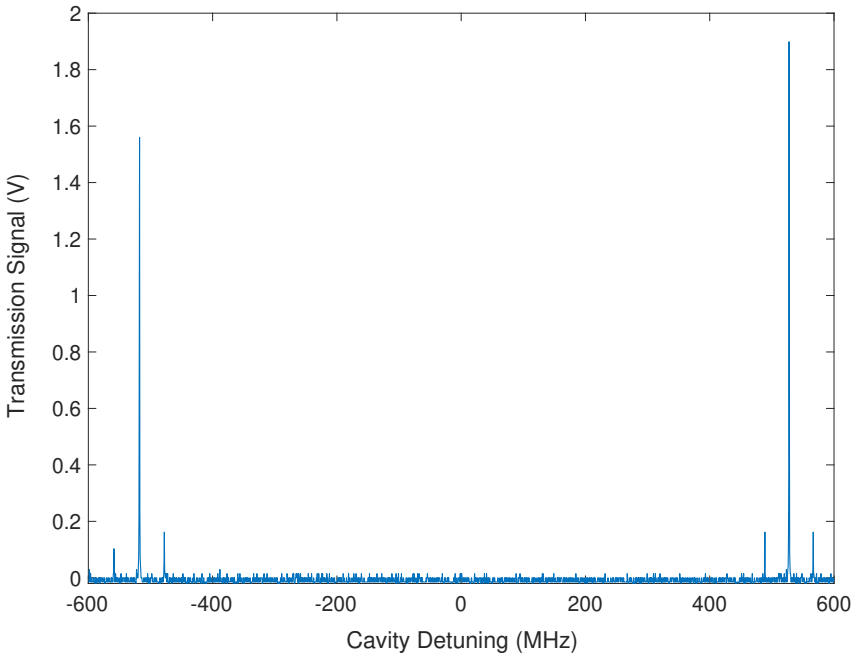

FIG. 33. The cavity free spectral range measurement was calibrated using the sidebands from the EOM. The EOM modulation was set to 39.75 MHz.

different frequencies, and different laser powers due to the frequency dependence of the laser feedback grating.

Figure 34 shows the linewidth fits based on selected slopes on the measured cavity transmission. The transmission signal shows the resonance having multiple peaks, seeming to stem from the mechanical vibrations causing the peak to jump back and forth. The narrowest fit is fit to the steepest, continuous slope. The widest fit is fit to the slowest, continuous slope, and the best fit includes the entire signal. With an FSR of 1.054 GHz, the best fit finesse would be 2165, about 13% higher than the finesse from the PDH and transmission/reflection measurement methods.

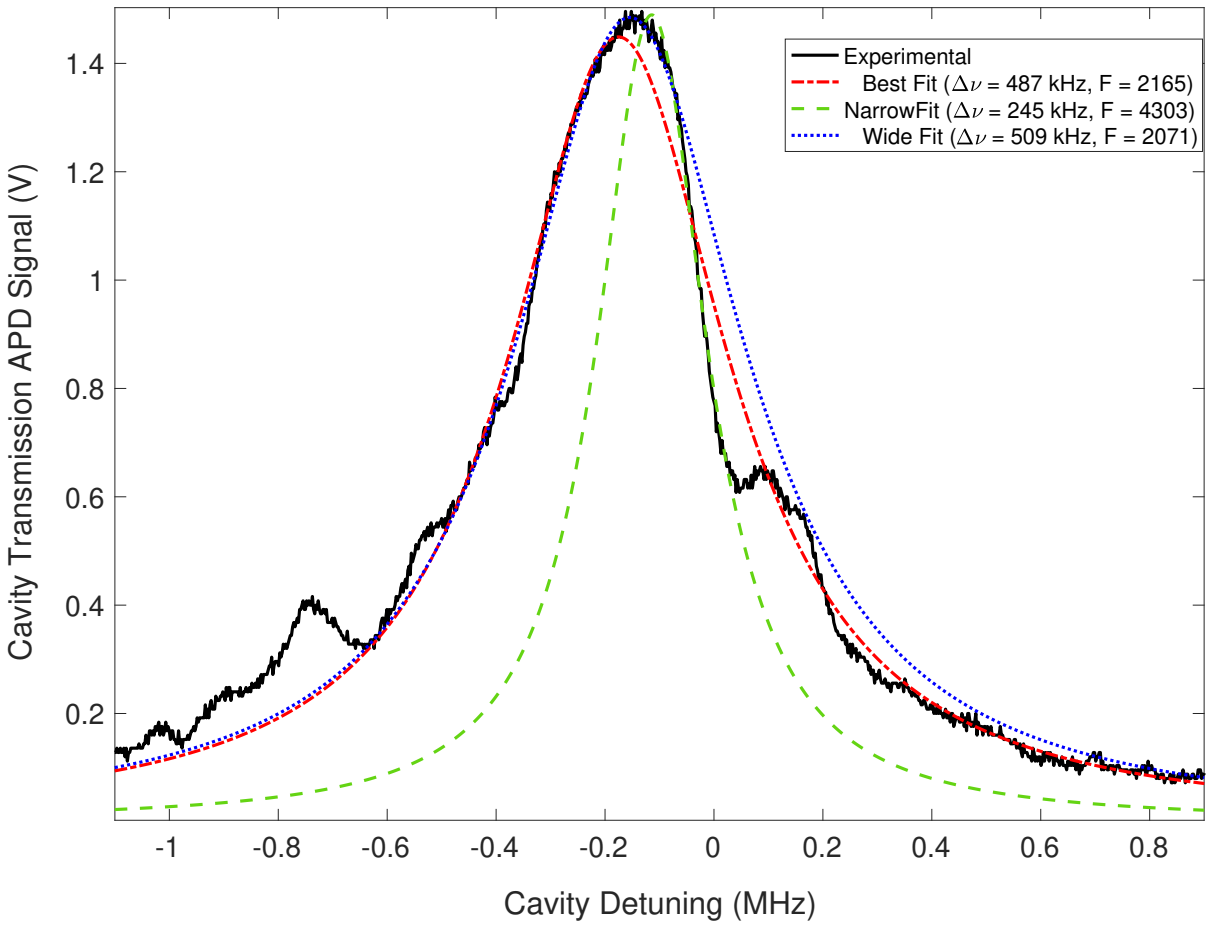

FIG. 34. Shown are three Lorentzian fits to the cavity transmission. The fits represent the best fit, narrowest fit, and widest fit based on distinct slopes on the curve. The Toptica DL Pro unlocked linewidth was stated as $\Delta\nu$ <200 kHz, and the scan was taken by scanning the cavity length at 100 Hz to limit the effect of low frequency vibrations.

PDH Measurements

The PDH signal is based on the reflected signal, which means that it is less affected by cavity losses than the transmitted signal. This also means that the PDH signal should give a much better SNR due to its limitation of intensity noise of the laser and cavity, which was a significant problem with doing measurements of the transmitted signal. Figure 35 shows the theoretical PDH fit agreeing very well with the experimental PDH error signal, with a fitted finesse of 1907. A finesse of 1907 corresponds to an average reflectivity of R=0.9984, which was the same value obtained from the measured cavity values of T=0.34 and R=0.24. The linefunctions fitted to the measured T and R curves give a linewidth of 550 kHz, while the fit curves in Fig. 34 give a linewidth of 607 kHz. This difference may arise from the data being taken on different days under different conditions and from the higher SNR of the PDH measurements, along with the measurement uncertainties where the T and R values were taken (peak value vs average value at line center).

The theoretical PDH equations used for fitting in Fig. 35 are Eq. (31) and Eq. (32) in 5.4.3, where F is the reflection coefficient at angular frequency ω, centered around the carrier resonance ω_o and the sideband resonances offset by the modulation frequency $\Omega = 2\pi f$. The value r put into the theoretic fit was the average coefficient of reflection of the cavity mirrors, or the square root of the average reflectance of the cavity mirrors.

However, one observation to note was that while servicing the mirror during the cavity overhaul, the input coupler was found to be visually foggy. This was likely due to photopolymerization on the coating due to the intense VUV light, which is known to be a major cause of transmission degradation in VUV experiments. While there were no measurements taken to test the decrease in the transmission at 819 nm, the mirror was cleaned and not checked again. The experimental transmission values suggest a slight degradation, but moreso suggests an increase in scattering losses, which is a reasonable assumption for a surface contaminant.

Another method, cavity ringdown, was used on the first cavity design, which gives a measure of the effective Q-factor of the cavity by measuring how long light takes to escape the cavity. This technique wasn't successful on the first cavity due to the use of an AOM with a switching time on the same order of magnitude as the cavity ringdown time constant. The new cavity would have been able to be measured more accurately through this method, but the ringdown time constant would have still been too close to the AOM switching time to be completely reliable when considering the effort of adding the AOM back into the experiment. The AOM was not kept in the system for the first experimental run due to the loss of power.

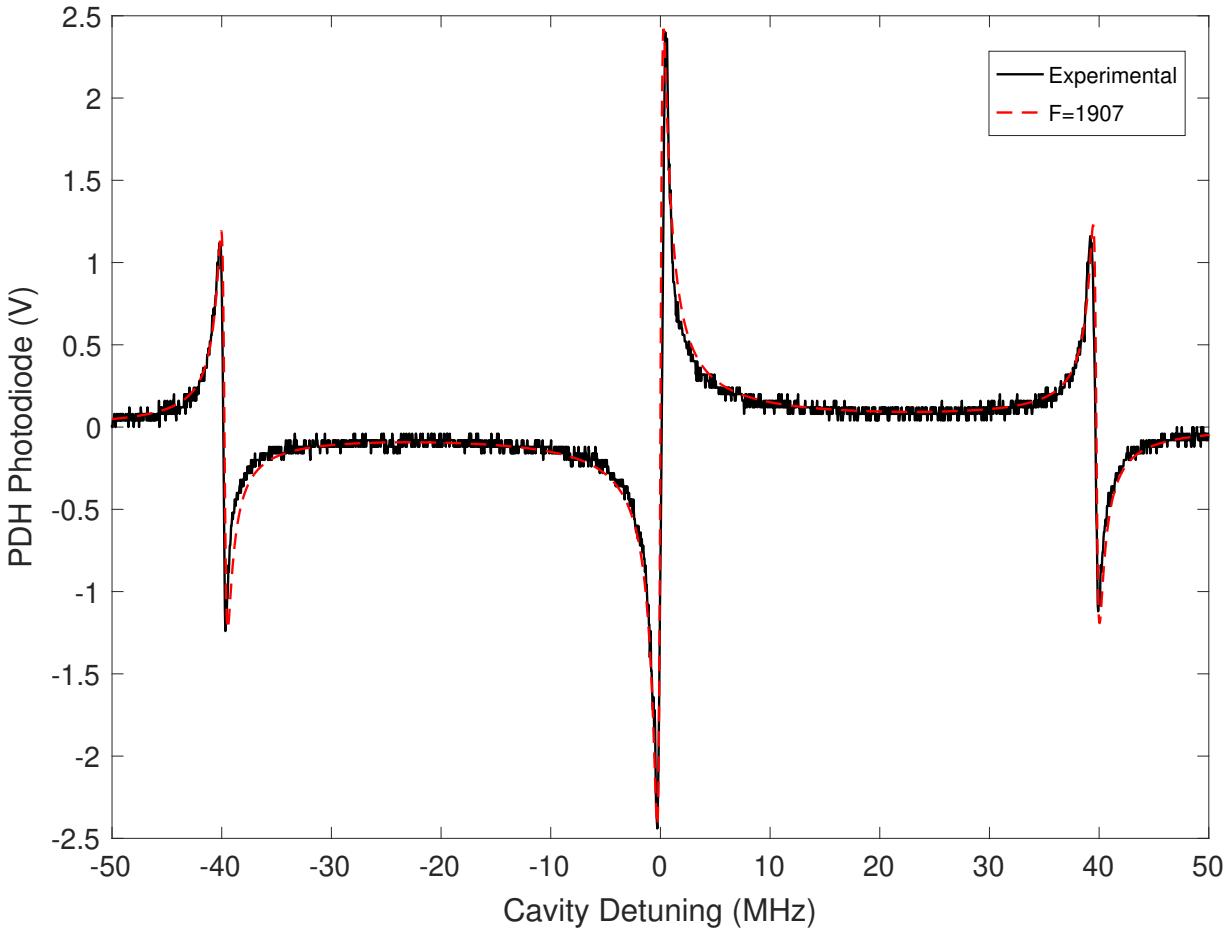

FIG. 35. Experimental PDH signal with theoretical fits to estimate the reflectivity finesse. The modulation frequency used was 39.97 MHz, with a measured cavity FSR of 1054 MHz and linewidth of around 500-600 kHz.

7.2 Kr* PRODUCTION DEPENDENCE ON Kr PRESSURE

This section focuses on the first main set of results in this dissertation. These first data are on the of Kr* production dependence on not just Kr pressure, but on 819 nm power and 123 nm power. The Kr* production was studied by adding Kr to the cell across the pressure range of the pressure transducer, which was from 1 mTorr to 10 Torr. First, the 819 nm power was varied to look at the production dependency on 819 nm power, and to observe any saturation behavior. These data, displayed in Fig. 36, were obtained with the first generation of the cavity, which had an estimated optical gain of only 56. A more calibrated measurement for Kr* production would be 811 nm scattering on the cycling transition due to the more well-defined parameters and higher scattering rates in scattering experiments.

As expected from numerical modeling, the 819 nm power shows some saturation, and the signal only changes in amplitude due to the low scattering cross-section that ground state Kr has at 819 nm. This small amount of scattering produces a mostly pressure-independent change in Kr* production with 819 nm power. In this configuration, the 819 nm power in the interaction region is only expected to be 500-600 mW, which gives a saturation parameter of 30 with a 400 μm cavity waist.

The second part of the Kr pressure dependence study was to vary the 123 nm intensity from the lamp, which is described in 6.3. The lamp had a manufacturer-measured intensity of the broad 123 nm light of $2{\cdot}10^{15}$ photons/s/sr, which gave an estimated power of 0.13 mW across a beam waist of about 10 mm. Due to lack of VUV measurement equipment, many of the VUV parameters are estimated from computer-aided design (CAD) models and numerical models.

Because the 123 nm light resonantly scatters with the ground state Kr, there was expected to be a pressure dependent change to the shape of the data, unlike what was seen for the 819 nm data. Because the VUV photons get absorbed and scattered in a physically complex manner, and because the VUV light was so broad that it excited a large number of velocity classes, the pressure dependence vs 123 nm power, in Fig. 37, was more difficult to study than the 819 nm data. The numerical model in the next chapter will discuss the experimental data with respect to the semi-classical model of the experiment to investigate the complicated structure of these data, which is believed to be a combination of self-reversal of the spectral line and radiation trapping [11, 73].

Using a PMT gain of 10^7, PMT quantum efficiency of 0.02, an optical transmission of 0.4, and a collection efficiency of 10%, these data show a peak ^{84}Kr* production rate of $1.2{\cdot}10^{10}$ atoms/s, which is very similar to the $7.2{\cdot}10^{10}$ atoms/s reported by Z.T. Lu's lab at

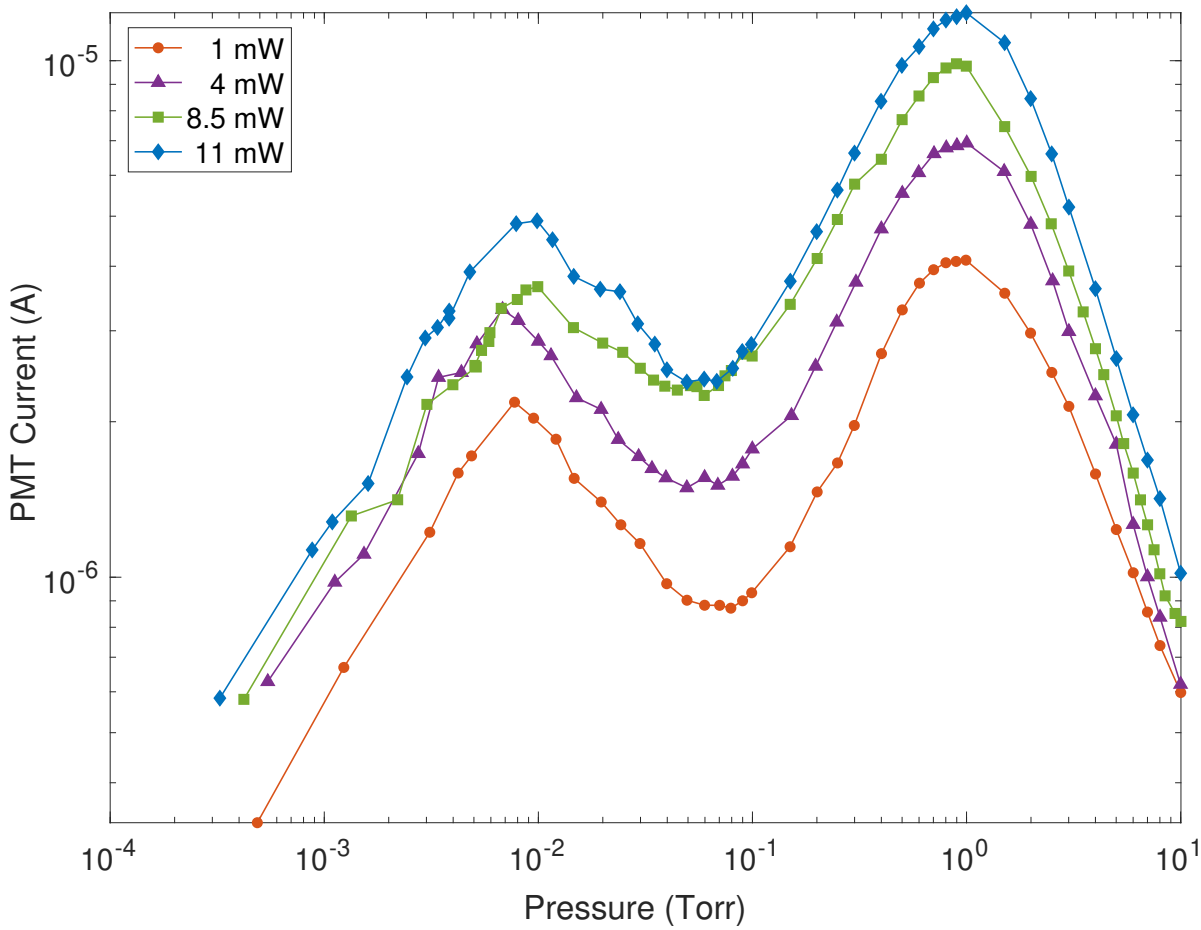

FIG. 36. Kr* production as a function of pressure at various 819 nm powers with an estimated cavity build-up of 56. The VUV lamp was at the default 80% power.

Hefei National Laboratory [11]. The 819 nm power in Z.T. Lu's work was delivered by a tapered amplifier and was slightly higher than in the data presented in this dissertation[12]. However, the reported photon intensity of the lamp used in [11] was an order of magnitude higher than the Resonance lamp used in this work. In 7.4, the higher finesse cavity was used to obtain 819 nm powers more than an order of magnitude higher to yield higher production rates.

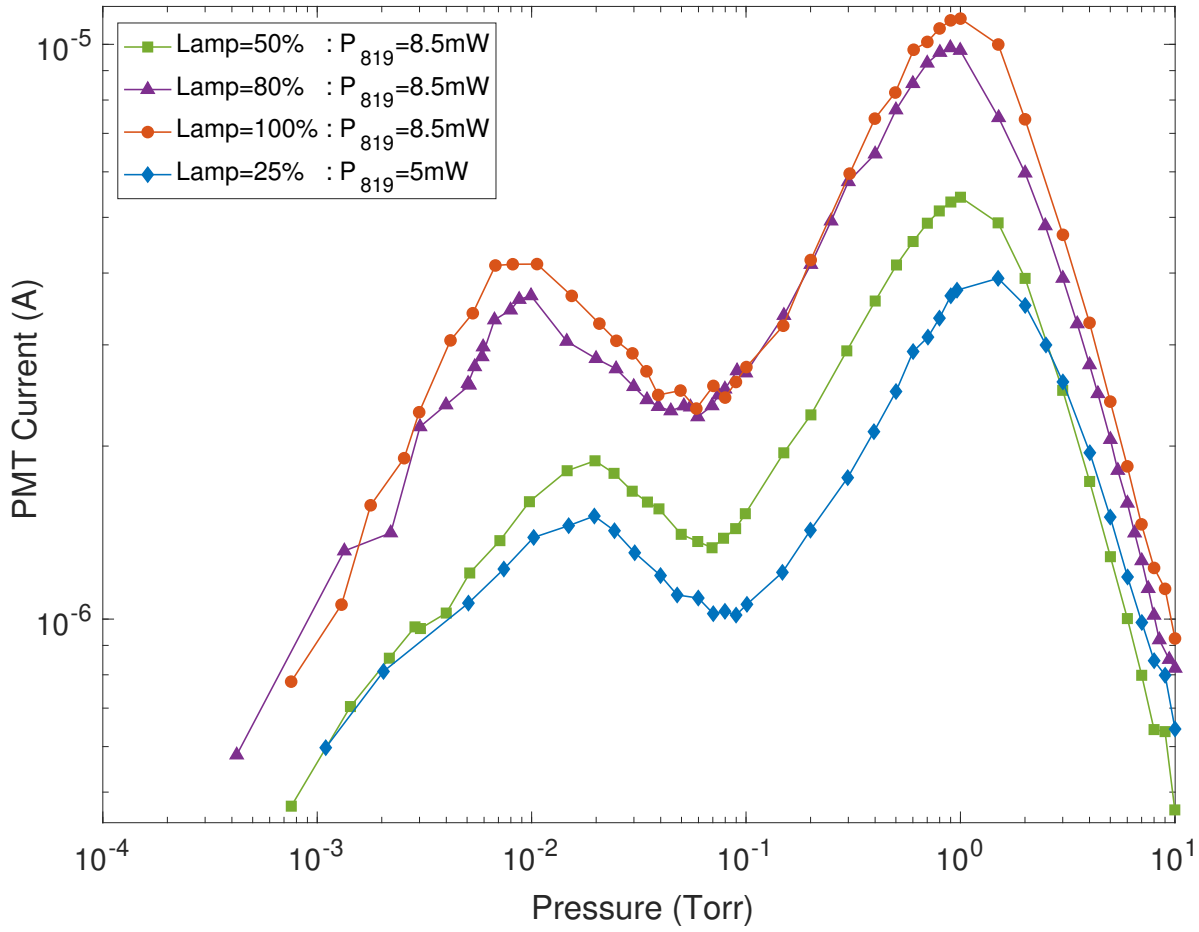

FIG. 37. Kr* production as a function of pressure at various 123 nm lamp RF powers. 123 nm power responds nonlinearly with RF power. Thus, RF lamp power percentage is given. Estimated cavity gain is 56.

7.3 FLUORESCENCE LINEWIDTH MEASUREMENTS

In this section, the 819 nm laser is scanned in frequency to look at the lineshape of the 760 nm fluorescence. These data were obtained to look into the physics behind the two-step excitation due to the extremely broad linewidth of the 123 nm light (strongly incoherent). The 819 nm laser scan was done at three krypton pressures. While this provided a test for the model in terms of collisional broadening, the test was not done with different 819 nm and 123 nm intensities, which would look at intensity broadening. However, the expected intensity broadened 819 nm linewidth for a saturation parameter of 450 was 120 MHz, while the Doppler width was 490 MHz. The saturation parameter of the 123 nm lamp was approximately 10^{-6} and could not be changed much. Therefore, the intensities were found to be mostly negligible for this test. Also, the pressure broadening/homogeneous broadening was a major consideration in this work, and therefore was a primary independent variable.

Resonance broadening, broadening due to the transition having a level that has a strong electric dipole transition to the ground state, was on the order of the intensity broadening at 1 Torr. Resonance and collisional broadening both depend on the pressure of the species. By using the mean free path and average thermal velocity, the collisional broadening was included, discussed below and shown in Figs. 38-40. For more on broadening mechanisms and linewidths, refer to Chapter 2.3.

The model fits the experimental lineshapes very well as the pressure is changed. As the pressure changed, the only corresponding linewidth that changed was the homogeneous (Lorentzian) linewidth, while the inhomogeneous (Gaussian) linewidth remained the same. The only model parameter that needs to be investigated more to fit the data is the Gaussian broadening, which had to be scaled by a 25% scaling factor in order to fit properly. The Gaussian part of the Voigt function was 627 MHz, while the calculated Doppler width of the 760 nm transition is 530 MHz, a 15% difference. The most likely phenomenological explanation involves the broad, incoherent behavior of the 123 nm light. It is either broader than expected due to parameters in the lamp that are experimentally unknown, or the model does not currently have enough physics to account for how the large number of velocity classes available to the 123 nm lamp plays a role in the linewidth and how that correspondingly affects the 819 nm transition even though a narrow laser is used.

One other possible contribution to the fluorescence being broader than expected could be heating of the Kr due to the intense NIR power in the cavity. This would increase the Doppler width and therefore increase the Gaussian part of the Voigt linewidth. However, due to prior work in atomic beams, this increase in temperature was estimated to be negligible,

especially with the low population of Kr that is resonant with the 819 nm laser and the large thermal mass of Kr available in a cell over an atomic beam. Additionally, in the model used to calculate the Voigt linewidths, in order for an increased temperature to account for the 25% scaling factor needed, the temperature would have to be 550 K rather than 300 K.

In a two-level transition, the unbroadened linewidth is the sum of the two natural linewidths of the transitions. Depending on the saturation parameters of the lower beam, the linewidth can be modified to be only the linewidth of the upper transition due to the saturation of the first transition. Since the lower transition in this experiment was far from saturated, this heavily contributed to the linewidth since the natural linewidth of the transition out of ground is an order of magnitude higher than the upper transition. This broadening would be Lorentzian, but the resulting intensity broadening from the saturation of the upper transition would be a Gaussian broadening term. These mechanisms, discussed in [31], are the subject of future work to modify the model to include more accurate information on the 123 nm transition. These data are shown in Figs. 38, 39, and 40.

In Fig. 41, the 819 nm frequency was scanned at 1 Torr of Kr with five different powers, with three of them graphed for clarity. The model used to fit the Voigt functions were the same as in Figs. 38-40, but with a higher cavity gain and different input powers. The model does not fit these data as well as the other three figures, which were taken with the old version of the cavity. The fact that the model is slightly narrower than the data suggest that there is more intensity broadening than expected. This could mean the cavity build-up factor is higher than expected (dependent on output coupler transmission), or that the significantly higher saturation parameter has a nonlinear effect on the fluorescence linewidth that has not been accounted for when the model was developed for significantly lower saturation parameters. The Lorentzian component of Fig. 41 was 207 MHz as before, but with Gaussian components of 708 MHz, 756 MHz, and 815 MHz, for increasing power. This shows the intensity broadening through saturation of the second step of the two-step transition is the most significant broadening mechanism for the 760 nm fluorescence, for the 123 nm powers involved in this work. The data in these four figures have been smoothed with a nearest-neighbor averaging filter due to oscillations in the picoammeter that occurred from the sampling parameters.

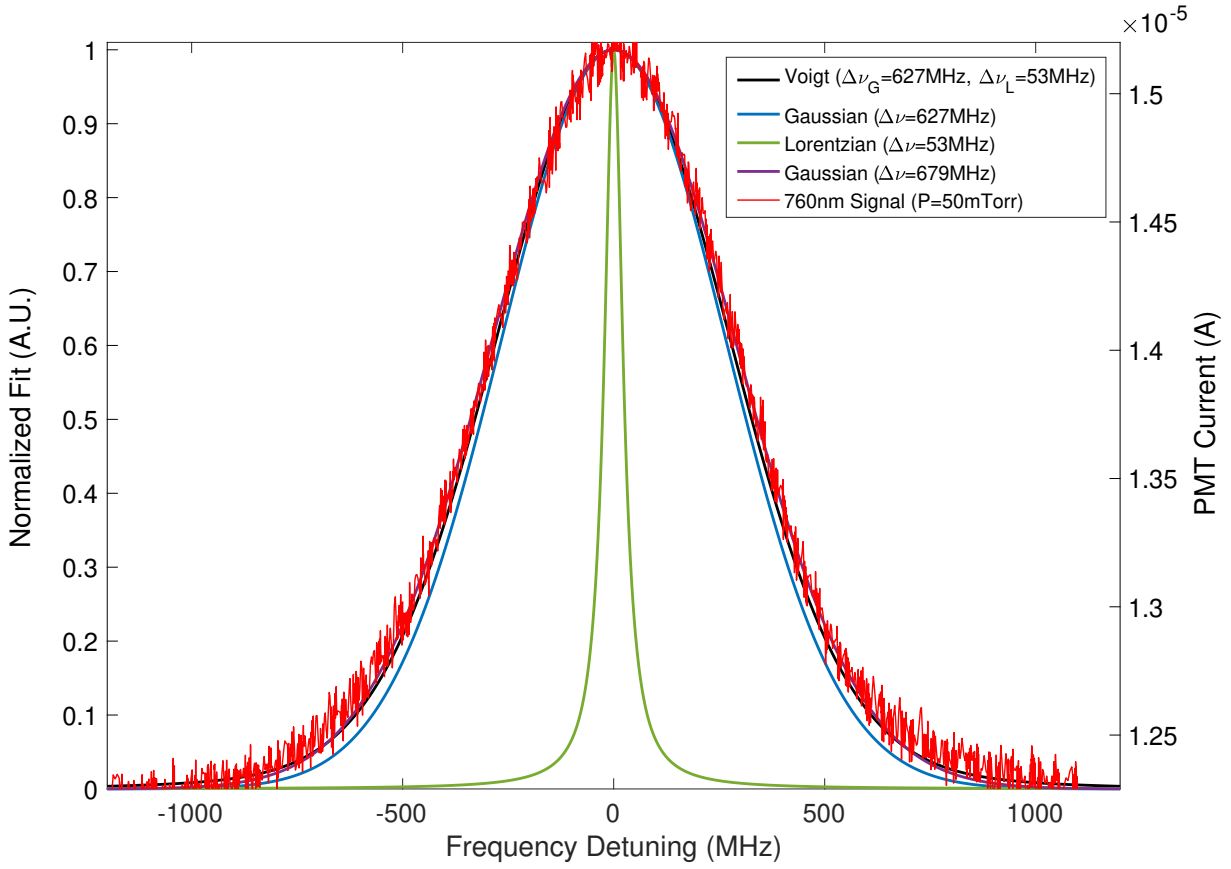

FIG. 38. 819 nm frequency scan at 50 mTorr of Kr with Gaussian, Lorentzian, and Voigt fits..

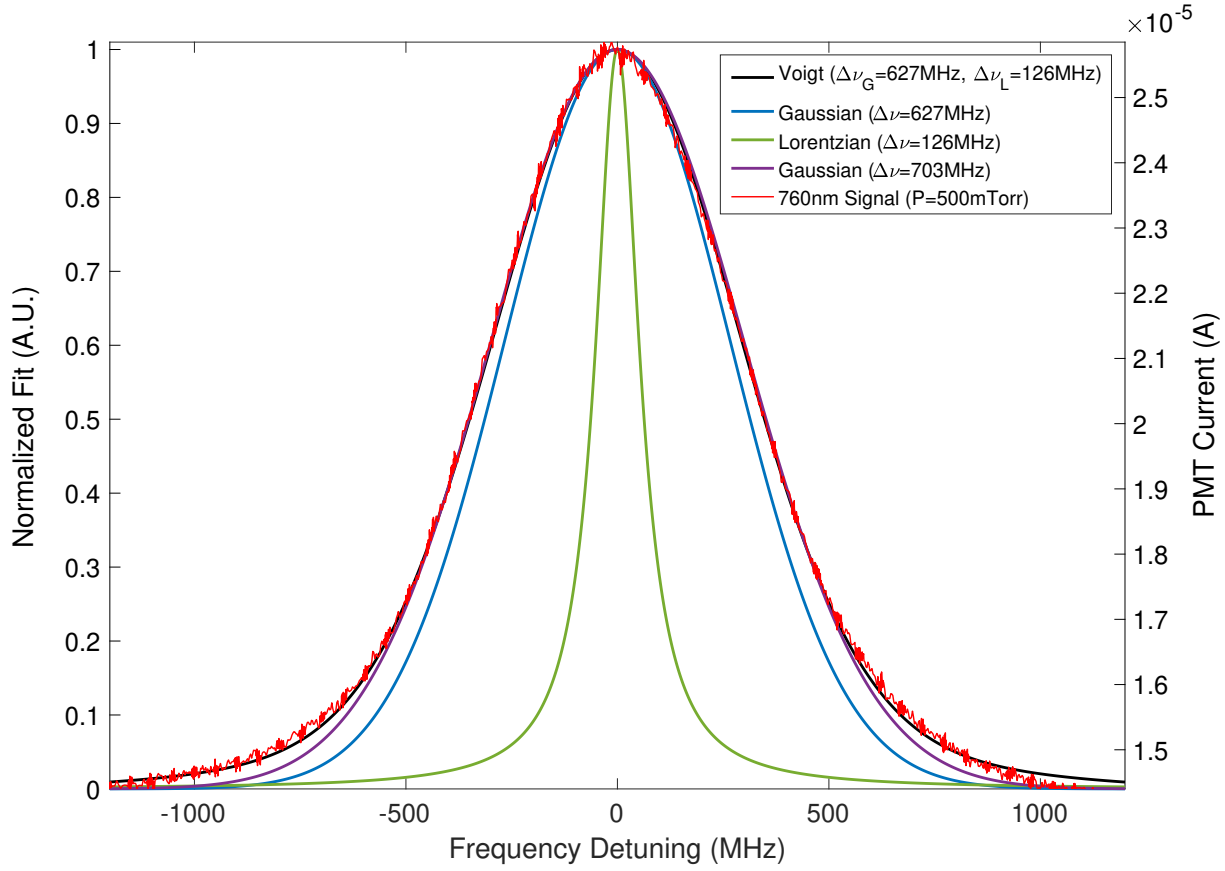

FIG. 39. 819 nm frequency scan at 500 mTorr of Kr with Gaussian, Lorentzian, and Voigt fits.

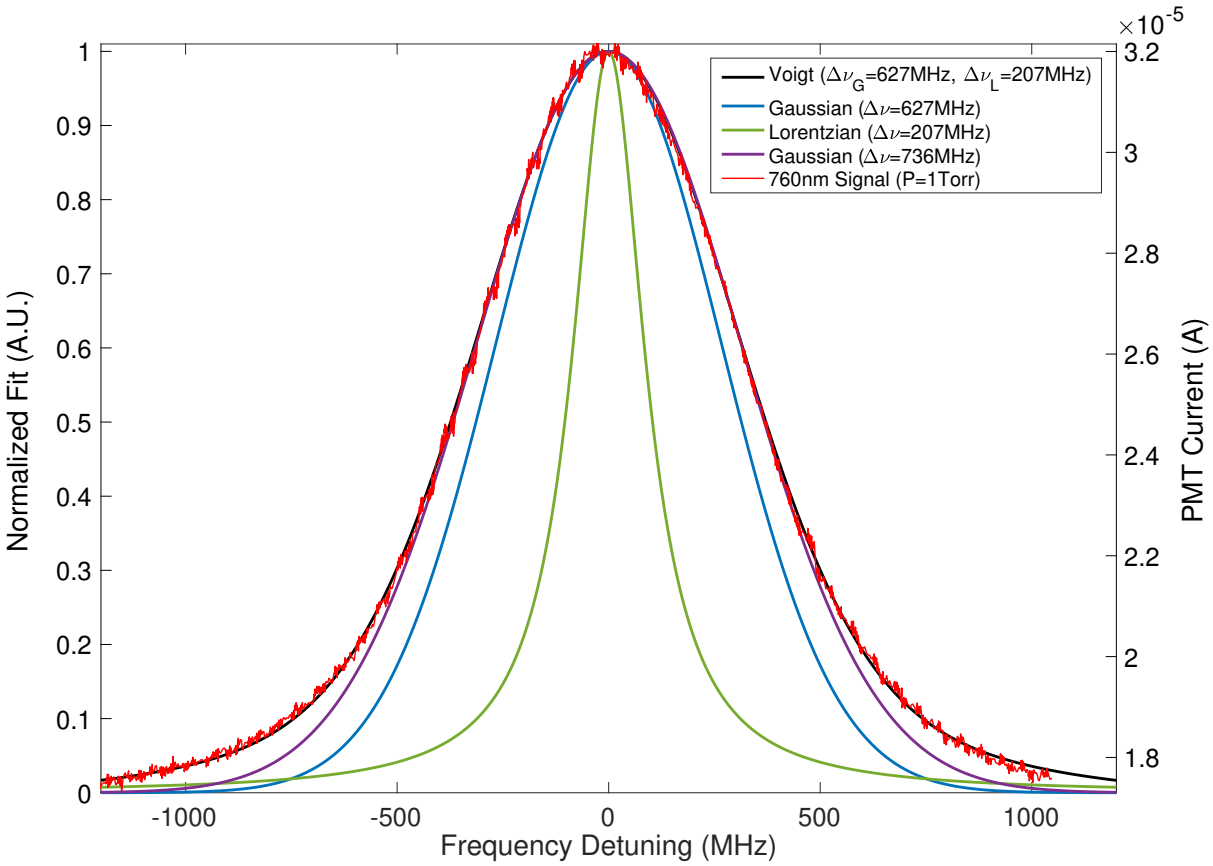

FIG. 40. 819 nm frequency scan at 1 Torr of Kr with Gaussian, Lorentzian, and Voigt fits.

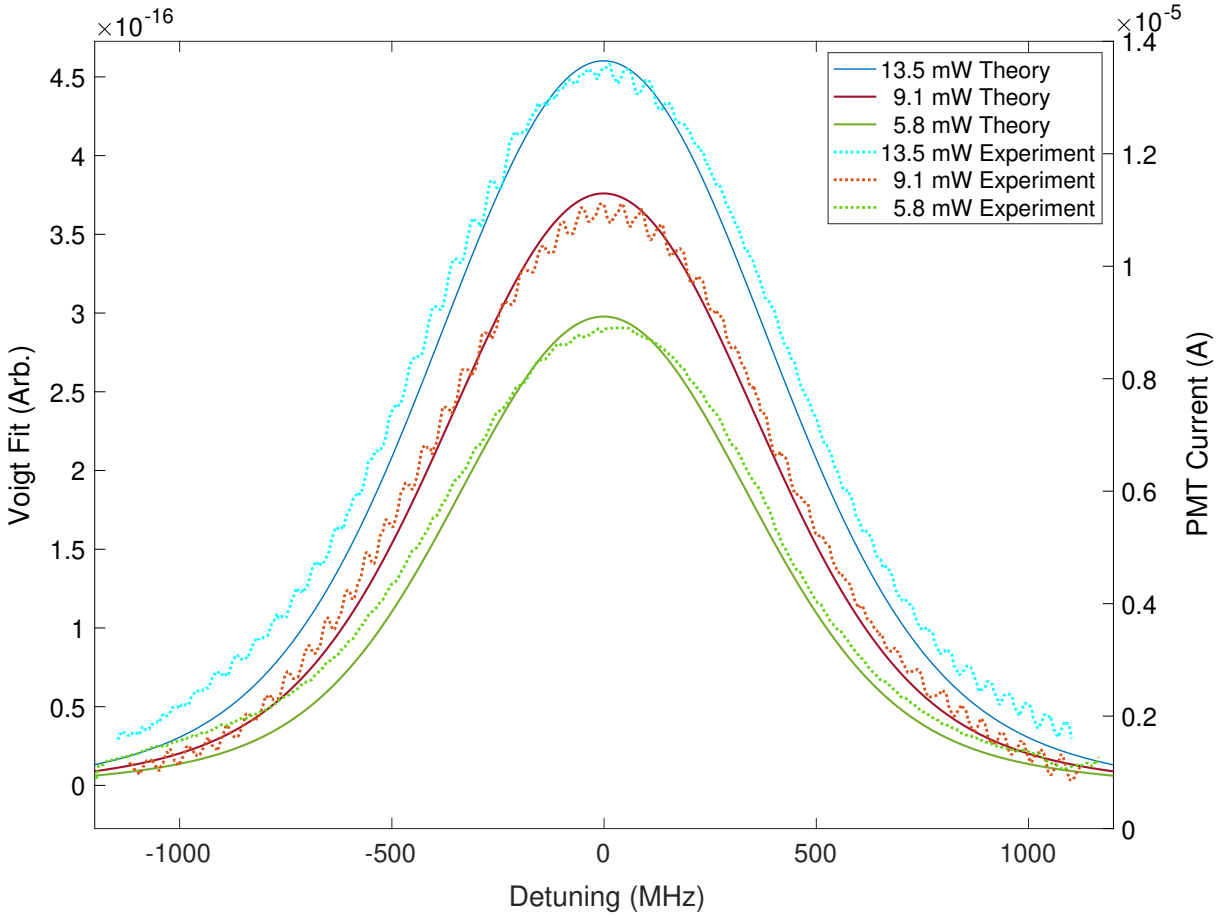

FIG. 41. 819 nm frequency scan at 1 Torr of Kr at various 819 nm powers. The fit is using the same model as the previous three linefunction fits above. The fit is narrower than the data, suggesting the intensity in the cavity is slightly higher than expected.

7.4 Kr* PRODUCTION Kr+He PRESSURE DEPENDENCE

In this section, the second main set of data in this dissertation will be presented. These data investigate the Kr* production as a function of the pressure of a He buffer gas to study the feasibility of an all-optical DPRGL. In order to investigate the plausibility of an all-optical DPRGL, a rather large parameter space needed to be explored where Kr* production was still high enough to populate the metastable state for a laser while having a buffer gas to non-radiatively transition atoms to the laser transition's upper level. Figure 42 shows that Kr* production remains relatively constant below 100 mTorr of He. The Kr* signal was expected to fall the most rapidly at higher Kr+He pressures, but the slope that the signal decreases at for a Kr pressure of 1 Torr is roughly equal to that for 10 mTorr of Kr. The lowest slopes were for Kr pressures of 100-500 mTorr, while the Kr pressure that kept the highest signal at high He pressures was 500 mTorr. Typical ratios used for DPRGL, both experimentally and computationally, have been from 2-6% [14, 15, 19, 22, 74]. With the maximum pressure of 10 Torr in this work, 2-5% represents the 250-500 mTorr that the data show as giving the highest Kr* signal at 10 Torr. These data, compared with the information from literature, suggest that all-optical production maintains the conditions currently expected of a DPRGL in state-of-the-art laser experiments.

An interesting feature in the data show the signal increases slightly around 800 mTorr of He for the Kr pressures of 100 and 250 mTorr. This suggest that there may be a particular set of parameters in this parameter space where the He buffer can increase Kr* production due to increased collisional deactivation from an undesirable state to a state that can lead to Kr* production, such as collisionally counteracting a quench transition.

As a verification of the data presented in 7.2, the He data in Fig. 42 was plotted over data from Fig. 37. The data from Fig. 42 along the y-axis, where P(He)=0, was plotted and can be seen to replicate the double peak, but with a signal an order of magnitude higher due to the higher build-up. This comparison is seen in Fig. 47 in 8.4.3, where the experimental data will be compared to the computational model.

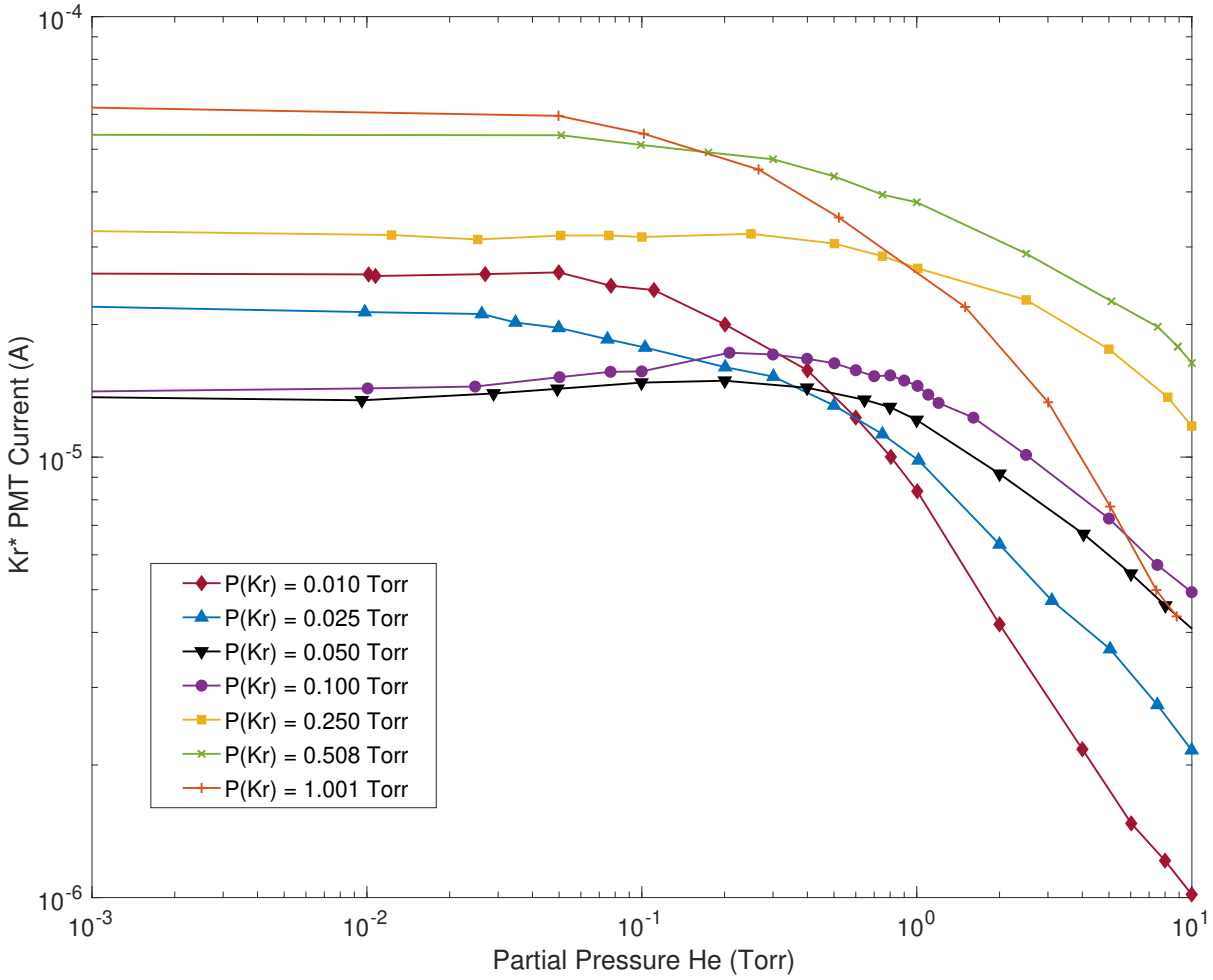

FIG. 42. Kr* production as a function of He buffer partial pressure for varying Kr partial pressures. Cavity gain is ≈ 875, with an input power of 13.5 mW.

CHAPTER 8

THEORETICAL AND COMPUTATIONAL MODELING

The optical Bloch equations used in this computational model can be found from Eqs. (37) to (54). This set of differential equations expresses the Lindblad master equation using the density matrix formulation with decoherence terms from spontaneous emission and collisional relaxation due to other krypton atoms and helium buffer atoms. The set is reduced from the full number of equations to just represent the minimum number of equations to solve all state populations.

Section 8.4 discusses the results of the numerical model. The Kr* production is investigated as the 819 nm power is changed, and the Kr* production is also investigated as the 123 nm power changes. The modeled PMT current includes the PMT quantum efficiency, gain, and collection efficiency. The model parameters were changed as they were in the experiment to see if the simulated current responds in the same way as the experimental results. While the two peak structure that was found in the experimental data was not able to be numerically reproduced, it is believed to be due to radiation trapping. Radiation trapping would require a separate Monte Carlo simulation, which was beyond the scope of this dissertation.

Depending on model parameters, the simulated results can either envelope the two peaks or overlay the lower pressure peak. As the following sections will discuss, the simulated results change in response to 123 nm power by shifting the peak in pressure while changes in 819 nm power changes the amplitude of the peak. This is what is observed in the lower pressure peak in the experimental data. Therefore, it is suggested that radiation trapping caused the higher-pressure peak through balancing the increased resonant scattering of VUV light in the interaction region with decreased VUV light making it to the interaction region. More research on the radiation trapping in Kr* production can be found in [73, 75].

$$K_{ij} = K_{ji} \left(\frac{2j_i + 1}{2j_j + 1} \right) e^{-\frac{|E_i - E_j|}{kT}} \tag{36}$$

8.1 SEMI-CLASSICAL RATE EQUATIONS

$$\begin{aligned}\dot{N}_{1S_0} = \dot{\rho}_{1,1} = &\left(\Gamma_{2,1} + \mathrm{B}_{2,1}\mathrm{I}_{1,2}\left(\frac{\mathrm{s}_{1,2}}{2(1+(\frac{2\delta_{Lamp}}{\Gamma_{2,1}})^2+\mathrm{s}_{1,2})}\right) + \mathrm{K}^{\mathrm{He}}_{2,1}\right)\rho_{2,2} + \Gamma_{5,1}\rho_{5,5} \\ &- \mathrm{B}_{1,2}\mathrm{I}_{1,2}\left(\frac{\mathrm{s}_{1,2}}{2(1+(\frac{2\delta_{Lamp}}{\Gamma_{2,1}})^2+\mathrm{s}_{1,2})}\right)\rho_{1,1} + \left(\frac{1}{\tau_{4,1}} + \mathrm{K}^{\mathrm{Kr}}_{4,1}\right)\rho_{4,4} \\ &+ \left(\frac{1}{\tau_{7,1}} + \mathrm{K}^{\mathrm{Kr}}_{7,1}\right)\rho_{7,7}\end{aligned} \tag{37}$$

$$\begin{aligned}\dot{N}_{1s_4} = \dot{\rho}_{2,2} = &\Gamma_{3,2}\rho_{3,3} + \Gamma_{8,2}\rho_{8,8} + \Gamma_{9,2}\rho_{9,9} + \Gamma_{10,2}\rho_{10,10} + \Gamma_{11,2}\rho_{11,11} + \frac{i\Omega_{L1}}{2}(\rho_{2,3} - \rho_{3,2}) \\ &- \left(\Gamma_{2,1} + \mathrm{B}_{2,1}\mathrm{I}_{1,2}\left(\frac{\mathrm{s}_{1,2}}{2(1+(\frac{2\delta_{Lamp}}{\Gamma_{2,1}})^2+\mathrm{s}_{1,2})}\right) + \mathrm{K}^{\mathrm{He}}_{2,1} + \mathrm{K}^{\mathrm{Kr}}_{2,4} + \mathrm{K}^{\mathrm{He}}_{2,4}\right)\rho_{2,2} \\ &+ (\mathrm{K}^{\mathrm{He}}_{4,2} + \mathrm{K}^{\mathrm{Kr}}_{4,2})\rho_{4,4} + \mathrm{B}_{1,2}\mathrm{I}_{1,2}\left(\frac{\mathrm{s}_{1,2}}{2*(1+(\frac{2\delta_{Lamp}}{\Gamma_{2,1}})^2+\mathrm{s}_{1,2})}\right)\rho_{1,1}\end{aligned} \tag{38}$$

$$\begin{aligned}\dot{N}_{2p_6} = \dot{\rho}_{3,3} = &-(\Gamma_{3,2} + \Gamma_{3,4} + \Gamma_{3,5} + \mathrm{K}^{\mathrm{Kr}}_{3,6} + \mathrm{K}^{\mathrm{Kr}}_{3,8} + \mathrm{K}^{\mathrm{Kr}}_{3,9} + \mathrm{K}^{\mathrm{Kr}}_{3,10} + \mathrm{K}^{\mathrm{Kr}}_{3,11} + \mathrm{K}^{\mathrm{He}}_{3,12})\rho_{3,3} \\ &+ \frac{i\Omega_{L1}}{2}(\rho_{3,2} - \rho_{2,3}) + \frac{i\Omega_{L2}}{2}(\rho_{3,4} - \rho_{4,3}) + \mathrm{K}^{\mathrm{Kr}}_{6,3}\rho_{6,6} + \mathrm{K}^{\mathrm{Kr}}_{8,3}\rho_{8,8} + \mathrm{K}^{\mathrm{Kr}}_{9,3}\rho_{9,9} \\ &+ \mathrm{K}^{\mathrm{Kr}}_{10,3}\rho_{10,10} + \mathrm{K}^{\mathrm{Kr}}_{11,3}\rho_{11,11} + \mathrm{K}^{\mathrm{He}}_{12,3}\rho_{12,12}\end{aligned} \tag{39}$$

$$\begin{aligned}\dot{N}_{1s_5} = \dot{\rho}_{4,4} = &\Gamma_{3,4}\rho_{3,3} + \Gamma_{6,4}\rho_{6,6} + \Gamma_{9,4}\rho_{9,9} + \Gamma_{10,4}\rho_{10,10} + \Gamma_{11,4}\rho_{11,11} + (\mathrm{K}^{\mathrm{Kr}}_{2,4} + \mathrm{K}^{\mathrm{He}}_{2,4})\rho_{2,2} \\ &- \left(\frac{1}{\tau_{4,1}} + \mathrm{K}^{\mathrm{Kr}}_{4,1} + \mathrm{K}^{\mathrm{He}}_{4,2} + \mathrm{K}^{\mathrm{Kr}}_{4,2}\right)\rho_{4,4} + \frac{i\Omega_{L2}}{2}(\rho_{4,3} - \rho_{3,4}) + \frac{i\Omega_{L3}}{2}(\rho_{4,6} - \rho_{6,4})\end{aligned} \tag{40}$$

$$\dot{N}_{1s_2} = \dot{\rho}_{5,5} = \Gamma_{3,5}\rho_{3,3} + \Gamma_{6,5}\rho_{6,6} + \Gamma_{8,5}\rho_{8,8} + \Gamma_{10,5}\rho_{10,10} + \Gamma_{12,5}\rho_{12,12} - \Gamma_{5,1}\rho_{5,5} \tag{41}$$

$$\dot{N}_{2p_9} = \dot{\rho}_{6,6} = -(\Gamma_{6,4} + K^{Kr}_{6,3} + K^{Kr}_{6,10} + K^{He}_{6,10} + K^{Kr}_{6,11} + K^{He}_{6,12})\rho_{6,6} + \frac{i\Omega_{L3}}{2}(\rho_{6,4} - \rho_{4,6}) + K^{Kr}_{3,6}\rho_{3,3} + K^{Kr}_{10,6}\rho_{10,10} + K^{He}_{10,6}\rho_{10,10} + K^{Kr}_{11,6}\rho_{11,11} + K^{He}_{12,6}\rho_{12,12} \tag{42}$$

$$\dot{N}_{1s_3} = \dot{\rho}_{7,7} = -\left(\frac{1}{\tau_{7,1}} + \mathrm{K}^{\mathrm{Kr}}_{7,1}\right)\rho_{7,7} + \Gamma_{9,7}\rho_{9,9} + \Gamma_{11,7}\rho_{11,11} \tag{43}$$

$$\dot{\rho}_{3,2} = -\frac{1}{2}(\Gamma_{2,1} + \Gamma_{3,2} + \Gamma_{3,4} + \Gamma_{3,5} + 2i\delta_{L1})\rho_{3,2} + \frac{i\Omega_{L1}}{2}(\rho_{3,3} - \rho_{2,2}) - \frac{i\Omega_{L2}}{2}\rho_{4,2} \tag{44}$$

$$\dot{\rho}_{4,2} = -\frac{1}{2}(\Gamma_{2,1} + \Gamma_{6,4} + i(\delta_{L_1} - \delta_{L_2}))\rho_{4,2} + \frac{i\Omega_{L1}}{2}\rho_{4,3} - \frac{i\Omega_{L2}}{2}\rho_{3,2} - \frac{i\Omega_{L3}}{2}\rho_{6,2} \tag{45}$$

$$\dot{\rho}_{4,3} = -\frac{1}{2}(\Gamma_{6,4} + \Gamma_{3,2} + \Gamma_{3,4} + \Gamma_{3,5} + 2i\delta_{L_2})\rho_{4,3} + \frac{i\Omega_{L1}}{2}\rho_{4,2} + \frac{i\Omega_{L2}}{2}(\rho_{4,4} - \rho_{3,3}) - \frac{i\Omega_{L3}}{2}\rho_{6,3} \tag{46}$$

$$\dot{\rho}_{6,2} = -\frac{1}{2}(\Gamma_{6,4} + \Gamma_{3,2} + \Gamma_{2,1} + i(\delta_{L_3} - \delta_{L_2} + \delta_{L_1}))\rho_{6,2} + \frac{i\Omega_{L1}}{2}\rho_{6,3} - \frac{i\Omega_{L3}}{2}\rho_{4,2} \tag{47}$$

$$\dot{\rho}_{6,3} = -\frac{1}{2}(\Gamma_{6,4} + \Gamma_{3,2} + \Gamma_{3,4} + \Gamma_{3,5} + i(\delta_{L_3} - \delta_{L_2}))\rho_{6,3} + \frac{i\Omega_{L1}}{2}\rho_{6,2} + \frac{i\Omega_{L2}}{2}\rho_{6,4} - \frac{i\Omega_{L3}}{2}\rho_{4,3} \tag{48}$$

$$\dot{\rho}_{6,4} = -\frac{1}{2}(\Gamma_{6,4} + \Gamma_{3,4} + 2i\delta_{L_3})\rho_{6,4} + \frac{i\Omega_{L2}}{2}\rho_{6,3} + \frac{i\Omega_{L3}}{2}(\rho_{6,6} - \rho_{4,4}) \tag{49}$$

$$\dot{N}_{2p_5} = \dot{\rho}_{8,8} = K^{Kr}_{3,8}\rho_{3,3} - (\Gamma_{8,2} + \Gamma_{8,5} + K^{Kr}_{8,3})\rho_{8,8} \tag{50}$$

$$\dot{N}_{2p_7} = \dot{\rho}_{9,9} = -(\Gamma_{9,5} + \Gamma_{9,7} + \Gamma_{9,4} + \Gamma_{9,2} + K^{Kr}_{9,10} + K^{Kr}_{9,3})\rho_{9,9} + K^{Kr}_{3,9}\rho_{3,3} + K^{Kr}_{10,9}\rho_{10,10} \tag{51}$$

$$\begin{aligned}\dot{N}_{2p_8} = \dot{\rho}_{10,10} = &-(\Gamma_{10,5} + \Gamma_{10,2} + \Gamma_{10,4} + K^{He}_{10,12} + K^{Kr}_{10,11} + K^{He}_{10,11} + K^{Kr}_{10,9} \\ &+ K^{Kr}_{10,6} + K^{He}_{10,6} + K^{Kr}_{10,3})\rho_{10,10} + K^{He}_{12,10}\rho_{12,12} + (K^{Kr}_{11,10} + K^{He}_{11,10})\rho_{11,11} \\ &+ K^{Kr}_{9,10}\rho_{9,9} + (K^{Kr}_{10,6} + K^{He}_{10,6})\rho_{6,6} + K^{Kr}_{3,10}\rho_{3,3}\end{aligned} \tag{52}$$

$$\begin{aligned}\dot{N}_{2p_{10}} = \dot{\rho}_{11,11} = &-(\Gamma_{11,7} + \Gamma_{11,5} + \Gamma_{11,4} + \Gamma_{11,2} + K^{Kr}_{11,3} + K^{Kr}_{11,6} + K^{Kr}_{11,10} + K^{He}_{11,10})\rho_{11,11} \\ &+ K^{Kr}_{3,11}\rho_{3,3} + (K^{Kr}_{10,11} + K^{He}_{10,11})\rho_{10,10} + K^{Kr}_{6,11}\rho_{6,6}\end{aligned} \tag{53}$$

$$\begin{aligned}\dot{N}_{3d} \ = \dot{\rho}_{12,12} = &-(K^{He}_{12,11} + K^{He}_{12,10} + K^{He}_{12,3})\rho_{12,12} + K^{He}_{11,12}\rho_{11,11} \\ &+ K^{He}_{10,12}\rho_{10,10} + K^{He}_{3,12}\rho_{3,3}\end{aligned} \tag{54}$$

8.2 RADIATIVE AND NON-RADIATIVE DECAY RATES

The rate coefficients have been taken from various sources to include radiative and non-radiative rate coefficients, which can be found in Appendix A. Table 2 shows all of the radiative transition rates, and the energy level diagram, Fig. 43, shows the labels of the states. The 3d manifold is included due to a non-negligible rate from 2p states to some 3d states that are then effectively lost to the laser system. Therefore, no radiative terms from the 3d manifold are included, and only collisional relaxations to and from 1s or 2p states are allowed.

Collisional (non-radiative) rate coefficients can be found in Table 4 for a buffer gas of helium, and Table 3 contains the rates for krypton-krypton collisions. The rates are in units of $s^{-1}cm^{-3}$, which requires the number density to be calculated. The number density was assumed to be constant throughout the experimental cell, which is a reasonable approximation for a room temperature gas cell with no strong external fields. If the reverse process rate is not defined in the chart, it can be calculated using Eq. (36).

All significant primary collisional relaxations were included, which were collisional relaxations between the levels directly involved in the production of metastables and of the laser. Secondary relaxations were included, which were relaxations from, or to, a level that is not directly involved in metastable production or the laser. Tertiary collisional relaxations were not included due to the assumption that the probability of that atom collisionally transitioning back to a primary level is sufficiently low.

8.3 5-LEVEL LINDBLAD RESULTS

The results in Fig. 44 show the fundamental part of the major model in this dissertation, which is the solution of the Lindblad master equations for the five levels directly involved in the production of Kr*. These states include the ground state $^1S_0$, the first excited state $1s_4$, the upper excited state $2p_6$, the metastable state $1s_5$, and the $1s_2$ state, which has a very low branching ratio from $2p_6$ and is nearly negligible. This simulation assumed the entire population at t=0 is in the $1s_4$ state and that there is no optical pumping out of the ground state. The oscillations due to the addition of coherent states can be seen. However, the intensity of the pump is not high enough to see a dramatic example of Rabi oscillations between $1s_4$ and $2p_6$, or the effect those oscillations have on the ground state population. The results of this simulation match those presented in the appendix of [12].

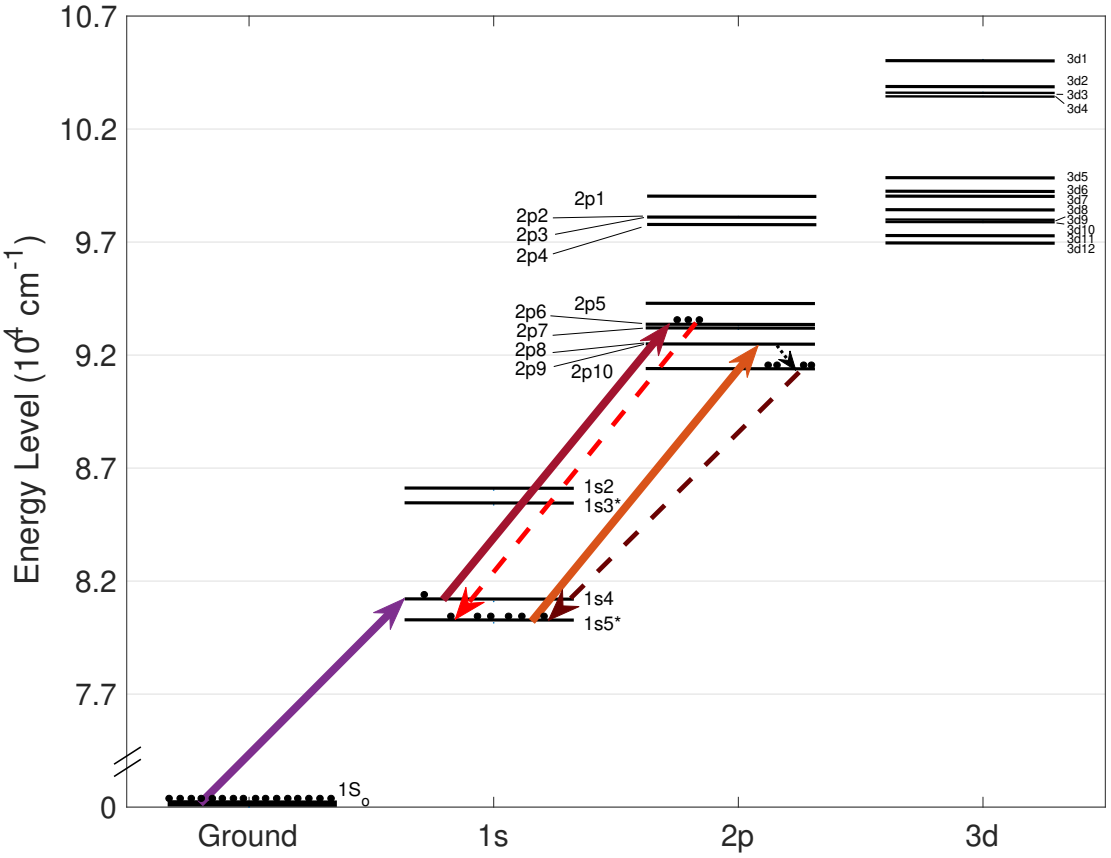

FIG. 43. Energy level diagram of relevant krypton levels for Kr* production and the DPRGL. Solid lines are excitation, dashed lines are fluorescence, and dotted lines are collisional relaxation. The purple excitation is the incoherent 123 nm lamp, the dark red excitation is the 819 nm laser, and the orange excitation is the 811 nm pump of the laser. The red fluorescence is the radiative transition to the metastable state and the dark red fluorescence is the 893 nm DPRGL emission. The black dotted line is the collisional relaxation of the He buffer gas from $2p_9$ to $2p_{10}$. 3d levels are included because the model includes collisional rates to/from some low-laying 3d levels. Experimental energy levels used in the figure are from [72, 76].

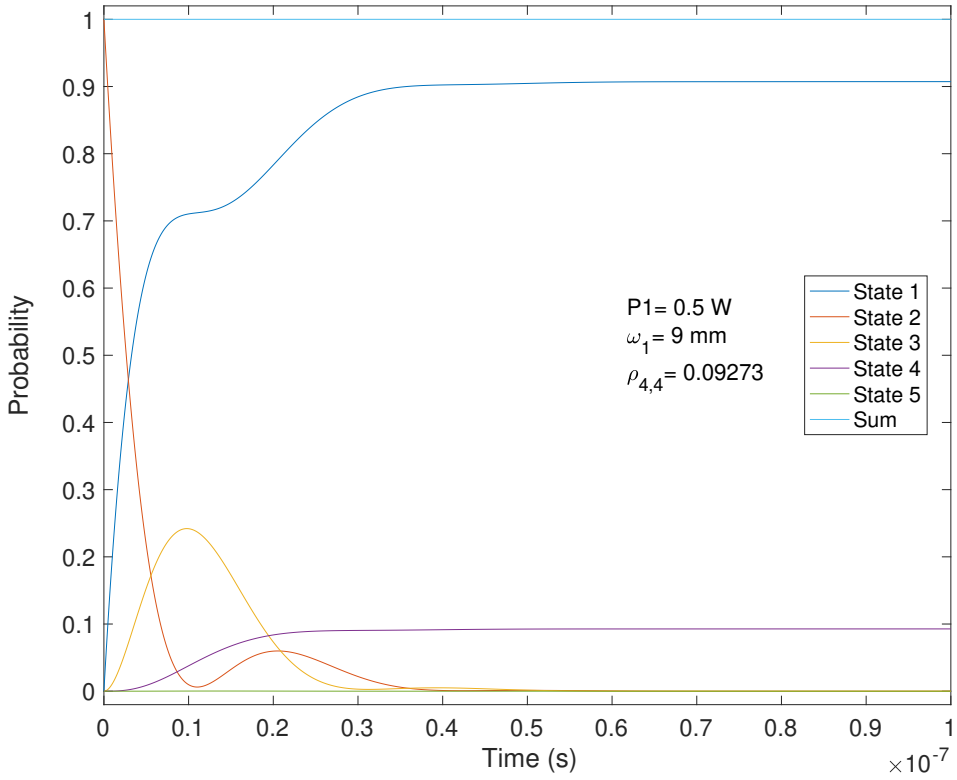

FIG. 44. This figure shows the simulation of the 5 states involved in all-optical Kr* (state 4) production via a VUV+NIR two-step transition. The parameters are taken to be a NIR power of 0.5 W with a waist of 9 mm, and the initial population is entirely in state 2, the first excited state. The VUV power is inconsequential due to the dynamics involved. The energy level numbers are the same used in Fig. 6 of [12], except the model in this dissertation put the zero energy level as ground, state 1.

8.4 NUMERICAL MODEL RESULTS

The following results represent the model simulated over 1μs. The first result shows the effect 819 nm power has on the Kr* signal and how saturation occurs. The second shows how the 123 nm lamp power changes the Kr* signal. The experimental lamp power is give as a percentage of RF power to the lamp's discharge, and therefore does not correlate directly to lamp 123 nm power. The value of lamp power is given as photon intensity (photons/s/sr) by the manufacturer. Estimated over the expected cone of illumination of 0.28 sr gives the expected photon flux, and assumes the given flux is within the Doppler width. This indirect RF power to photon flux relationship, along with the lack of a VUV detector, makes modeling the RF lamp difficult. The following section looks at matching the experimental data to the model and discusses the results.

8.4.1 Kr* PRODUCTION AS A FUNCTION OF 819 NM POWER

When studying the response of the model to changes in the 819 nm power and a fixed lamp power, one can see the saturation occur as it would if it were a normal one-photon transition. However, in reality, the intensity of the VUV light affects the $1s_4$ population, which in turns affects the effective saturation intensity of the 819 nm transition from $1s_4$ to $2p_6$. As the 819 nm power decreases by an order of magnitude, the simulated PMT current, shown in Fig. 45, eventually decreases an equal amount at lower powers, showing the linearity of the effective one-photon transition. From 2.4, a resonant two-step transition fluoresces linearly with the intensities when not in saturation. Since the saturation parameter of the lamp was less than $5{\cdot}10^{-6}$ in the experiment, the only saturation occurring in the experiment would be the $1s_4$ to $2p_6$ transition. The saturation power, for the given waist, of this transition is estimated to be 3.7 μW, approximately the power at which the nonlinearity starts in the Fig. 45.

8.4.2 Kr* PRODUCTION AS A FUNCTION OF 123 NM POWER

The effect that the VUV intensity has on the Kr* production rate is a much more complicated relationship than for the NIR intensity. Saturation is seen in Fig. 46 even though the saturation parameters in the figure, for the given waist of 10 mm, are only $4.8{\cdot}10^{-5}$, 10^{-6}, and 10^{-7}. In the figure, the NIR light is shown with saturation parameters of $3{\cdot}10^{6}$, 30, and 3.

The colors in Fig. 37 correspond to the same VUV intensity while the same line type

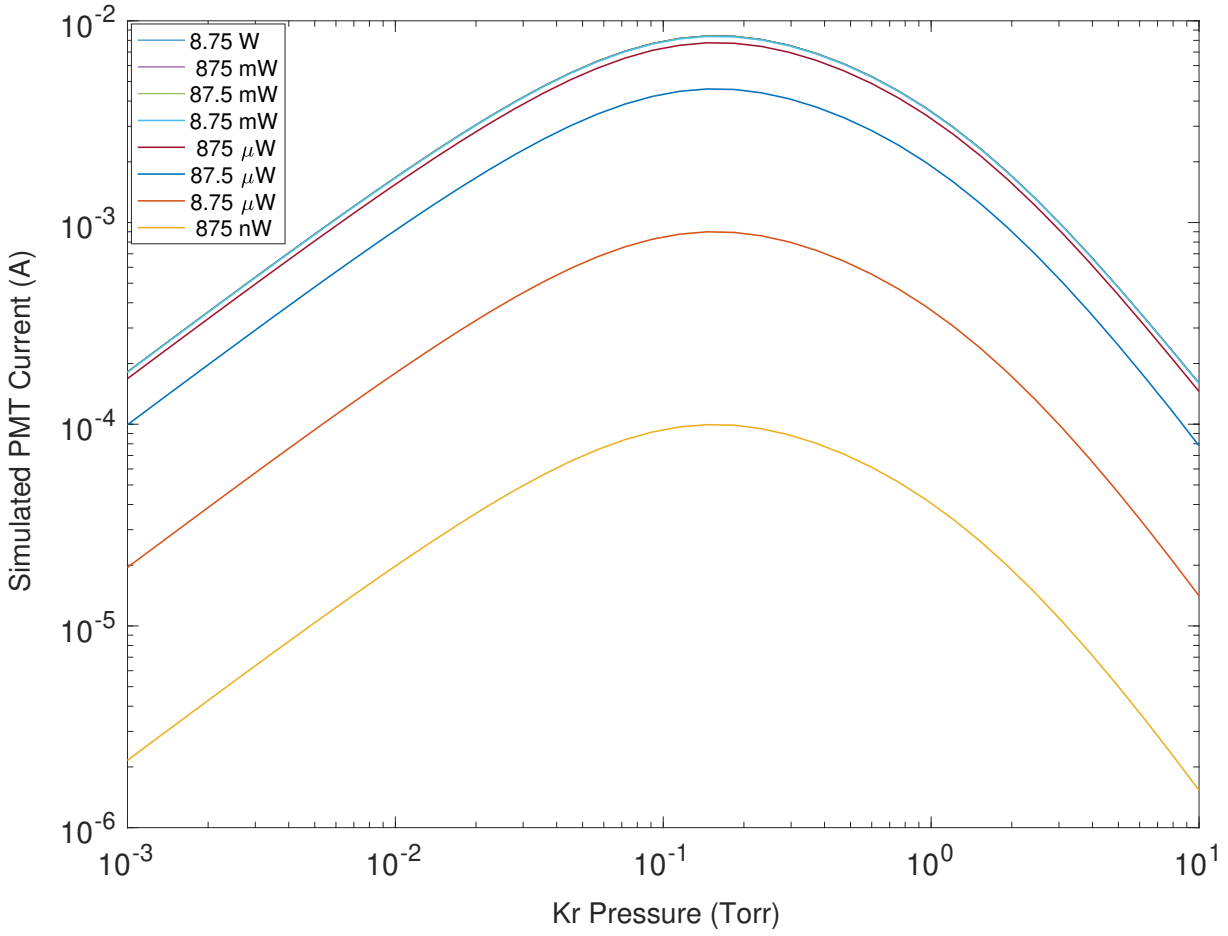

FIG. 45. Simulated Kr* production as a function of pressure at various 819 nm powers. The VUV lamp intensity was set as 2.65 W/m^{-2}, and the cavity waist was set at 400 μm with a gain of 875. The three highest powers are not visible behind the 8.75 mW curve due to saturation.

corresponds to the same NIR intensity. It can be seen that at higher VUV intensities, the shape of the curve becomes distorted with the least amount of saturation near the peak. As the VUV intensities decrease the saturation of the NIR become the most prominent. Another feature of the change in VUV intensity is the shift of the peak towards the higher pressure and lower signal amplitude as the VUV intensity decreases. This can be viewed as the higher intensities reaching the interaction region more at lower pressures where the saturation intensity is higher, while the saturation intensity decreases at higher pressure where less VUV light reaches the interaction region.

Young *et al.* shows a decrease in saturation power with pressure across 10^{-5}-10^{-1} Torr. The model presented in this dissertation also shows a reduction in the saturation power with pressure. At higher pressures, this is very noticeable, which is also a feature seen in the experimental data. The experimental data also shows a similar spacing as the model in the signal at lower pressures when the VUV intensity changes.

8.4.3 Kr* PRODUCTION - EXPERIMENT VS MODEL

The data were compared to the computational model with parameters mentioned in 8.2. With the rates given in literature and the parameters of the experiment, the simulation replicated the data quite well in magnitude and shape. The double peak shape is believed to be a complicated combination of radiation trapping and self-reversal as discussed in 8. Self-reversal of the line means that the multiple scattering of the VUV light off ground state Kr shifts the light closest to resonance away from resonance. This creates a double peak feature with the light being mostly in the wings of the linefunction. So, rather than being completely lost, it can now excite a new velocity class. In a cell, this is not much of a problem due to the 3-dimensional velocity distribution. In an atomic beam, the pressure outside of the beam would be low enough to not scatter very much unless it were a beam of a large diameter. In that case, the excitation geometry would need to be selected to maximize the two frequency distributions.

The shape of the model varied rather strongly depending on the parameters of collisional deactivation rates from the 1s manifold. These values were not found to be precisely measured, and thus several values were selected across an order of magnitude. As one may suspect, as the total deactivation rates from the short-lived $1s_2$ and $1s_4$ states increase, the Kr* production peak shifts towards lower pressures due to the 1s manifold not being able to be sufficiently populated. With the best estimate for the deactivation rates from literature, Fig. 47 shows that the simulation forms an envelope over the two peaks. As the intensities

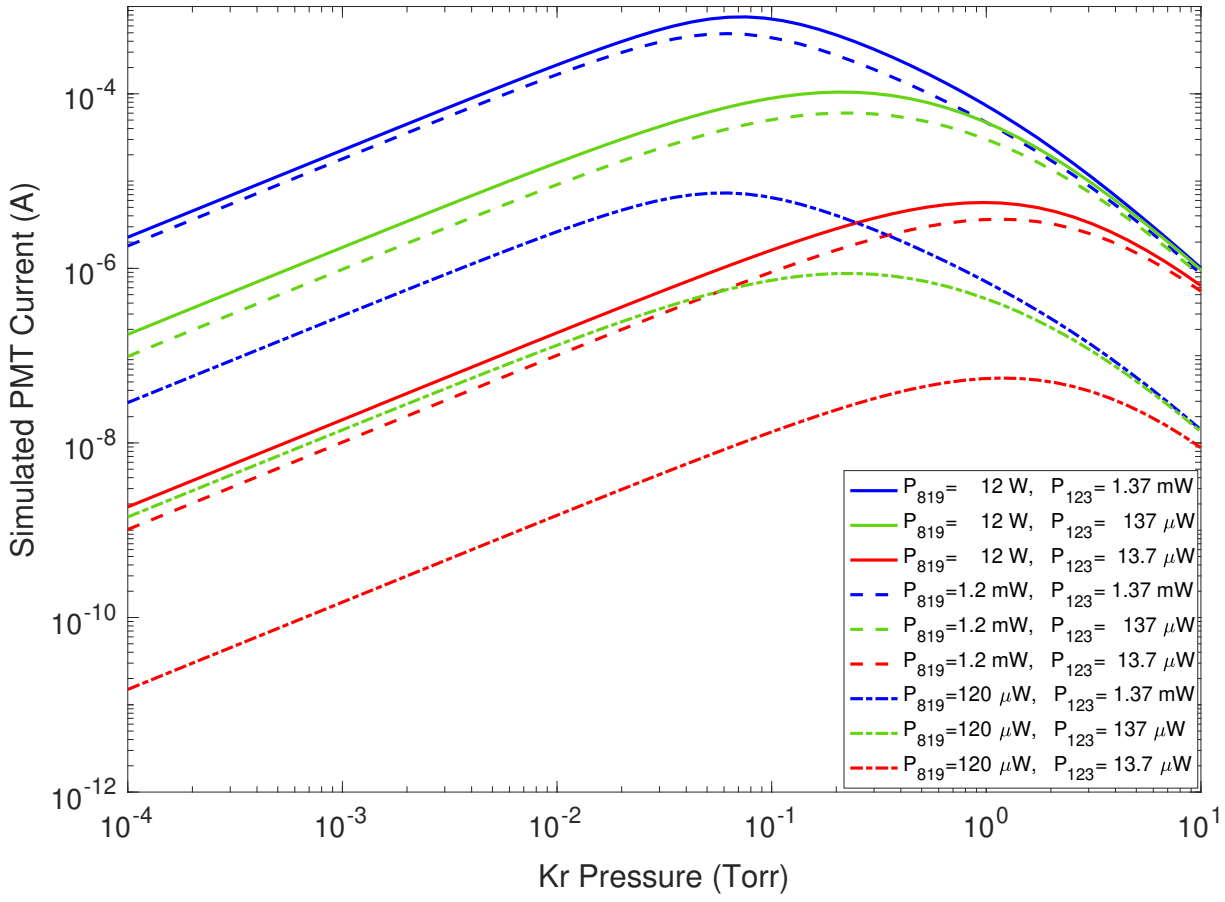

FIG. 46. Simulated Kr* production as a function of pressure at various 123 nm powers.

of the light change, they behave as one would expect, with the 819 nm light causing the amplitude to change and the 123 nm light causing the peak to shift along with a change in amplitude. The fact that the data agree so well also suggests that the measured cavity build-up and the estimated lamp intensity are reasonable values.

However, with different values for deactivation rates, one can get the simulated data to line up well with the lower pressure peak and for shifts in the peak to respond as expected according to pressure and light intensities. While the values necessary to produce this fit are further from estimates in literature, this result would suggest the high pressure peak being caused by radiation trapping at higher pressures and increasing the effective lamp intensity. With the deactivation rates as best estimated from literature, as used in the figures, the data suggest some sort of resonance happening around 100 mTorr where a transition occurs between a collisional deactivation regime at lower pressures to a radiation trapping regime at higher pressures. Another possibility would be that the low amount of self-reversal at lower pressures means that VUV light is scattered away before reaching the interaction region, and at higher pressures the large amount of self-reversal allows the VUV light to multiply scatter enough to reach the interaction region. More data needs to be taken with specific VUV equipment to truly understand what interactions occur with the VUV light before and inside the interaction region. To better understand this phenomenon in a theoretical and computational capacity, Monte Carlo simulations for radiation transport of VUV light through the Kr cell would need to be performed in combination with the semi-classical model discussed in this dissertation [11, 73].

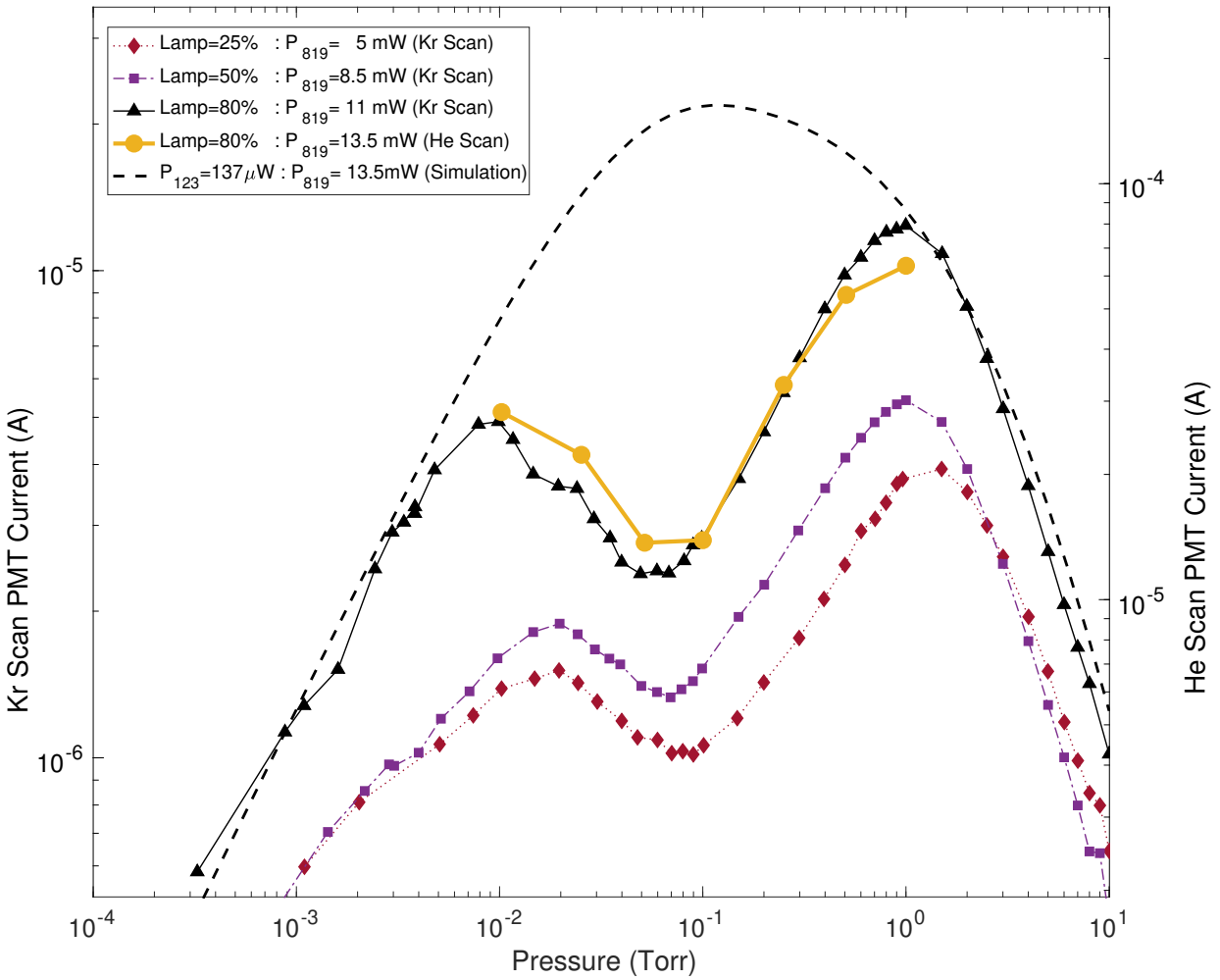

FIG. 47. Simulated Kr* production fit to experimental data from. The yellow line represents the data from the Kr+He measurements when there was no He added yet (data taken along the y axis of Fig. 37. This provides another reproducibility check of previous data using the Kr+He data. This figure also shows how the model overlaps the data, which is presented on the same scale (right axis). The Kr scan data (left axis) have a cavity gain of 56 while the He scan and the simulation have a cavity gain of 875.

CHAPTER 9

CONCLUSIONS AND FUTURE WORK

The research presented in this dissertation investigated the viability of using a low-powered diode laser and a commercial VUV lamp for all-optical production of Kr*, with direct applicability to all-optical production of other metastable rare gases. A custom vacuum chamber with a PDH-stabilized build-up cavity was realized with a finesse of 1900, giving a build-up factor of approximately 875. This gain allowed the use of a much lower-powered laser than previously used in all-optical experiments that typically used Ti:Sapphs or tapered amplifiers. These solutions are expensive, bulky, or both, while a low-powered diode laser and a build-up cavity can be built incredibly compact with the build-up factor being controlled by mirror reflectance values.

The theoretical model of the 5-level system for Kr* production was developed using the Lindblad master equation, and resulted in the exact same steady-state population of the metastable state of 0.093 as in [11] when all of the initial population is in the first excited state, $1s_4$. This result can be seen in Fig. 44. However, this dissertation investigated this model through the use of incoherent excitation out of the ground state using the estimated parameters of the VUV lamp, which showed saturation of the $1s_4$ state to be unlikely with current VUV lamp configurations available. Therefore, the conversion efficiency of current systems are likely lower than what should potentially be obtained with saturation of the 123 nm transition. The Lindblad model in this work was later expanded to include collisional deactivations and more energy levels to use it as a theoretical model for the DPRGL.

The estimated production rates obtained in this work using the high finesse cavity were of the same order of magnitude as state-of-the-art measurements done by Z.T. Lu *et al.* in [11], despite using a much lower-powered laser and a VUV lamp an order of magnitude less intense than in their work. With better focusing of the VUV lamp, and the addition of more lamps, this number can be expected to increase significantly due to the low saturation parameter of the 123 nm transition in these experiments. These results also show the technique transfers quite well between a cell experiment and an atomic beam experiment, making it ideal for both ATTA and production of DPRGL.

This research also investigated the Kr* production in the presence of a He buffer gas to further explore the all-optical production parameter space for a DPRGL. These results agree

with experimental and theoretical literature on the optimal ratio of Kr to He of 2-6% Kr, while using all-optical production methods rather than the glow discharges used in other works.

9.1 FUTURE EXPERIMENT AND MODEL ADJUSTMENTS

The analytic and computational models of the system need to be expanded upon to include the radiation trapping that is discussed in the literature. However, modeling radiation trapping requires its own radiation transport modeling through means such as a Monte-Carlo simulation as in Young *et al.* [73].

Further data would need to be taken to experimentally probe the fluorescence linewidth of this two-step transition from $2p_6$ to $1s_5$. As described in the experimental results, the Doppler component of the fitted Voigt function is broader than the model currently estimates. More 819 nm frequency scans would help enlighten whether this broadening is intensity-dependent on the NIR laser, while the ability to use a monochromator to scan the 123 nm frequency would allow a much more thorough investigation of the 760 nm fluorescence parameter space.

The addition of more pressure transducers to cover a wider range of pressures, both lower (for ATTA), and higher (for DPRGL) would be the next move to expand these data. However, due to the difficulty of keeping a large cell at pressure with no pumping, improvements on the cell's vacuum system would need to be made to make measurements at pressures below 1 mTorr.

For future use, it would be good to be able to monitor the VUV lamp intensity to make sure the intensity is consistent between data runs and that the MgF_2 window is kept as transparent as possible. Also, using a VUV mirror to retroreflect the VUV light back into the interaction region would increase the efficiency with respect to lamp output significantly for lower pressures. Its benefit at higher pressures depends on the resonant scattering as the pressure increases.

One final modification would be to include a Ly-α passband filter at the output of the VUV lamp. Due to the glow discharge nature of the VUV lamp, the lamp outputs the full discrete atomic spectrum of not only neutral Kr, but also of ionized species, depending on the discharge power. This gives a significant background in the 760 nm signal when doing fluorescence detection. While there is also an 811 nm background from the lamp, switching to 811 nm scattering detection would significantly increase the SNR due to the higher achievable radiance of the method and the ability to effectively use lock-in detection.

REFERENCES

[1] H.-C. Lee, Review of inductively coupled plasmas: Nano-applications and bistable hysteresis physics, Appl. Phys. Rev. **5**, 011108 (2018).

[2] W. Vassen, C. Cohen-Tannoudji, M. Leduc, D. Boiron, C. I. Westbrook, A. Truscott, K. Baldwin, G. Birkl, P. Cancio, and M. Trippenbach, Cold and trapped metastable noble gases, Rev. Mod. Phys. **84**, 175 (2012).

[3] C. Y. Chen, Y. M. Li, K. Bailey, T. P. Connor, L. Young, and Z. T. Lu, Ultrasensitive Isotope Trace Analyses with a Magneto-Optical Trap, Science **286**, 1139 (1999).

[4] H Oeschger and M Wahlen, Low Level Counting Techniques, Annu. Rev. Nucl. Sci. **25**, 423 (1975).

[5] C. Tuniz, Accelerator mass spectrometry: ultra-sensitive analysis for global science, Radiat. Phys. Chem. **61**, 8th International Symposium on Radiation Physics - ISRP8, 317 (2001).

[6] Z. Feng, S. Ebser, L. Ringena, F. Ritterbusch, and M. K. Oberthaler, Bichromatic force on metastable argon for atom-trap trace analysis, Phys. Rev. A **96**, 013424 (2017).

[7] H. J. Metcalf, *Laser Cooling and Trapping* (Springer, New York, 1999).

[8] Y. Ding, S. M. Hu, K. Bailey, A. M. Davis, R. W. Dunford, Z. T. Lu, T. P. O'Connor, and L. Young, Thermal beam of metastable krypton atoms produced by optical excitation, Rev. Sci. Instrum. **78**, 023103 (2007).

[9] C. Y. Chen, K. Bailey, Y. M. Li, T. P. O'Connor, Z.-T. Lu, X. Du, L. Young, and G. Winkler, Beam of metastable krypton atoms extracted from a rf-driven discharge, Rev. Sci. Instrum. **72**, 271 (2001).

[10] E. Aprile, T. Yoon, A. Loose, L. W. Goetzke, and T. Zelevinsky, An atom trap trace analysis system for measuring krypton contamination in xenon dark matter detectors, Rev. Sci. Instrum. **84**, 093105 (2013).

[11] J. S. Wang, F. Ritterbusch, X.-Z. Dong, C. Gao, H. Li, W. Jiang, S.-Y. Liu, Z.-T. Lu, W.-H. Wang, G.-M. Yang, Y.-S. Zhang, and Z.-Y. Zhang, Optical Excitation and Trapping of ^{81}Kr, Phys. Rev. Lett. **127**, 023201 (2021).

[12] Z.-Y. Zhang, F. Ritterbusch, W.-K. Hu, X.-Z. Dong, C. Y. Gao, W. Jiang, S.-Y. Liu, Z.-T. Lu, J. S. Wang, and G.-M. Yang, Enhancement of the ^{81}Kr and ^{85}Kr count rates by optical pumping, Phys. Rev. A **101**, 053429 (2020).

[13] J. Han, L. Glebov, G. Venus, and M. C. Heaven, Demonstration of a diode-pumped metastable Ar laser, Opt. Lett. **38**, 5458 (2013).

[14] J. Han and M. C. Heaven, Kinetics of optically pumped Ar metastables, Opt. Lett. **39**, 6541 (2014).

[15] J. Han, M. C. Heaven, P. J. Moran, G. A. Pitz, E. M. Guild, C. R. Sanderson, and B. Hokr, Demonstration of a CW diode-pumped Ar metastable laser operating at 4 W, Opt. Lett. **42**, 4627 (2017).

[16] D. Emmons, "Analysis of Ar(1s 5) Metastable Populations in High Pressure Argon-Helium Gas Discharges", PhD Thesis (Air Force Institute of Technology, Wright-Patterson Air Force Base, 2017).

[17] W. T. Rawlins, K. L. Galbally-Kinney, S. J. Davis, A. R. Hoskinson, J. A. Hopwood, and M. C. Heaven, Optically pumped microplasma rare gas laser, Opt. Express **23**, 4804 (2015).

[18] J. Yang, Y. Yang, J. Luo, and B. Pan, Modeling of a diode transverse-pumped cesium vapor laser, Appl. Phys. B **115**, 571 (2014).

[19] Z. Yang, G. Yu, H. Wang, Q. Lu, and X. Xu, Modeling of diode pumped metastable rare gas lasers, Opt. Express **23**, 13823 (2015).

[20] J. Gao, Y. He, P. Sun, Z. Zhang, X. Wang, and D. Zuo, Simulations for transversely diode-pumped metastable rare gas lasers, J. Opt. Soc. Am. B **34**, 814 (2017).

[21] P. A. Mikheyev, Optically pumped rare-gas lasers, IEEE J. Quantum Electron. **45**, 704 (2015).

[22] S. Long, Y. Qin, H. Chen, X. Wu, M. Li, X. Tang, and T. Wen, Two-stage excitation model of diode pumped rare gas atoms lasers, Opt. Express **27**, 2771 (2019).

[23] A. V. Demyanov, I. V. Kochetov, and P. A. Mikheyev, Kinetic study of a cw optically pumped laser with metastable rare gas atoms produced in an electric discharge, J. Phys. D: Appl. Phys. **46**, 375202 (2013).

[24] J. D. Jackson, *Classical electrodynamics* (Wiley, New York, 1999).

[25] P. F. Bernath, *Spectra of Atoms and Molecules*, Third ed. (2016).

[26] C. Foot, *Atomic Physics* (Oxford University Press, 2005).

[27] G. B. Rybicki, *Radiative Processes In Astrophysics* (Wiley-VCH Verlag GmbH, 2004).

[28] J. B. Boffard, R. Jung, L. Anderson, and C. Lin, in *Advances In Atomic, Molecular, and Optical Physics*, Vol. 54, edited by P. Berman, C. Lin, and E. Arimondo (Academic Press, 2007), pages 319–421.

[29] R. C. Hilborn, Einstein coefficients, cross sections, f values, dipole moments, and all that, Am. J. Phys. **50**, 982 (1982).

[30] M. T. Meftah, H. Gossa, K. A. Touati, K. Chenini, and A. Naam, Doppler Broadening of Spectral Line Shapes in Relativistic Plasmas, Atoms **6**, 10.3390/atoms6020016 (2018).

[31] W Demtröder, *Laser Spectroscopy*, 4th ed. (Springer-Verlag, Berlin, 2008).

[32] G. Drake, *Springer Handbook of Atomic, Molecular, and Optical Physics* (Jan. 2006).

[33] S. S. Svanberg, *Atomic and Molecular Spectroscopy: Basic Aspects and Practical Applications*, 4th ed. (Springer, Berlin ; New York, 2004).

[34] T. Ye, D. Fu, and W. S. Warren, Nonlinear Absorption Microscopy, Photochem. Photobiol. **85**, 631 (2009).

[35] H Weber, Two-photon-absorption laws for coherent and incoherent radiation, IEEE J. Quantum Electron. **7**, 189 (1971).

[36] G. White, "Optical Excitation of Metastable Krypton and Photoassociative Spectroscopy of Ultracold RbAr", PhD Thesis (Old Dominion University, Norfolk, 2019).

[37] M. Kaschke, K.-H. Donnerhacke, and M. S. Rill, *Optical Devices in Ophthalmology and Optometry: Technology, Design Principles and Clinical Applications* (John Wiley & Sons, Incorporated, Weinheim, 2014).

[38] C. E. Wieman and L. Hollberg, Using diode lasers for atomic physics, Rev. Sci. Instrum. **62**, 1 (1991).

[39] S. M. Sze, *Physics of Semiconductor Devices*, Third ed. (Wiley-Interscience, Hoboken, N.J., 2007).

[40] P. K. Basu, *Semiconductor Laser Theory* (2015).

[41] C. Ye, *Tunable External Cavity Diode Lasers* (World Scientific, Hackensack, NJ, 2004).

[42] R. Höppner, E. Roldán, and G. J. de Valcárcel, A semiclassical optics derivation of Einstein's rate equations, Am. J. Phys. **80**, 882 (2012).

[43] J. R. Ackerhalt and B. W. Shore, Rate equations versus Bloch equations in multiphoton ionization, Phys. Rev. A **16**, 277 (1977).

[44] C.-F. Li, G.-C. Guo, and J. Piilo, Non-Markovian quantum dynamics: What does it mean?, Europhys. Lett. **127**, 50001 (2019).

[45] B. D. DePaola, *Notes for Lectures on Coherent Excitation*, 2015.

[46] N. Islam, T. Mondal, S. Chakraborty, and S. Biswas, Erratum: Re-examining Einstein's B coefficient and rate equations with the Rabi model (2019 J. Stat. Mech. 113104), J. Stat. Mech. **2020**, 029901 (2020).

[47] D. Manzano, A short introduction to the Lindblad master equation, AIP Adv. **10**, 025106 (2020).

[48] D. J. Griffiths and D. F. Schroeter, *Introduction to Quantum Mechanics*, Third ed. (Cambridge University Press, 2018).

[49] P. W. Milonni, *Laser Physics*, 2nd ed. (John Wiley & Sons, Hoboken, NJ, 2010).

[50] M. Suter and P. Dietiker, Calculation of the finesse of an ideal Fabry–Perot resonator, Appl. Opt. **53**, 7004 (2014).

[51] M. Pollnau and M. Eichhorn, Spectral coherence, Part I: Passive-resonator linewidth, fundamental laser linewidth, and Schawlow-Townes approximation, Prog. Quantum. Electron. **72**, 100255 (2020).

[52] N. Ismail, C. C. Kores, D. Geskus, and M. Pollnau, Fabry-Pérot resonator: spectral line shapes, generic and related Airy distributions, linewidths, finesses, and performance at low or frequency-dependent reflectivity, Opt. Express **24**, 16366 (2016).

[53] T. Amemiya and Y. Nakano, "Single Mode Operation of 1.5-μm Waveguide Optical Isolators Based on the Nonreciprocal-loss Phenomenon", in *Advances in Optical and Photonic Devices* (IntechOpen, 2010).

[54] H. C. Busch, M. B. Cooper, and C. I. Sukenik, Spectroscopy of neon for the advanced undergraduate laboratory, Am. J. Phys. **87**, 223 (2019).

[55] D. A. Shaddock, M. B. Gray, and D. E. McClelland, Frequency locking a laser to an optical cavity by use of spatial mode interference, Opt. Lett. **24**, 1499 (1999).

[56] N. Chabbra, A. R. Wade, E. R. Rees, A. J. Sutton, A. Stochino, R. L. Ward, D. A. Shaddock, and K. McKenzie, High stability laser locking to an optical cavity using tilt locking, Opt. Lett. **46**, 3199 (2021).

[57] N. P. Robins, B. J. J. Slagmolen, D. A. Shaddock, J. D. Close, and M. B. Gray, Interferometric, modulation-free laser stabilization, Opt. Lett. **27**, 1905 (2002).

[58] D. W. Preston, Doppler-free saturated absorption: Laser spectroscopy, Am. J. Phys. **64**, 1432 (1996).

[59] J. M. Supplee, E. A. Whittaker, and W. Lenth, Theoretical description of frequency modulation and wavelengthmodulation spectroscopy, Appl. Opt. **33**, 6294 (1994).

[60] G. C. Bjorklund, Frequency-modulation spectroscopy: a new method for measuring weak absorptions and dispersions, Opt. Lett. **5**, 15 (1980).

[61] M. Gehrtz, G. C. Bjorklund, and E. A. Whittaker, Quantum-limited laser frequency-modulation spectroscopy, J. Opt. Soc. Am. B **2**, 1510 (1985).

[62] E. A. Whittaker, P. Pokrowsky, W. Zapka, and G. C. Bjorklund, "Improved laser technique for high-sensitivity atomic absorption spectroscopy in flames", in Conference on Lasers and Electro-Optics (1983), WD5.

[63] E. D. Black, *Notes on the Pound-Drever-Hall Technique*, (Laser Interferometer Gravitational Wave Observatory, 1998).

[64] E. D. Black, An introduction to Pound–Drever–Hall laser frequency stabilization, Am. J. Phys. **69**, 79 (2000).

[65] R. W. P. Drever, J. L. Hall, F. V. Kowalski, J. Hough, G. M. Ford, A. J. Munley, and H. Ward, Laser phase and frequency stabilization using an optical resonator, Appl. Phys. B **31**, 97 (1983).

[66] D. J. McCarron, S. A. King, and S. L. Cornish, Modulation transfer spectroscopy in atomic rubidium, Meas. Sci. Technol. **19**, 105601 (2008).

[67] V. Negnevitsky, "Modulation transfer spectroscopy for fast , accurate laser stabilisation" (Monash University, Nov. 2009).

[68] H.-R. Noh, S. E. Park, L. Z. Li, J.-D. Park, and C.-H. Cho, Modulation transfer spectroscopy for 87Rb atoms: theory and experiment, Opt. Express **19**, 23444 (2011).

[69] T. Preuschoff, M. Schlosser, and G. Birkl, Optimization strategies for modulation transfer spectroscopy applied to laser stabilization, Opt. Express **26**, 24010 (2018).

[70] A. Ejlli, F. Della Valle, and G. Zavattini, Polarisation dynamics of a birefringent Fabry–Perot cavity, Appl. Phys. B **124**, 22 (2018).

[71] P. Berceau, M. Fouché, R. Battesti, F. Bielsa, J. Mauchain, and C. Rizzo, Dynamical behaviour of birefringent Fabry-Perot cavities, Appl. Phys. B **100**, 803 (2010).

[72] V. Kaufman, Wavelengths and Energy Levels of Neutral Kr(84) and Level Shifts in All Kr Even Isotopes, J. Res. Natl. Inst. **98**, 717 (1993).

[73] L. Young, D. Yang, and R. W. Dunford, Optical production of metastable krypton, J. Phys. B: At. Mol. Opt. Phys. **35**, 2985 (2002).

[74] J. Han and M. C. Heaven, Gain and lasing of optically pumped metastable rare gas atoms, Opt. Lett. **37**, 2157 (2012).

[75] J. Han and M. C. Heaven, Kinetics of optically pumped Kr metastables, Opt. Lett. **40**, 1310 (2015).

[76] C. Sansonetti and M. Greene, Infrared spectrum and revised energy levels for neutral krypton, Phys. Scr. **75**, 577 (2007).

[77] K. Dzierżęga, U. Volz, G. Nave, and U. Griesmann, Accurate transition rates for the 5p-5s transitions in Kr I, Phys. Rev. A **62**, 022505 (2000).

[78] D. Zhong, D. W. Setser, R. Sobczynski, and W. Gadomski, Conservation of the Kr+(2P1/2) state in the reactive quenching of Kr(5s'[1/2]0) atoms by halogen-containing molecules, J. Chem. Phys. **105**, 5020 (1996).

[79] A. V. Demyanov, I. V. Kochetov, P. A. Mikheyev, V. N. Azyazov, and M. C. Heaven, Kinetic analysis of rare gas metastable production and optically pumped Xe lasers, J. Phys. D: Appl. Phys. **51**, 045201 (2018).

[80] C. A. Whitehead, H. Pournasr, M. R. Bruce, H. Cai, J. Kohel, W. B. Layne, and J. W. Keto, Deactivation of two-photon excited Xe(5p56p,6p',7p) and Kr(4p55p) in xenon and krypton, J. Chem. Phys. **102**, 1965 (1995).

[81] G. Zikratov and D. W. Setser, State-to-state rate constants for the collisional interaction of Xe(7p), Xe(6p'), and Kr(5p') atoms with He and Ar, J. Chem. Phys. **104**, 2243 (1996).

APPENDIX A

RADIATIVE AND NON-RADIATIVE RATES

A.1 SPONTANEOUS EMISSION RATES

TABLE 2. Table of spontaneous emission rate coefficients for transitions included in model.

Transition	Einstein A_{21} (10^6 s^{-1})	Reference
$1s_2 \rightarrow {}^1S_0$	224.20	[12]
$1s_4 \rightarrow {}^1S_0$	225.20	[12]
$2p_5 \rightarrow 1s_2$	0.04	[77]
$2p_6 \rightarrow 1s_2$	0.31	[77]
$2p_7 \rightarrow 1s_2$	0.106	[77]
$2p_8 \rightarrow 1s_2$	0.081	[77]
$2p_{10} \rightarrow 1s_2$	0.074	[77]
$2p_7 \rightarrow 1s_3$	0.076	[77]
$2p_{10} \rightarrow 1s_3$	0.126	[77]
$2p_5 \rightarrow 1s_4$	43.10	[77]
$2p_6 \rightarrow 1s_4$	8.94	[77]
$2p_7 \rightarrow 1s_4$	29.31	[77]
$2p_8 \rightarrow 1s_4$	22.17	[77]
$2p_{10} \rightarrow 1s_4$	3.13	[77]
$2p_6 \rightarrow 1s_5$	27.32	[77]
$2p_7 \rightarrow 1s_5$	4.27	[77]
$2p_8 \rightarrow 1s_5$	8.96	[77]
$2p_9 \rightarrow 1s_5$	36.10	[77]
$2p_{10} \rightarrow 1s_5$	22.89	[77]

A.2 COLLISIONAL DEACTIVATION RATES

TABLE 3. Kr-He collisional deactivation rate coefficients for transitions included in model.

Transition	Kr-Kr Deactivation Rate (10^6 $s^{-1}cm^3$)	Reference
$1s_4 \rightarrow {}^1S_0$	$1{\cdot}10^{-10}$	[78]
$1s_5 \rightarrow {}^1S_0$	$1{\cdot}10^{-10}$	[78]
$1s_5 \rightarrow 1s_4$	$2.44{\cdot}10^{-15}$	[75]
$2p_{10} \rightarrow 1s_5$	$7.2{\cdot}10^{-11}$	[79]
$2p_5 \rightarrow 2p_6$	$26.0{\cdot}10^{-12}$	[80]
$2p_5 \rightarrow 2p_7$	$1.3{\cdot}10^{-11}$	[80]
$2p_5 \rightarrow 2p_8$	$5{\cdot}10^{-11}$	[80]
$2p_5 \rightarrow 2p_9$	$7{\cdot}10^{-12}$	[80]
$2p_5 \rightarrow 2p_{10}$	$0.5{\cdot}10^{-12}$	[80]
$2p_6 \rightarrow 2p_7$	$0.73{\cdot}10^{-12}$	[80]
$2p_6 \rightarrow 2p_8$	$5.0{\cdot}10^{-12}$	[80]
$2p_6 \rightarrow 2p_9$	$22{\cdot}10^{-12}$	[80]
$2p_6 \rightarrow 2p_{10}$	$0.2{\cdot}10^{-12}$	[80]
$2p_8 \rightarrow 2p_7$	$1.80{\cdot}10^{-11}$	[80]
$2p_8 \rightarrow 2p_9$	$2.62{\cdot}10^{-10}$	[80]
$2p_8 \rightarrow 2p_{10}$	$8.1{\cdot}10^{-11}$	[80]
$2p_9 \rightarrow 2p_8$	$1.77{\cdot}10^{-10}$	[79]
$2p_9 \rightarrow 2p_{10}$	$2.7{\cdot}10^{-11}$	[79]

TABLE 4. Kr-He collisional deactivation rate coefficients for transitions included in model.

Transition	Kr-He Deactivation Rate (10^6 $s^{-1}cm^3$)	Reference
$1s_4 \rightarrow {}^1S_0$	$2{\cdot}10^{-13}$	[75]
$1s_5 \rightarrow 1s_4$	$8{\cdot}10^{-14}$	[75]
$2p_9 \rightarrow 1s_5$	$0{\cdot}10^{-11}$	[79]
$2p_{10} \rightarrow 1s_5$	$6{\cdot}10^{-12}$	[79]
$2p_2 \rightarrow 2p_3$	$44{\cdot}10^{-11}$	[81]
$2p_3 \rightarrow 2p_2$	$60{\cdot}10^{-11}$	[81]
$2p_2 \rightarrow 2p_4$	$5.5{\cdot}10^{-12}$	[81]
$2p_4 \rightarrow 2p_2$	$1.7{\cdot}10^{-11}$	[81]
$2p_3 \rightarrow 2p_4$	$8{\cdot}10^{-11}$	[81]
$2p_4 \rightarrow 2p_3$	$1.7{\cdot}10^{-11}$	[81]
$2p_8 \rightarrow 2p_9$	$3.3{\cdot}10^{-10}$	[79]
$2p_9 \rightarrow 2p_8$	$1.3{\cdot}10^{-10}$	[75]
$2p_8 \rightarrow 2p_{10}$	$2.3{\cdot}10^{-11}$	[79]
$2p_{10} \rightarrow 2p_8$	$2.5{\cdot}10^{-13}$	[75]
$2p_9 \rightarrow 2p_{10}$	$7.0{\cdot}10^{-12}$	[79]
$2p_{10} \rightarrow 2p_9$	$2.5{\cdot}10^{-13}$	[75]
$2p_2 \rightarrow 3d_9$	$33{\cdot}10^{-11}$	[81]
$2p_3 \rightarrow 3d_{10}$	$40{\cdot}10^{-11}$	[81]
$2p_4 \rightarrow 3d_{10}$	$20{\cdot}10^{-11}$	[81]
$2p_6 \rightarrow 3d_{10}$	$15{\cdot}10^{-11}$	[81]
$2p_8 \rightarrow 3d_{10}$	$15{\cdot}10^{-11}$	[81]
$2p_9 \rightarrow 3d_9$	$4{\cdot}10^{-11}$	[81]

APPENDIX B

FINISHED MIRROR MOUNTS

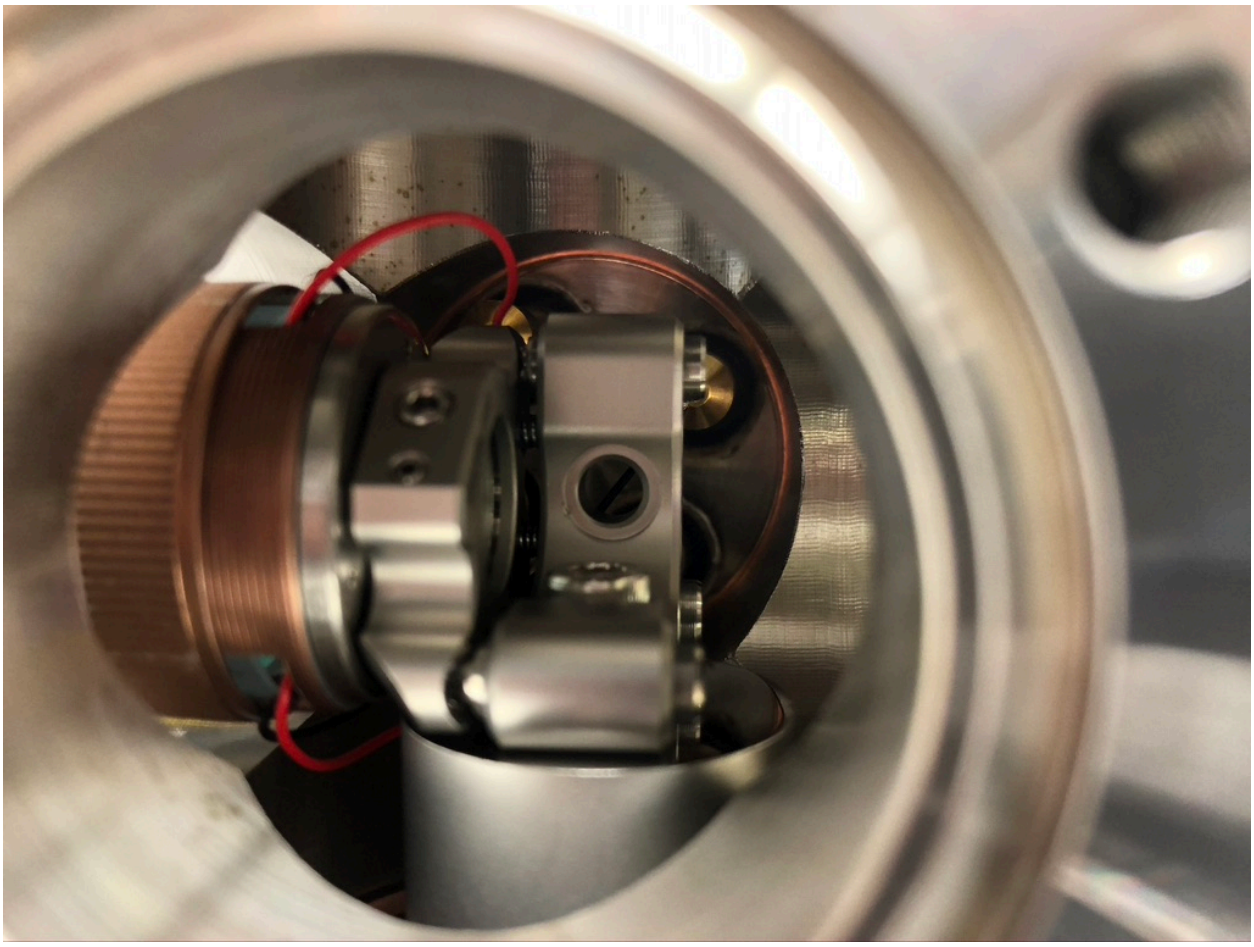

FIG. 48. This figure shows the finished product of the first mirror mount design actually used in the cavity.

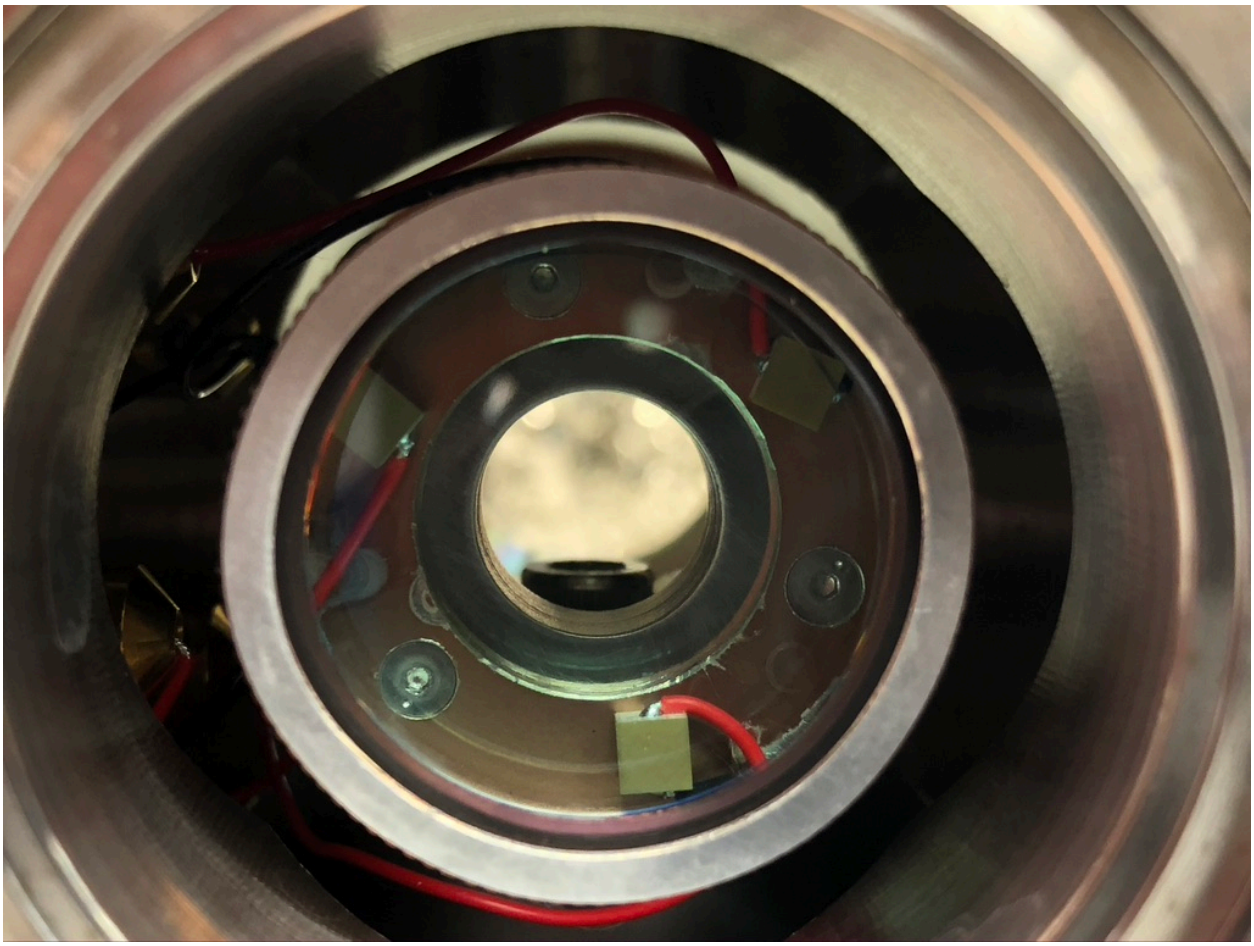

FIG. 49. This figure shows the front of the first mirror mount design actually used in the cavity. The scanning piezos can be seen that push against the mirror.

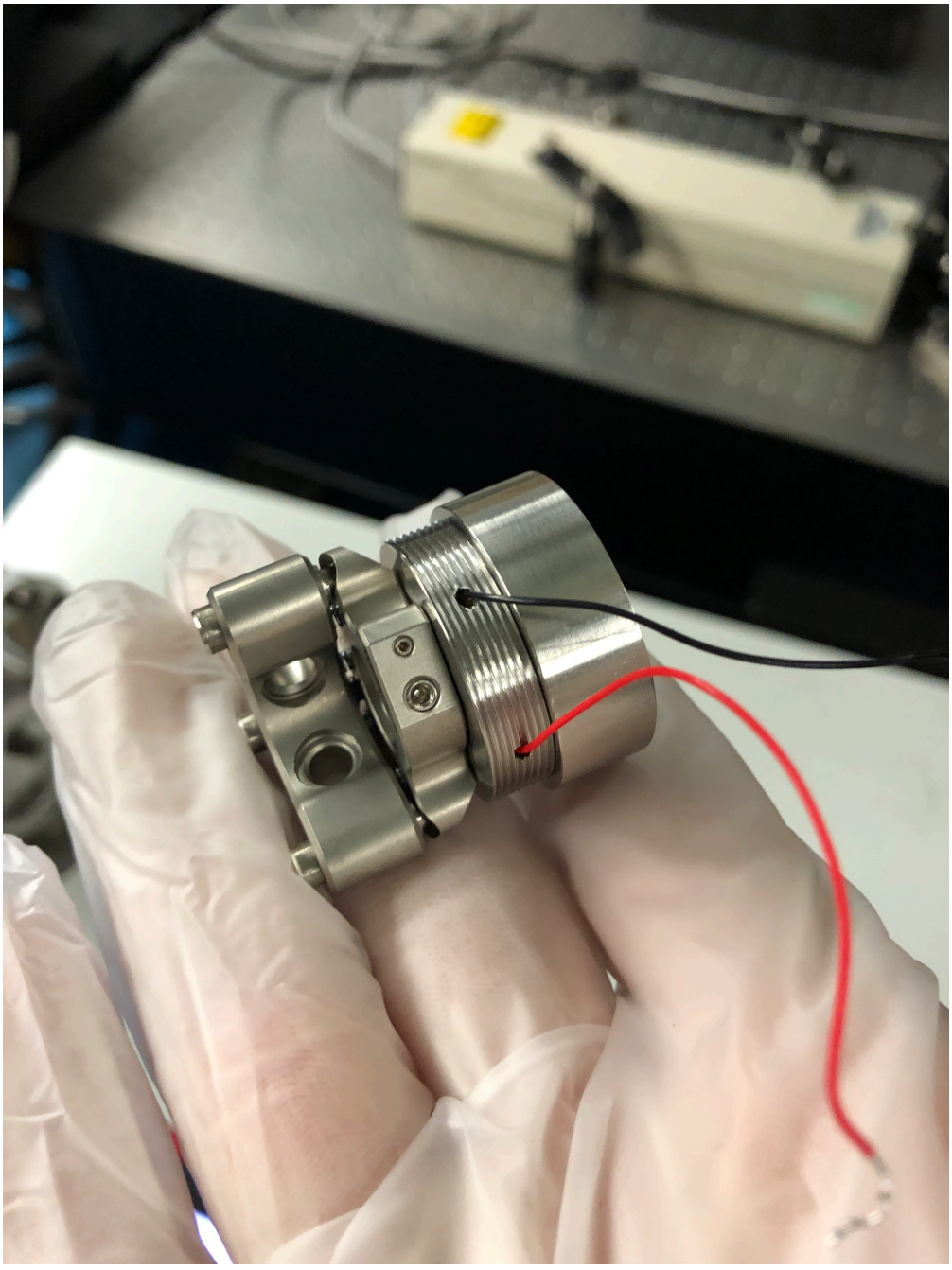

FIG. 50. This figure shows the finished product of the final mirror mount design actually used in the cavity.

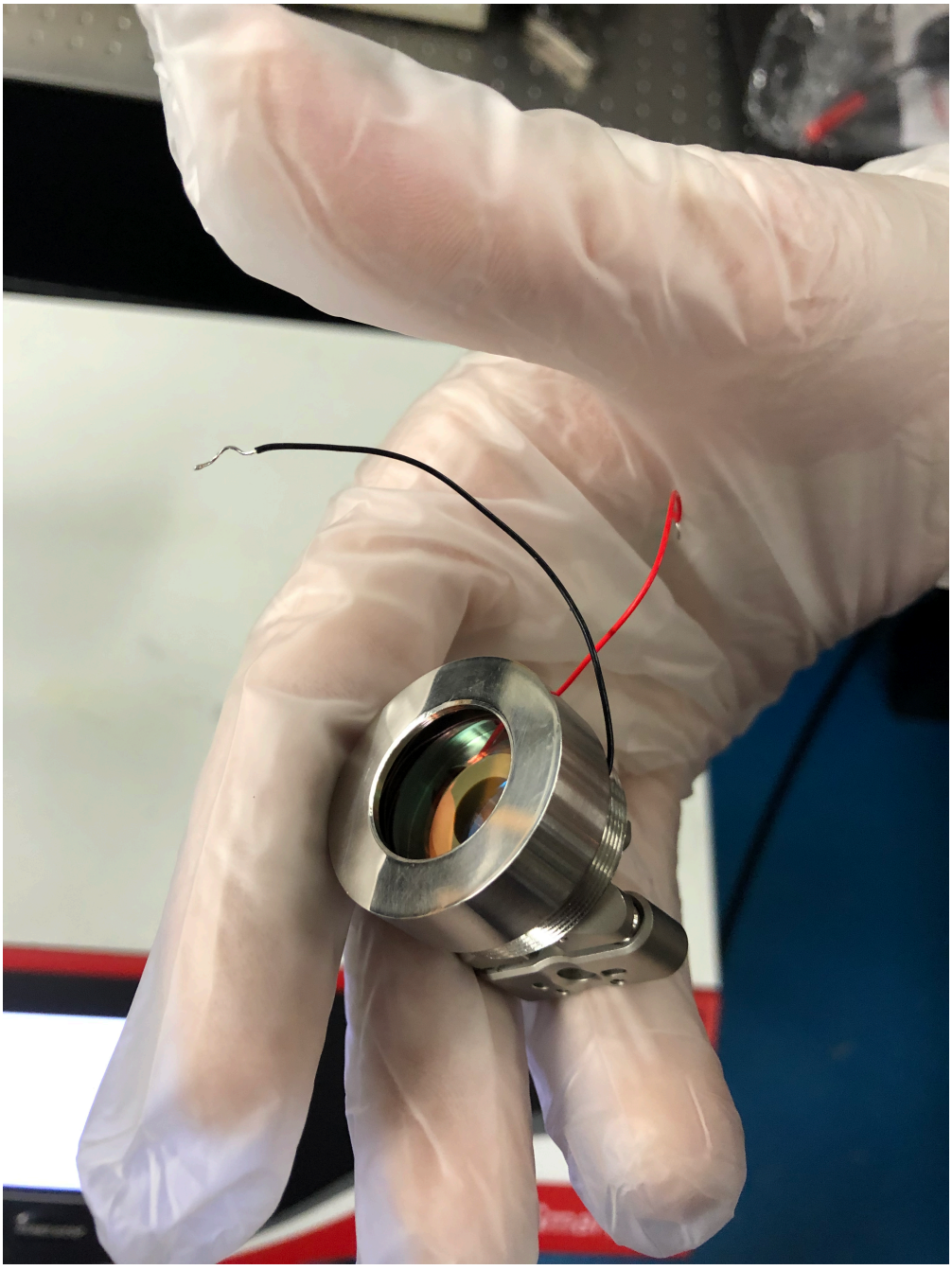

FIG. 51. This figure shows the front of the final mirror mount design actually used in the cavity. The scanning ring piezo can be seen that pushed against the mirror.

APPENDIX C

INSTRUMENTAL MEASUREMENTS

C.1 INTERFERENCE FILTER MEASUREMENTS

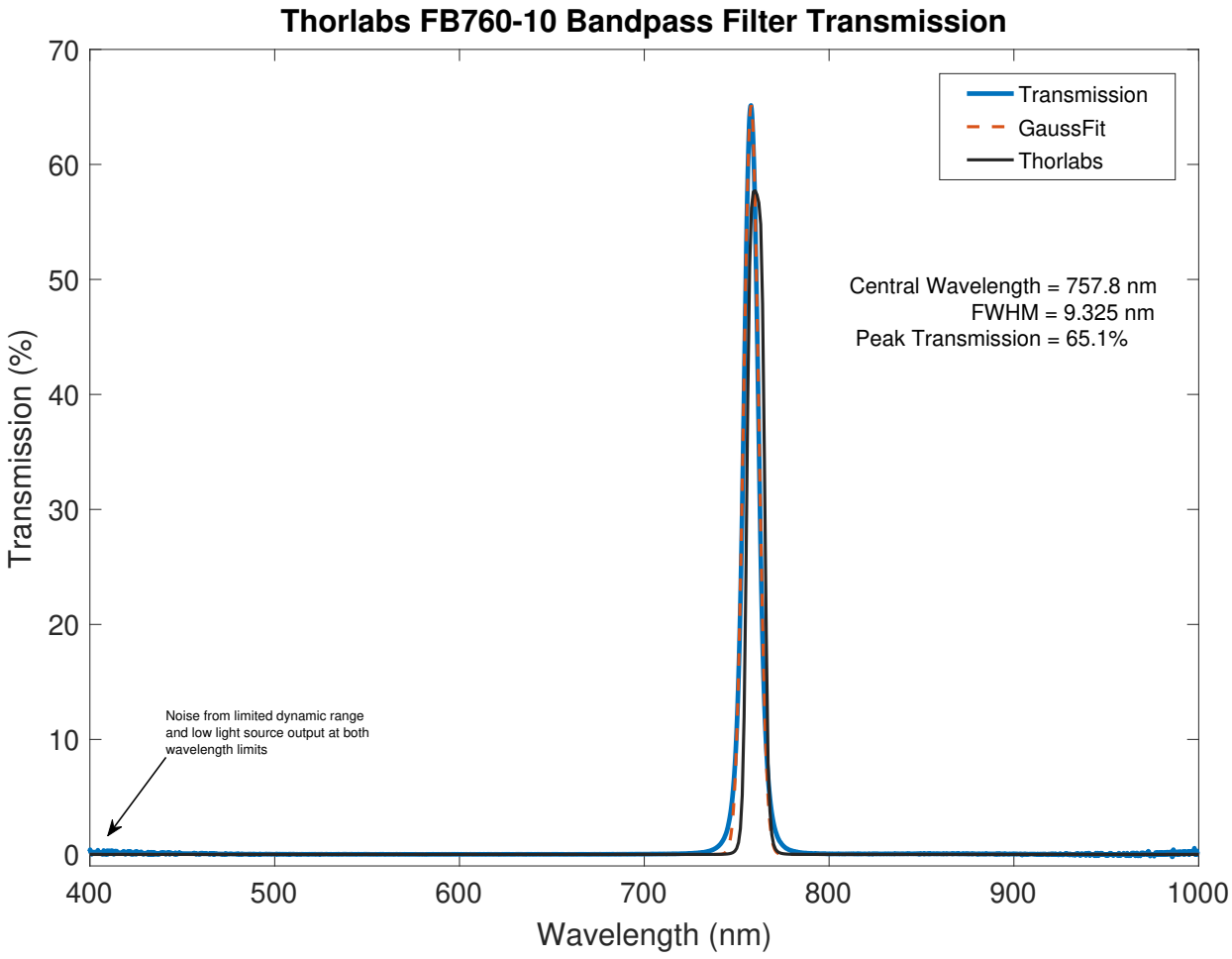

FIG. 52. Transmission measurement of Thorlabs FB760-10 plotted against manufacturer's specs and Gaussian fit.

C.2 TOPTICA THRESHOLD CURRENT MEASUREMENTS

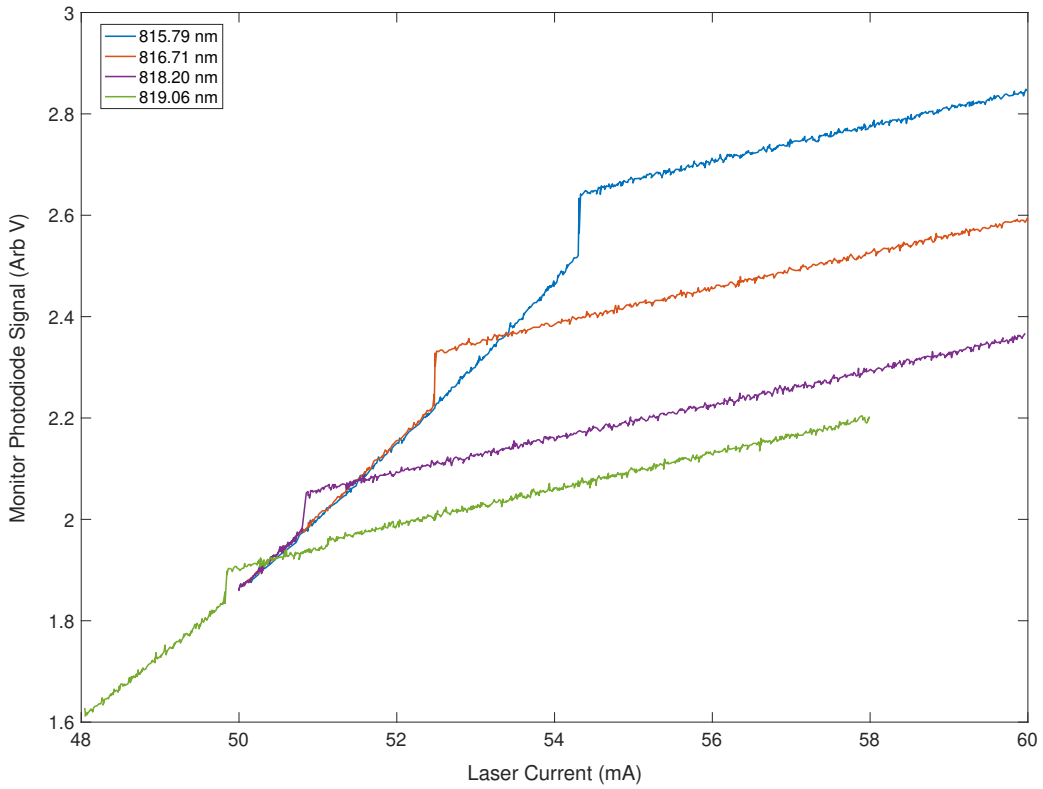

FIG. 53. Wavelength dependence of threshold current while working to tune the laser to run single mode at 819 nm. The laser was factory aligned at 811 nm and the collimation was too far out of alignment to run single mode at 819 nm. The slightly nonlinear dependence on current can be seen below threshold, while the response is linear above threshold. The 819 nm curve has a jump in the linear regime near 51 mA because it was before adjusting the collimation, and therefore the laser was running multimode. The threshold current at 819 nm dropped from 50 mA to 47 mA after collimation.

C.3 LOCK-BOX SERVO BODE PLOTS

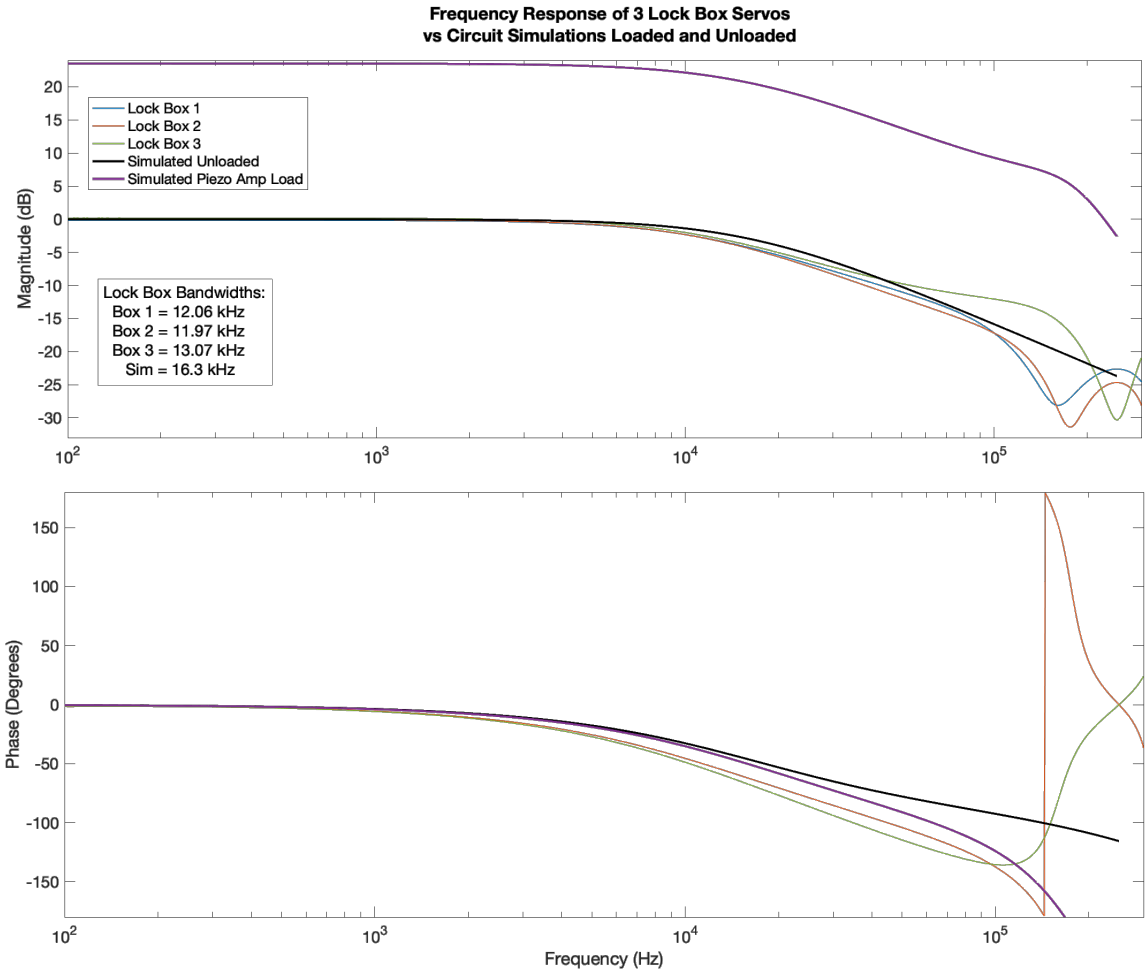

FIG. 54. Bode plots of the three lock boxes under test compared to the simulated circuit. Differences occur due to different component selections over the years as the different boxes were built.

APPENDIX D

FEEDBACK SERVO CIRCUIT SCHEMATIC

Figure 55 shows the low-frequency feedback servo used in this work. The figure shows the schematic in National Instruments Multisim^{TM}, which was used for simulating the circuit. This circuit originates from the Thad Walker's group at University of Wisconsin. The function of this circuit is to allow the user to switch from open-loop scanning of the piezo, for visualization of the locking signal, to closed-loop operation of the piezo for active stabilization. The Bode plots of three servos that were analyzed can be found in Appendix C.3.

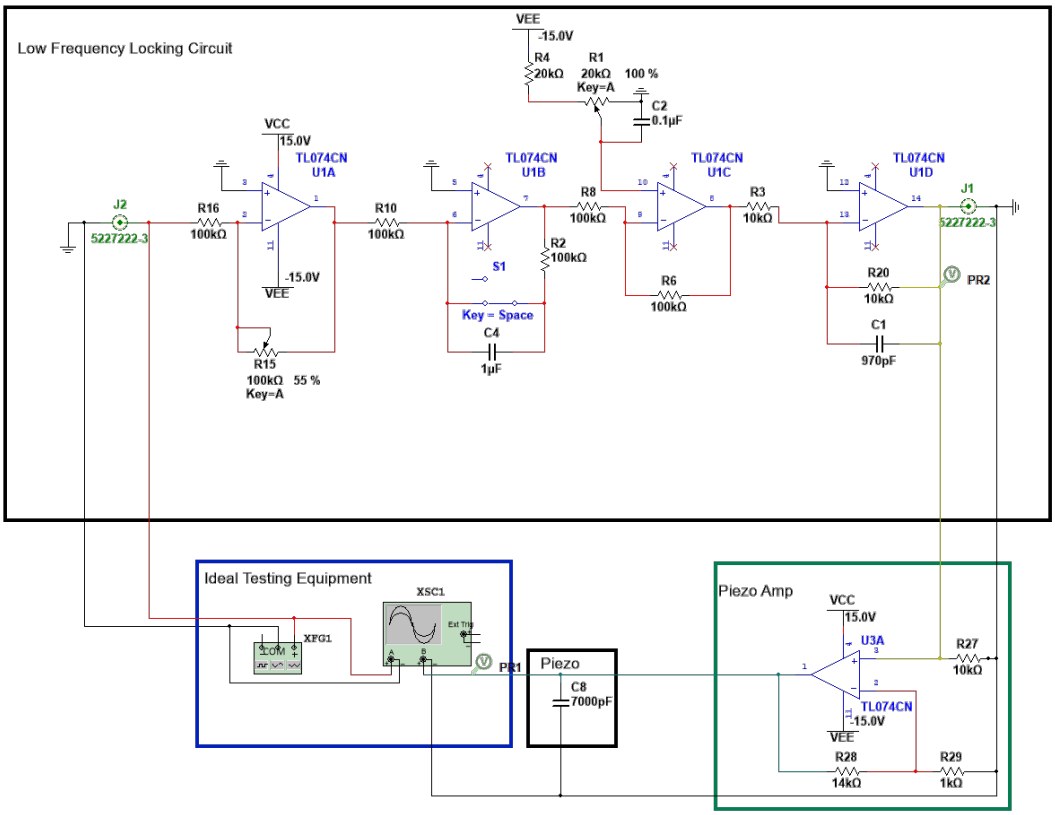

FIG. 55. Multisim schematic of the lock box servo for scanning and locking a laser or cavity.

APPENDIX E

LICENSE AGREEMENTS

E.1 DEMTRODER

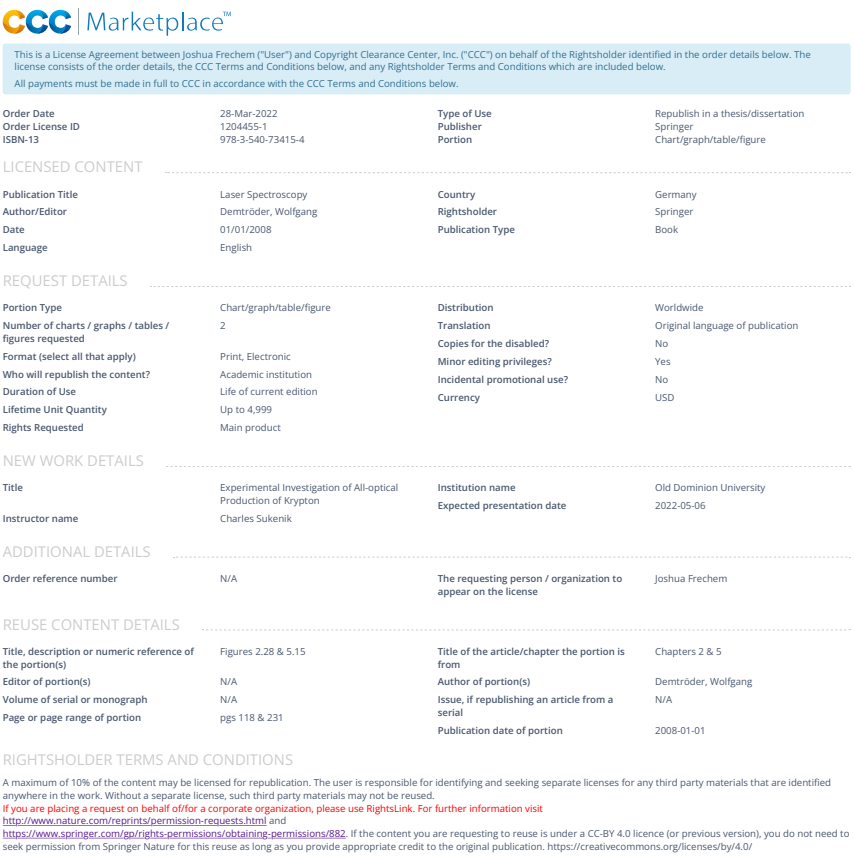

CCC Marketplace™

This is a License Agreement between Joshua Frechem ("User") and Copyright Clearance Center, Inc. ("CCC") on behalf of the Rightsholder identified in the order details below. The license consists of the order details, the CCC Terms and Conditions below, and any Rightsholder Terms and Conditions which are included below.

All payments must be made in full to CCC in accordance with the CCC Terms and Conditions below.

Order Date	28-Mar-2022	**Type of Use**	Republish in a thesis/dissertation
Order License ID	1204455-1	**Publisher**	Springer
ISBN-13	978-3-540-73415-4	**Portion**	Chart/graph/table/figure

LICENSED CONTENT

Publication Title	Laser Spectroscopy	**Country**	Germany
Author/Editor	Demtröder, Wolfgang	**Rightsholder**	Springer
Date	01/01/2008	**Publication Type**	Book
Language	English		

REQUEST DETAILS

Portion Type	Chart/graph/table/figure	**Distribution**	Worldwide
Number of charts / graphs / tables / figures requested	2	**Translation**	Original language of publication
		Copies for the disabled?	No
Format (select all that apply)	Print, Electronic	**Minor editing privileges?**	Yes
Who will republish the content?	Academic institution	**Incidental promotional use?**	No
Duration of Use	Life of current edition	**Currency**	USD
Lifetime Unit Quantity	Up to 4,999		
Rights Requested	Main product		

NEW WORK DETAILS

Title	Experimental Investigation of All-optical Production of Krypton	**Institution name**	Old Dominion University
		Expected presentation date	2022-05-06
Instructor name	Charles Sukenik		

ADDITIONAL DETAILS

Order reference number	N/A	**The requesting person / organization to appear on the license**	Joshua Frechem

REUSE CONTENT DETAILS

Title, description or numeric reference of the portion(s)	Figures 2.28 & 5.15	**Title of the article/chapter the portion is from**	Chapters 2 & 5
Editor of portion(s)	N/A	**Author of portion(s)**	Demtröder, Wolfgang
Volume of serial or monograph	N/A	**Issue, if republishing an article from a serial**	N/A
Page or page range of portion	pgs 118 & 231	**Publication date of portion**	2008-01-01

RIGHTSHOLDER TERMS AND CONDITIONS

A maximum of 10% of the content may be licensed for republication. The user is responsible for identifying and seeking separate licenses for any third party materials that are identified anywhere in the work. Without a separate license, such third party materials may not be reused.

If you are placing a request on behalf of/for a corporate organization, please use RightsLink. For further information visit http://www.nature.com/reprints/permission-requests.html and https://www.springer.com/gp/rights-permissions/obtaining-permissions/882. If the content you are requesting to reuse is under a CC-BY 4.0 licence (or previous version), you do not need to seek permission from Springer Nature for this reuse as long as you provide appropriate credit to the original publication. https://creativecommons.org/licenses/by/4.0/

FIG. 56. License agreement to use figures from [31].

E.2 KASCHKE

CCC Marketplace™

This is a License Agreement between Joshua Frechem ("User") and Copyright Clearance Center, Inc. ("CCC") on behalf of the Rightsholder identified in the order details below. The license consists of the order details, the CCC Terms and Conditions below, and any Rightsholder Terms and Conditions which are included below.

All payments must be made in full to CCC in accordance with the CCC Terms and Conditions below.

Order Date	28-Mar-2022	Type of Use	Republish in a thesis/dissertation
Order License ID	1204460-1	Publisher	Wiley
ISBN-13	9783527410682	Portion	Chart/graph/table/figure

LICENSED CONTENT

Publication Title	Optical Devices in Ophthalmology and Optometry : Technology, Design Principles and Clinical Applications	Country	Germany
		Rightsholder	John Wiley & Sons - Books
Author/Editor	Kaschke, Michael, Donnerhacke, Karl-Heinz, Rill, Michael Stefan	Publication Type	Book
Date	10/21/2013		
Language	English		

REQUEST DETAILS

Portion Type	Chart/graph/table/figure	Distribution	Worldwide
Number of charts / graphs / tables / figures requested	3	Translation	Original language of publication
		Copies for the disabled?	No
Format (select all that apply)	Print, Electronic	Minor editing privileges?	Yes
Who will republish the content?	Academic institution	Incidental promotional use?	No
Duration of Use	Life of current edition	Currency	USD
Lifetime Unit Quantity	Up to 4,999		
Rights Requested	Main product		

NEW WORK DETAILS

Title	Experimental Investigation of All-Optical Production of Metastable Krypton	Institution name	Old Dominion University
		Expected presentation date	2022-05-06
Instructor name	Charles Sukenik		

ADDITIONAL DETAILS

The requesting person / organization to appear on the license	Joshua Frechem

REUSE CONTENT DETAILS

Title, description or numeric reference of the portion(s)	Figures B.3, B.15, and B.20	Title of the article/chapter the portion is from	B.2.2 Multilevel Optical Pumping, B.5.1 Gas Lasers, and B.5.2 Semiconductor Lasers
Editor of portion(s)	N/A	Author of portion(s)	Kaschke, Michael; Donnerhacke, Karl-Heinz; Rill, Michael Stefan
Volume of serial or monograph	N/A		
Page or page range of portion	pgs 556, 573, and 577	Publication date of portion	2013-10-21

RIGHTSHOLDER TERMS AND CONDITIONS

No right, license or interest to any trademark, trade name, service mark or other branding ("Marks") of WILEY or its licensors is granted hereunder, and you agree that you shall not assert any such right, license or interest with respect thereto. You may not alter, remove or suppress in any manner any copyright, trademark or other notices displayed by the Wiley material. This Agreement will be void if the Type of Use, Format, Circulation, or Requestor Type was misrepresented during the licensing process. In no instance may the total amount of Wiley Materials used in any Main Product, Compilation or Collective work comprise more than 5% (if figures/tables) or 15% (if full articles/chapters) of the (entirety of the) Main Product, Compilation or Collective Work. Some titles may be available under an Open Access license. It is the Licensors' responsibility to identify the type of Open Access license on which the requested material was published, and comply fully with the terms of that license for the type of use specified Further details can be found on Wiley Online Library http://olabout.wiley.com/WileyCDA/Section/id-410895.html.

FIG. 57. License agreement to use figures from [37].

FIG. 58. Licensing terms for Copyright Clearance Center.

VITA

Joshua Carl Frechem
Department of Physics
Old Dominion University
Norfolk, VA 23529

Education: Ph.D. Physics Expected May 2022 Old Dominion University
Dissertation Title: Experimental Investigation of All-optical Production of Metastable Krypton
Advisor: Dr. Charles I. Sukenik

M.S. Physics May 2019, Old Dominion University
B.S. Physics August 2016, Old Dominion University
B.S.M.E. August 2016, Old Dominion University

Publications & Presentations:
Frechem, Joshua, "Investigation of All-optical Production of Metastable Krypton," APS Division of Atomic, Molecular, and Optical Physics Meeting 2021.
L. L. Taylor, J. C. Frechem, H. Han, J. Xu, T. R. Smith, M. Pomerantz, J. C. Lambropoulos, and J. Qiao, "Material Removal and Thermal Impact of Femtosecond-Laser Polishing for Germanium-Based Freeform Optics," in Optical Design and Fabrication 2017

Typeset using LaTeX.